



# **Ultrasound Transducers for a Simplified Martian Acoustic Anemometer**

Submitted By  
Xinyu Shi

IN PARTIAL FULFILLMENT OF THE REQUIREMENTS FOR THE DEGREE OF  
MASTER OF SCIENCE IN MECHANICAL ENGINEERING

School of Engineering  
Tufts University  
Medford, Massachusetts

May 2018  
© 2018 Xinyu Shi

Advisor:  
Robert White  
Associate Professor  
Department of Mechanical Engineering  
Tufts University



## **Abstract**

The selection, modeling and verification of ultrasonic transducers in an ultrasound transmit - receive system are described. The system is applied to the measurement of wind speed in an acoustic anemometry application. The target environment for the final system is the surface of Mars, which requires operation in approximately 6 mbar CO<sub>2</sub>. Four transducers are tested as part of this work: Kobitone and PUI piezoelectric transducers, and custom “CAP1” and capacitive micromachined ultrasound (cMUT) transducers from VN Instruments and Tufts University, respectively. Tukey - windowed linear chirp acoustic signal is chosen and analyzed using cross frequency techniques. A model for the full system frequency response, which includes the control electronics, electromechanical coupling of the transducers and attenuation of sound, is provided and verified. Transducers are also characterized using LDV (Laser Doppler Vibrometry) and input impedance measurement. For PUI transducers, the model provides a peak value within 5% of the measured value in air and in 6 mbar CO<sub>2</sub>. Time delay are also predicted to have a value within 10% difference from the calculated distance in atmospheric air for all the transducer tested.

## **Acknowledgements**

I am grateful to my advisor, Professor Robert D. White for giving me the opportunity to work on this project, as well as the guidance and help during the project. His passion, knowledge and the quality of his research work has been my goal until this day.

I'm also thankful for Dr. Don Banfield for initiating this promising project and being in the thesis committee, as well as Ian Neeson for the help he gave me in understanding the TivaUT system. I would like to thank my thesis committee members Professor Jason Rife and Professor Brian Tracey for being willing to take time to be part of this project and providing invaluable suggestions.

I would also like to thank my family for their emotional support and encouragement over the years. They have inspired me to be who am I today.





## Table of Contents

Chapter 1	Introduction.....	1
1.1	Motivation .....	1
1.2	Contributions .....	2
Chapter 2	Background .....	4
2.1	Ultrasound and sound propagation .....	4
2.2	Ultrasound transducers .....	7
2.2.1	Piezoelectric transducers .....	8
2.2.2	Capacitive micromachined ultrasonic transducer (cMUT) .....	11
2.3	Anemometers.....	12
2.4	Mars .....	17
2.4.1	Martian surface wind and dust devils.....	17
2.4.2	Mars Exploration and Wind Speed Measurement .....	19
2.4.3	Need for a better method.....	24
2.4.4	Challenges for ultrasonic anemometer operating on Mars .....	24
Chapter 3	Testing Methods.....	27
3.1	Selecting transducers.....	27
3.2	Parameters .....	29
3.2.1	Laser Doppler Vibrometry (LDV).....	29
3.2.2	Input Impedance measurement .....	33
3.2.3	Combining LDV and Input impedance measurement results.....	35
3.2.4	Speed of Sound.....	36
3.3	Experiment setup .....	39
3.3.1	Chamber and pressure.....	39
3.3.2	Setup and alignment.....	40
3.4	Measurement .....	41
3.4.1	Tiva UT and Configuration .....	41
3.4.2	Time domain measurement .....	42
3.5	Analytic method.....	46
3.5.1	Power Spectral Density (PSD) and Cross Power Spectral Density (CPSD) .....	46
3.5.2	Cross correlation and time delay calculation.....	46
Chapter 4	Modeling of the transmit- receive system .....	48
4.1	Key assumptions .....	49
4.2	Modeling .....	50
4.2.1	Drive amplifier .....	50
4.2.2	Transmitter transfer function.....	55
4.2.3	Absorption.....	61
4.2.4	Receiver transfer function .....	64
4.2.5	Receive amplifier.....	65
4.2.6	System transfer function .....	67
Chapter 5	Results .....	68
5.1	Time domain plot.....	68
5.2	Peak amplitude of time domain chirp .....	75
5.3	Time of flight.....	76
Chapter 6	Discussion .....	78
Chapter 7	Conclusions and Future Work.....	81

7.1	Conclusions .....	81
7.2	Future Work.....	82
Appendix A .....		85
Appendix B .....		89
Appendix C .....		91
Appendix D .....		94
Appendix E .....		100
Bibliography.....		101

## Table of Figures

Figure 1 Acoustic range versus frequency.....	4
Figure 2 SONAR image of Little Hercules, a wooden-hulled ship wreck in the 19 <sup>th</sup> century [6].....	5
Figure 3 Cartesian coordinates for piezoelectric material [10].....	9
Figure 4 Schematic of a piezoelectric ultrasonic transducer (a) conventional extensional transducers (b) pMUTs [11].....	10
Figure 5 Schematic of a single element in a cMUT array [14].....	12
Figure 6 Simplified schematic of a dual beam Laser Doppler Anemometer [20] .....	14
Figure 7: Common setup for an ultrasonic anemometer [2].....	15
Figure 8 1D demonstration of transmission for an ultrasonic anemometer.....	16
Figure 9 A dust devil on Northern Mars captured by NASA's Reconnaissance Orbiter [27] .....	18
Figure 10 Model of a Viking lander [29].....	19
Figure 11 The hot-wire anemometer model on the Viking lander [26] .....	21
Figure 12 Pathfinder Rover Schematic [34] .....	22
Figure 13 Telltale wind indicator on Phoenix [35] .....	23
Figure 14 Ultrasonic transducers that were tested .....	28
Figure 15 LDV measurement for PUI-B transducer at a single point across frequency ...	30
Figure 16 Surface LDV scan of PUI-B transducer at 41200 Hz.....	31
Figure 17 Calculated beam pattern for Kobitone transducer using LDV .....	32
Figure 18 Example of input impedance modeling of PUI transducers in 6 mbar CO <sub>2</sub> .....	35
Figure 19 Gas constant variation with humidity [37].....	38
Figure 20 Testing setup for transducers in air.....	39
Figure 21 Testing setup for Kobitone transducers in vacuum chamber .....	40
Figure 22 An example of a time domain plot .....	43
Figure 23 40% percent Tukey window used in the experiment.....	45
Figure 24 Block diagram of transfer functions in the transmit receive system .....	48
Figure 25 Time domain chirp signal for Digital Number Sent (input).....	50
Figure 26 Received chirp signal on oscilloscope (output).....	51
Figure 27 Coherence plot between the signal sent and received .....	51
Figure 28 Gain plot model vs. experiment .....	53
Figure 29 Gain plot for two load cases at three different percentages .....	54
Figure 30 Single point LDV for Kobitone transducer.....	57
Figure 31 Mechanical model of a piezoelectric transducer [39].....	58
Figure 32 Equivalent electrical circuit.....	58
Figure 33 Equivalent circuit model of an ultrasonic transducer .....	60
Figure 34 Absorption coefficient in Np/m as a function of frequency in Martian atmosphere .....	63
Figure 35 Absorption of sound as a function of frequency in 1 atm air [7] .....	64
Figure 36 Preamplifier circuit diagram .....	66
Figure 37 Time domain plot for PUI in atmospheric air .....	68
Figure 38 Time domain plot for PUI in CO <sub>2</sub> at 1.8 cm .....	69
Figure 39 Time domain plot for PUI in CO <sub>2</sub> at 3.1 cm .....	71
Figure 40 Time domain plot for Kobitone in atmospheric air .....	72

Figure 41 Time domain plot for Kobitone in 6 mbar CO <sub>2</sub> .....	72
Figure 42 Time domain plot for Tufts cMUT in atmospheric air .....	73
Figure 43 Time domain plot for Tufts cMUT in 6mbar CO <sub>2</sub> .....	74
Figure 44 Time domain plot for CAP1 in atmospheric air .....	75

## Table of Tables

Table 1 Comparison between various anemometers .....	13
Table 2 Comparison of Module Mean Data with the 20-Sol Mean Results at the same LLT (Local Lander Time) for wind speed, direction and temperature on the Viking Lander [30].....	20
Table 3 Basic properties from datasheet of the transducers tested .....	29
Table 4 Transducer parameters based on LDV model in air .....	31
Table 5 Transducer parameters from input impedance model.....	34
Table 6 Transducer parameters combining LDV and input impedance model .....	36
Table 7 Time settings for time domain testing for transducers.....	44
Table 8 Parameters used in the calculation for absorption coefficient [8,46] .....	62
Table 9 Comparison of signal sent and received in various gain settings.....	76
Table 10 Time of flight result for transducers tested .....	77
Table 11 Percentage difference between measurement and prediction.....	79

# Chapter 1      Introduction

The goal of this dissertation is to describe and apply a selection process for ultrasonic transducers applied to a Martian acoustic anemometer. In addition, we demonstrate a modeling and verification process for the ultrasound frequency response in such a transmit and receive application. The system model includes the control electronics, ultrasonic transducers, and transmission effects in air or CO<sub>2</sub>. The anemometer will be applied in the future for measuring wind speed on Mars, with far reaching impacts on our understanding of Martian atmospheric dynamics.

To build a successful anemometer, four pairs of ultrasonic transducers were selected and tested and a transmit - receive model was built for testing the transducers in atmospheric air and 6 mbar CO<sub>2</sub>. Although there have been efforts in designing and building an ultrasonic anemometer on Mars, a successful measurement of Mars wind speed using such method has yet to happen. The paper focuses on modeling the acoustic transmission process for the transmit – receive system of a pair of ultrasonic transducers and therefore, predicting the time of flight and intensity for the received signal. The model will be used as a design tool that allows transducers and signal processing optimization.

## **1.1 Motivation**

Various anemometers have been developed and equipped for Martian landers and rovers in the past decades. These anemometers include a hot-wire anemometer with wind sock, a hot-film anemometer and a telltale. They have all provided great amount of data and improved our understanding of Martian atmosphere. Previous anemometers successfully measured the Martian wind speed in 2D, but they are relatively limited in terms of sensitivity, dimensions of

measurement, updating rate and vulnerability to the environment. To capture the dominant component of the turbulent Eddie spectrum, near surface (1.5m altitude) measurement at 10-20 kHz with a sensitivity of 5 cm/s is required [1]. None of the anemometers that has been sent to Mars can capture turbulent boundary layers on Mars [2]. Most of these sensors were only capable of measuring the wind speed above 1m/s with a response time of 1s [3]. Ultrasonic anemometers generally have high sensitivity, high accuracy, high temporal resolution, demand little power and are insensitive to radiative heating. Therefore, it is superior to the anemometers flown to the Mars in the past [2]. Accurate anemometers are crucial for understanding the near-surface atmosphere environment, for example, slope winds, convective cells, dust devils and Aeolian processes [2]. Furthermore, water fluxes, heat and momentum fluxes between the surface of Mars and atmosphere can also be studied using wind speed measurements. Ultrasonic anemometers are a promising technique for achieving this goal, therefore, understanding the atmosphere environment near the Martian surface. In this thesis, the focus lies in characterizing and selecting ultrasonic transducers that are used to building ultrasonic anemometers so that the transducers will operate properly in Martian atmosphere and transmit signal can be detectable in such environment.

## **1.2 Contributions**

This thesis has demonstrated the capacity of two pairs of ultrasonic transducers to transmit and receive ultrasound in 6 mbar CO<sub>2</sub>: PUI and Kobitone transducers. The thesis has also demonstrated a reliable modeling method that provides high accuracy prediction of the signal strength in the transmission testing as well as time of flight prediction of the ultrasound signal in air and 6 mbar CO<sub>2</sub>. For PUI transducers, the peak value of the model is within 5% difference compared to the measurement peak value. For all of the transducers tested, the time of flight measurement is within 10% of the predicted value in air. PUI transducer model also provided time



of flight prediction within 20% of the measurement in 6 mbar CO<sub>2</sub>. The thesis demonstrates the feasibility of operating an ultrasonic anemometer under Martian conditions.

It is also confirmed that piezoelectric transducers are capable of making both air and 6 mbar CO<sub>2</sub> coupled transmissions. This thesis has cleared ways for testing more piezoelectric and capacitive ultrasonic transducers in the future for an ultrasonic anemometer on Mars.

## Chapter 2 Background

### 2.1 Ultrasound and sound propagation

Ultrasound refers to sound waves with frequencies above 20 kHz, which is the upper limit of human hearing. Animals were found to use ultrasound for navigation. Ultrasound has been used in various applications including navigation, non-destructive testing, range finding, medical imaging, processing and anemometry.

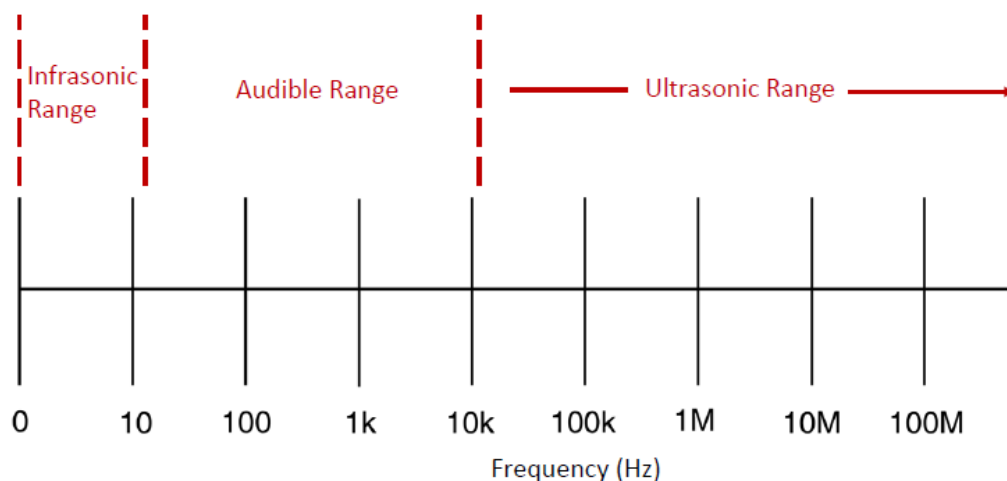
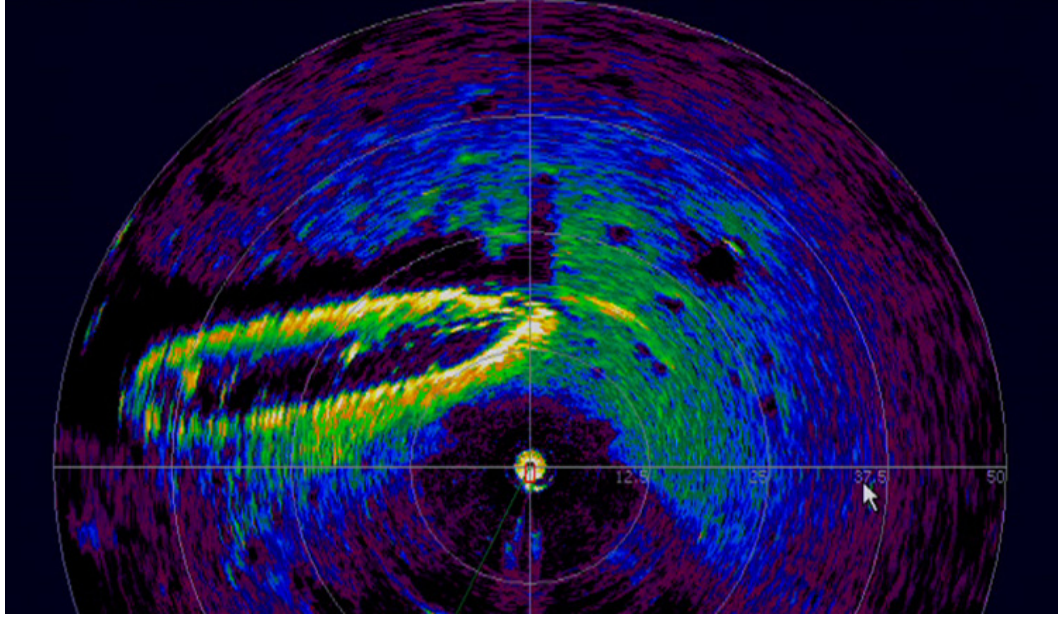


Figure 1 Acoustic range versus frequency

Because of its safe and non-destructive feature, it has become common mechanism for applications in medical field. For example, by using medical ultrasound, physicians can see internal structures of patients' body like tendons, joints, muscles and veins [4]. Most of these devices take advantage of Doppler effects: a 2D ultrasound image can be generated, either by sweeping ultrasonic transducers mechanically or by generating a 1D phased array electronically [5].



**Figure 2 SONAR image of Little Hercules, a wooden-hulled ship wreck in the 19<sup>th</sup> century [6]**

Another important application of ultrasound is SONAR. SONAR has been a technique inspired by bats, which use ultrasound's time of flight to measure the distance of certain objects. It is performed mostly underwater. There are two main types of SONAR based on how it works: active SONAR and passive SONAR. Active SONAR sends out and receives signals that are reflected by the object. Then time of flight can be used to calculate the distance of the object to the ship. Passive SONAR has receivers that "listen" to the signals that are transmitted by an object; therefore, the direction can be measured and the range can be estimated [5].

Ultrasound propagates as the speed of sound. It obeys the wave equation [7]:

$$\nabla^2 p - \frac{1}{c^2} \frac{\partial^2 p}{\partial t^2} = 0 \quad (2-1)$$

For a spherical wave, the harmonic solution for acoustic pressure turns into [7]:

$$p(r, t) = \frac{A}{r} e^{j(\omega t - kr)} \quad (2-2)$$

which represents the geometric spreading of the acoustic wave. This is the first source of signal loss with distance.

The amplitude of the traveling spherical wave is also affected by absorption, thus, the pressure with absorption can be written as [7]:

$$p(r,t) = \frac{A}{r} e^{-\alpha r} e^{j(\omega t - kr)} \quad (2-3)$$

where  $\alpha$  is the absorption coefficient of the media. Depending on the media and the distance of sound travels, the absorption coefficient can significantly attenuate ultrasound signals. This is one of the concerns for ultrasound propagating in 6 mbar CO<sub>2</sub> as absorption coefficient in low pressure CO<sub>2</sub> is much higher than that in atmospheric air at the testing frequencies.

There are three major absorption mechanisms that are crucial for sound transmission: viscosity, thermal conduction and molecular thermal relaxation. For most non-metallic liquids, the absorption caused by thermal conduction is less than that from viscosity [7]. Classical absorption coefficient including both viscous and thermal absorption can be derived:

$$\alpha_c = \frac{\omega^2}{2\rho_0 c^3} \left( \frac{4}{3}\eta + \frac{(\gamma-1)\kappa}{c_p} \right) \quad (2-4)$$

where  $\eta$  is the coefficient of shear viscosity,  $\gamma$  is ratio of heat capacities,  $\kappa$  is the thermal conductivity and  $c_p$  is the phase speed. Importantly, we see that the absorption coefficient grows quickly with frequency, as  $\omega^2$ . According to the mathematical derivations from Williams, the absorption coefficient increases drastically with frequency on Mars in the ultrasound domain [8]. Changing from atmospheric pressure to low pressure CO<sub>2</sub> will alter the absorption coefficient and affect its frequency dependence.

## 2.2 Ultrasound transducers

Ultrasound transducers transmit and receive ultrasound by creating pressure variations through diaphragm motion. There are generally three types of transducers: transmitters, receivers and transceivers. Transmitters convert the voltage to pressure, receivers convert pressure to voltage and transceivers have the functions of both.

Ultrasonic transducers can be split into two categories based on how they are made: piezoelectric transducers and capacitive transducers. For piezoelectric transducers, pressure variation causes the piezoelectric diaphragm to vibrate. Based on piezoelectric effect, mechanical stress caused by vibration of the non-centrosymmetric crystal diaphragm creates electric potential of the transducer, which can be used for calculating pressure variation [9]. The capacitive transducers have two plates that act as capacitors. Vibration of the front plate generates a varying capacitance between the front plate and the back plate, which can be used for pressure calculation. Capacitive Micromachined Ultrasonic Transducers (cMUT) have an array of capacitor element, which can be summed up for ultrasound transmission.

There are a couple of key parameters for an ultrasonic transducer. First is the damping ratio:

$$\zeta = \frac{1}{2Q} \quad (2-5)$$

The Q factor is defined as:

$$Q = \frac{f_r}{\Delta f} = \frac{\omega_r}{\Delta \omega} \quad (2-6)$$

where  $f_r$  is the resonant frequency and  $\Delta f$  is the resonant width, which is the bandwidth of frequencies which power is greater than half of the power at resonant frequency. The damping

ratios are crucial for the ultrasonic transducers as it will directly affect the transfer function of the transducers, both setting bandwidth  $\Delta f$  and the transient time constant  $\omega_n/2Q$  of the transducer.

The second key parameter is the impedance. There are three kind of impedances that are related to an acoustic system. The specific acoustic impedance  $z$  (pressure/ particle speed), the acoustic impedance  $Z$  (pressure/ volume velocity) and the radiation impedance  $Z_r$  (Force/ particle speed) [7]. The specific acoustic impedance has following mathematical expression:

$$z = p / U \quad (2-7)$$

where  $p$  is the pressure and  $U$  is the particle speed. Based on the media, the specific acoustic impedance is the key factor on how much sound can be transmitted from one media to another.

The acoustic impedance  $Z$  is related to the specific acoustic impedance  $z$  by [7]:

$$Z = z / S \quad (2-8)$$

where  $S$  is the surface area. If we want to model electromechanical coupling of the transducers, then radiation impedance is used. The relationship between the radiation impedance and the specific acoustic impedance is expressed as [7]:

$$Z_r = Sz \quad (2-9)$$

### 2.2.1 Piezoelectric transducers

Piezoelectric transducers are transducers that generate and receive ultrasound signals by piezoelectric effects. Piezoelectric effect is an effect that happens on certain crystals and ceramics. When mechanical stress is applied to the material, electrical potential is generated and when voltage is applied to the material, the dimensions of the material change.

Piezoelectric transmission constant  $[d]$  gives the relationship between strain  $[S]$  and electric field  $e$  being applied [10]:

$$[S]=[d][E] \quad (2-10)$$

Reversely, a piezoelectric receiving constant  $[g]$  relates the stress being applied and the generated electric field [10]:

$$[E]=[g][T] \quad (2-11)$$

where  $[T]$  represents the applied stress in  $\text{N/m}^2$ . Piezoelectric material can be aligned in Cartesian coordinate like below.

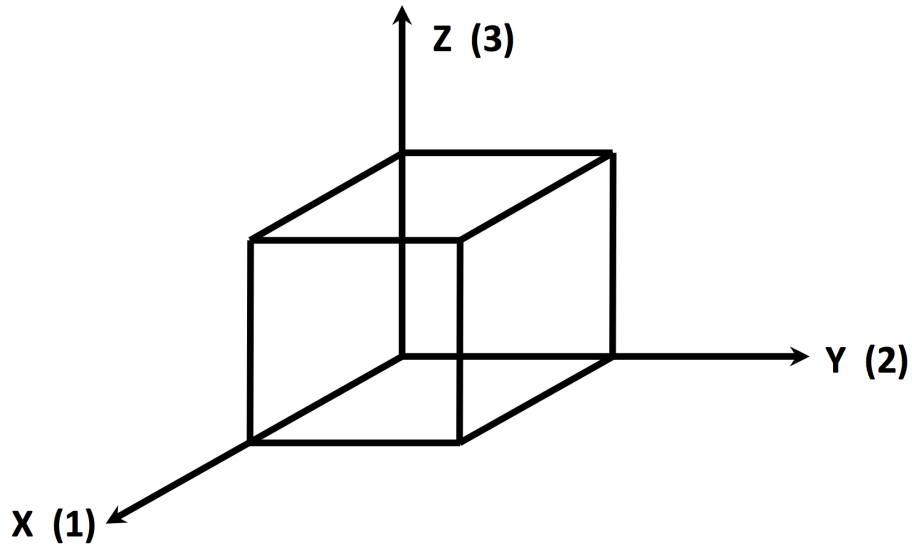


**Figure 3 Cartesian coordinates for piezoelectric material [10]**

We can expand each piezoelectric constant into three directional dependent constants based on the direction of stress/strain and the electric field [10]. For example,  $g_{33}$  represents the induced electric field in z axis due to the stress applied in z axis and  $d_{33}$  represents induced strain in z axis due to the electric field applied. Thickness-mode operation, which includes  $d_{33}$  and  $g_{33}$  is normally most important to ultrasonic transducers.

Input impedance measurement can be used to verify the voltage and current coupling of the piezoelectric transducer in atmospheric air and 6 mbar  $\text{CO}_2$ . Voltages and current were measured for a transducer at certain frequency and an easy model for transducers was set up. Most

piezoelectric transducer's impedance can be modeled by Van Dyke model. A typical schematic of a piezoelectric transducer is shown in Figure 4.

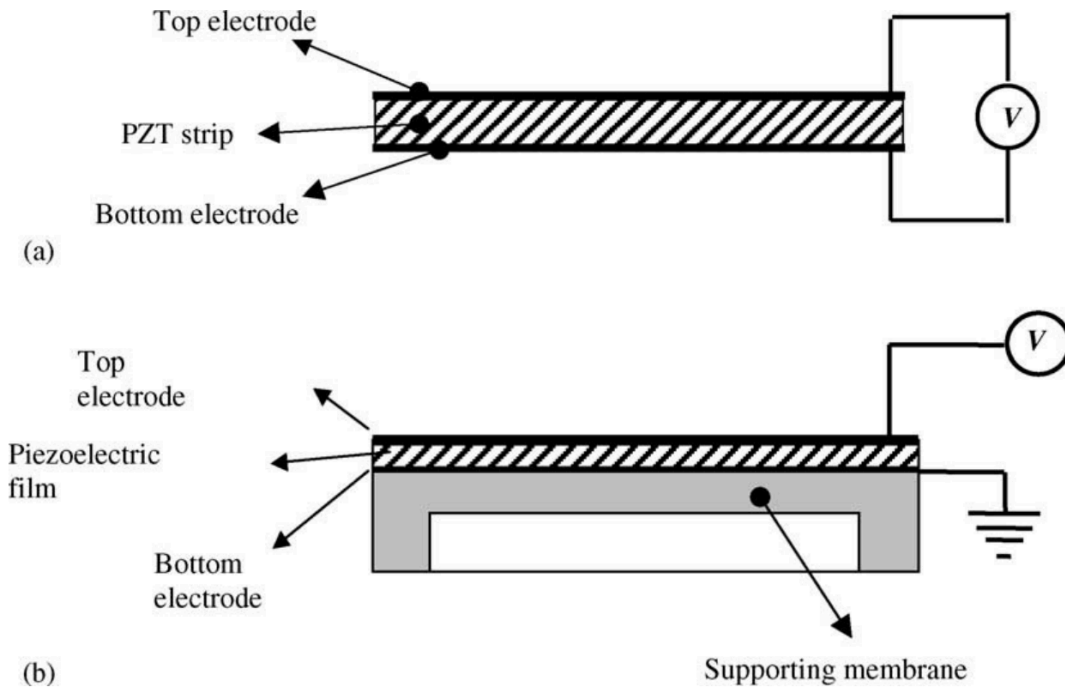


**Figure 4 Schematic of a piezoelectric ultrasonic transducer (a) conventional extensional transducers (b) pMUTs [11]**

There are limitations on the piezoelectric transducers [12]. To begin with, the geometry of the piezoelectric transducers decides that they are normally narrowband with one or two modes. For certain operation that requires a wider bandwidth to operate, the piezoelectric transducers might not be the best choice. Second, the piezoelectric transducers will have a limit on the source strength, since the electric field generated is dependent on the vibration of the plate, which can be limited by the geometry of the transducer. Importantly, piezoelectric transducers can sometimes require high drive voltage. However, typically no external DC bias is required.



### **2.2.2 Capacitive micromachined ultrasonic transducer (cMUT)**

Capacitive micromachined ultrasonic transducers (cMUT) were first demonstrated by Khuri- Yakub in the 1990s [12]. It is micromachined to have two plates: one vibrating diaphragm and one electrode back plate. The variation of distance between the diaphragm and the back plates creates a capacitance, which can be used to calculate the diaphragm movement. The micromachined transducer normally has an array of elements and therefore may include vent holes. AC signals are converted to vibrations of the plates. DC bias is also applied to increase electric field between the plates and to increase power of the signal and sensitivity [13]. In this thesis, a Nickel- on glass cMUT manufactured in our lab was used for testing [14].

In the fabrication process of the Tufts cMUT in our lab, three physical layers were used in the process [15]. This includes one structural layers, one sacrificial layers and one metal layer. Photolithography, physical vapor deposition and electroplating were also used to create the structure. A lumped element model was used for modeling [16].

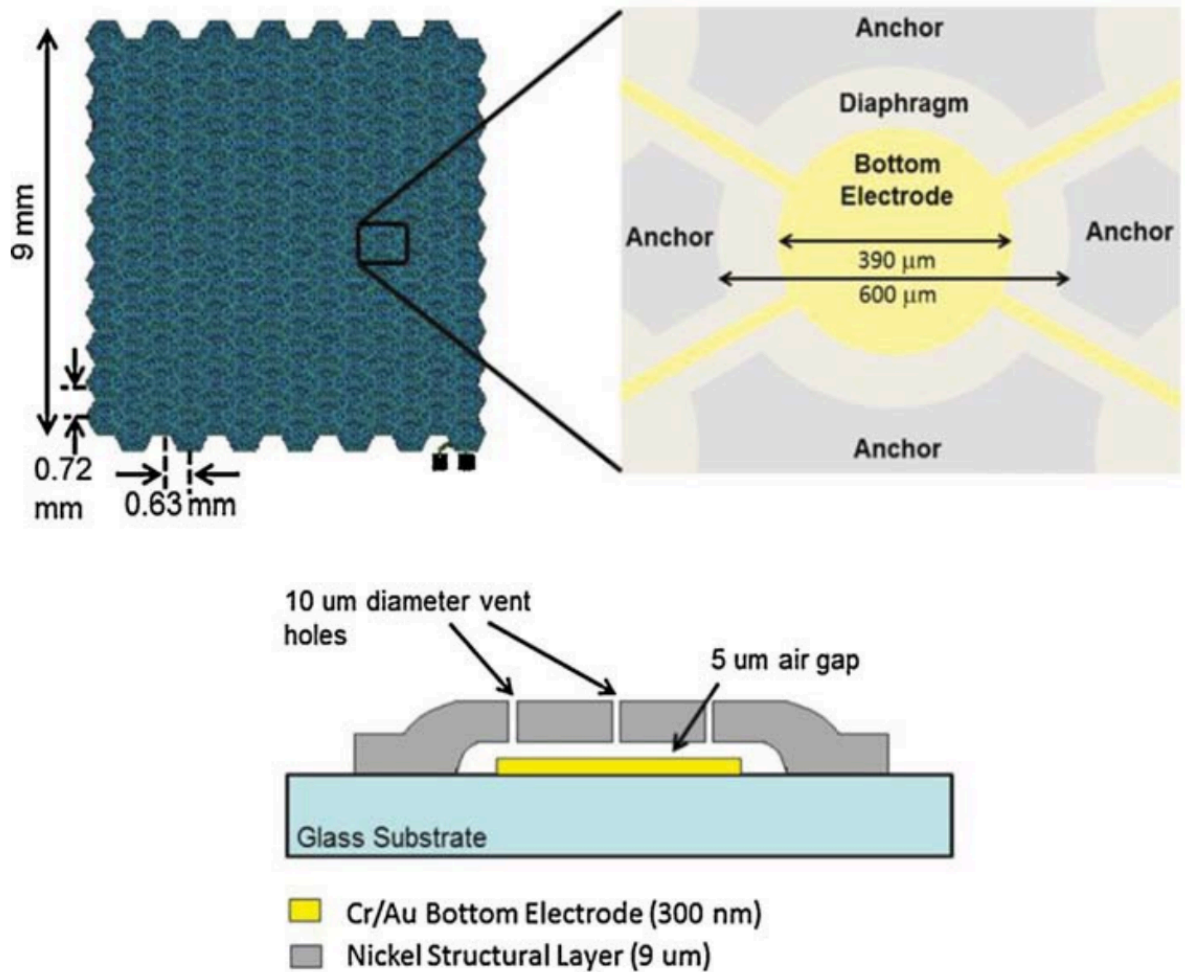


Figure 5 Schematic of a single element in a cMUT array [14]

## 2.3 Anemometers

An anemometer is a device used for measuring the velocity and direction of the wind. Common types of velocity anemometers include: cup anemometer, vane anemometer, hot-wire anemometer, laser Doppler anemometer and ultrasonic anemometer. Aside from measuring wind speed, a hot-wire anemometer can also measure temperature fluctuation level in a turbulent flow [17]. Anemometers have been used in weather stations and are essential to environmental research.

Cup anemometers provide an easy way to measure wind speed. Cups are attached on a vertical shaft, as the wind blows, the cups rotate either clockwise or counterclockwise, which will

rotate the shaft. The dial count per unit time is proportional to the magnitude of the wind speed. A calibration curve comparing wind speed with the dial count can be generated using wind tunnel experiments [18]. Some cup anemometers also have a tail for measuring wind direction.

Common types	Size	Dimensions	Updating speed	Accuracy
Cup anemometer	Large	2D	Slow	Low
Hot-wire anemometer	Small	2D	Slow	Medium
Telltale	Large	2D	Extremely slow	Medium
Ultrasonic Anemometer	Large	3D	Fast	High

**Table 1 Comparison between various anemometers**

Hot-wire anemometers are made from a fine wire that is integrated into a control circuit. The wire is first heated to a set temperature, with a certain rating of voltage and current. As the wind comes through the wire, temperature of the wire will change. To maintain the pre-set temperature, the voltage and the current are changed. The magnitude of the wind speed can then be calculated using the change of voltage and current. The constant temperature on a hot-wire

anemometer has a short response time as well as good spatial resolution in earth atmosphere; therefore it is suited for measuring fluctuating gas velocities on earth [19].

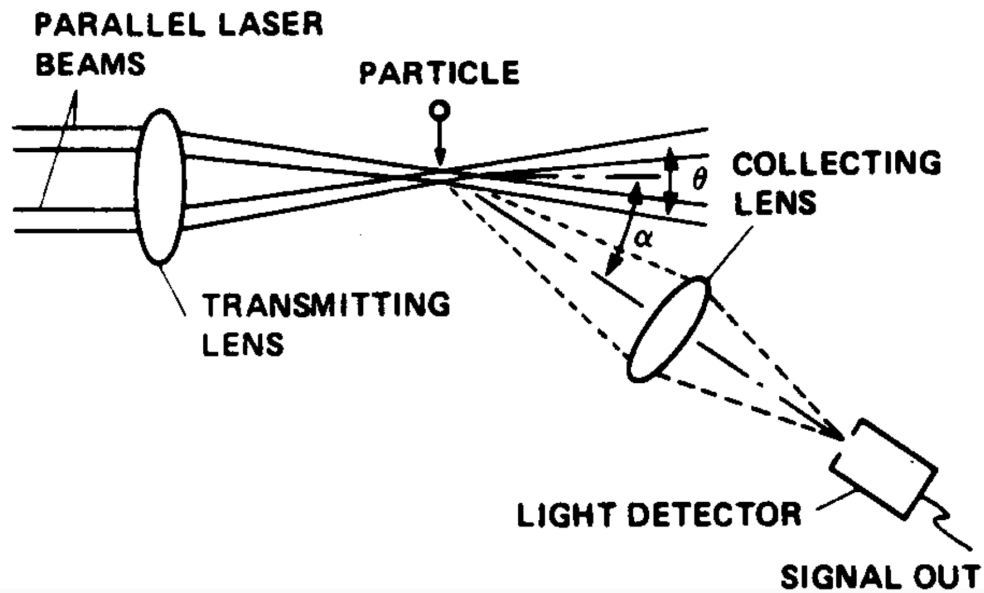
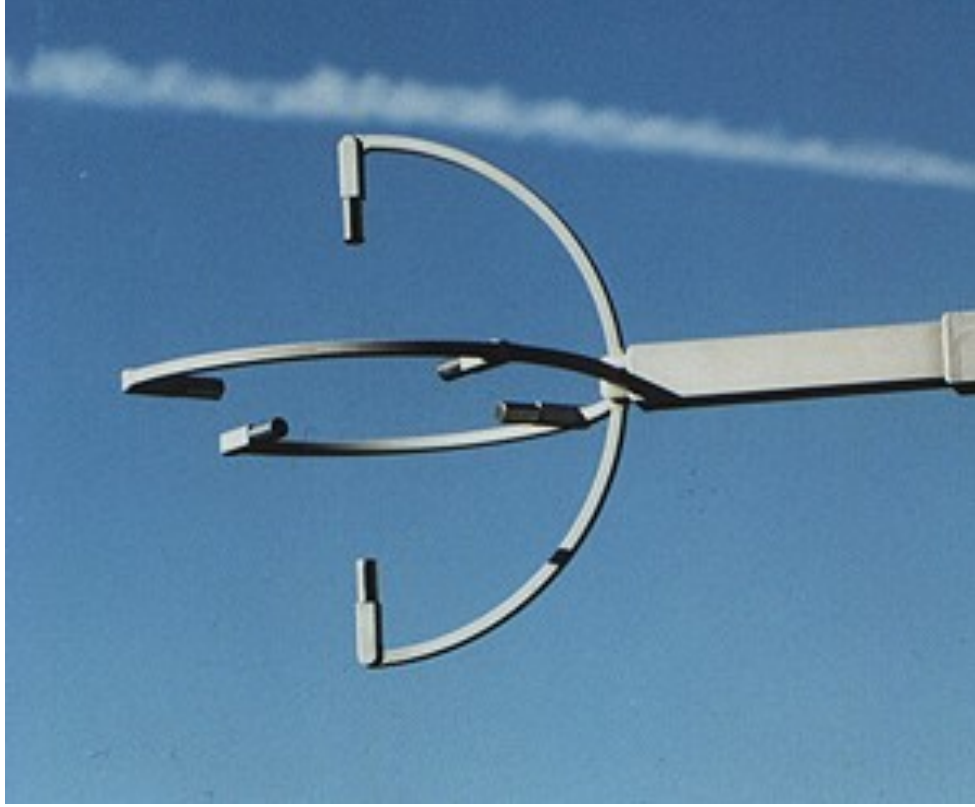


Figure 6 Simplified schematic of a dual beam Laser Doppler Anemometer [20]

Laser Doppler anemometer uses the interference of laser light to determine the speed of wind flowing through. It provides non-invasive measurement of the velocity probability distribution within a volume element, with high spatial resolution [21]. Laser light, beam splitter (normally a Bragg cell), optical lenses are used to create fringes. The wind flow passing through the probe volume will create a scattering pattern, which contains the Doppler effect information. The frequency shifted can be then analyzed by Fast Fourier Transform (FFT). 3D velocity can be measured using two probes.

Ultrasonic transducers are commonly used in weather stations and atmospheric research on earth. A common setup for an ultrasonic transducer can be found in Figure 7.



**Figure 7: Common setup for an ultrasonic anemometer [2]**

In 1D setting, if we set two transducers a distance  $L$  apart, we can measure time of flight for both direction as  $t_1$  and  $t_2$ . If we assign the parallel component of wind speed as  $V_w$  and the speed of sound as  $V_s$ . Then we have:

$$\frac{1}{t_1} = \frac{V_s + V_w}{L} \quad (2-12)$$

$$\frac{1}{t_2} = \frac{V_s - V_w}{L} \quad (2-13)$$

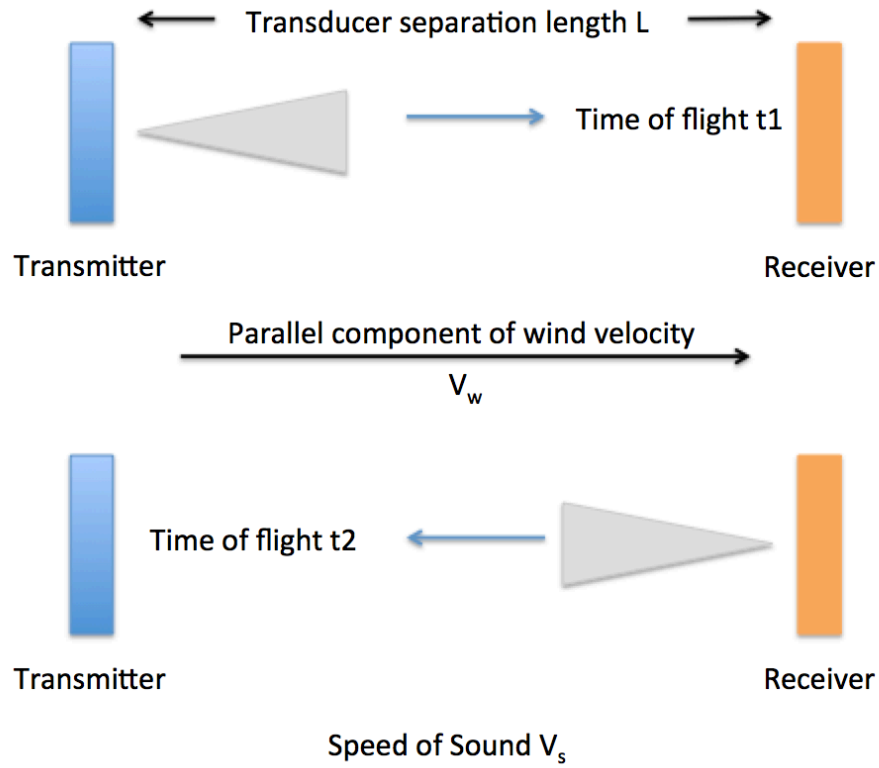


**Figure 8 1D demonstration of transmission for an ultrasonic anemometer**

Wind speed in that dimension can be solved:

$$V_w = \frac{L}{2} \left( \frac{1}{t_1} - \frac{1}{t_2} \right) \quad (2-14)$$

$$V_s = \frac{L}{2} \left( \frac{1}{t_1} + \frac{1}{t_2} \right) \quad (2-15)$$

By using three pairs of ultrasound transducers, 3D wind speed, which includes magnitude and direction as well as the speed of sound can be measured. Ultrasonic anemometers have a fast response time. If we set the distance of the transmitter and receiver to be less than 1 meter away, a linear chirp (swept sine) signal can be transmitted and received using less than 3 milliseconds in atmospheric air. This allows a faster updating rate of the wind speed measurement. With further analysis, we could analyze heat flux for the wind in a greater resolution [22].

## **2.4 Mars**

Mars was named after the Roman God of War. For all the planets in the solar system, it is most similar to Earth in the length of day and the average speed of orbiting sun. Therefore, research has been done on the habitability of Mars based on the physics, biology and environment in the past decades [23]. Although there are a lot of similarities between the two planets, the atmosphere is quite different. The atmosphere of Mars contains 96% of Carbon dioxide, 1.9% Argon and 1.9% Nitrogen [24]. The average on Martian surface is about 600 Pascal, which is 6 mbar.

The recorded observation of the planet Mars dates to 2<sup>nd</sup> millennium BCE by the Egyptians. The Babylonians, Early Greek have all made observation of Mars since then for various reasons [25]. In 1610, Galileo Galilei has made first observation of the Planet by using a telescope. With the help of orbiters, landers and rovers, we've come to know the red planet a lot. But to further understand the history of formation of Mars, we have to know more about the planet about its atmospheric properties, chemical composition and physical properties.

### **2.4.1 Martian surface wind and dust devils**

Dust devils are particle laden convective vortices formed by strong insolation of the surface. Dust devils were first discovered on the Martian surface from Viking orbiter images during the late 1970s by Thomas and Gierasch from the Viking orbiters (1985), and later confirmed by Ryan and Lucich (1983) who identified dust devils from Viking Lander meteorological data:

the Martian dust devils have a typical peak tangential wind speed of 30 m/s whereas the on earth the peak tangential wind speed of dust devils is 10 m/s [26].

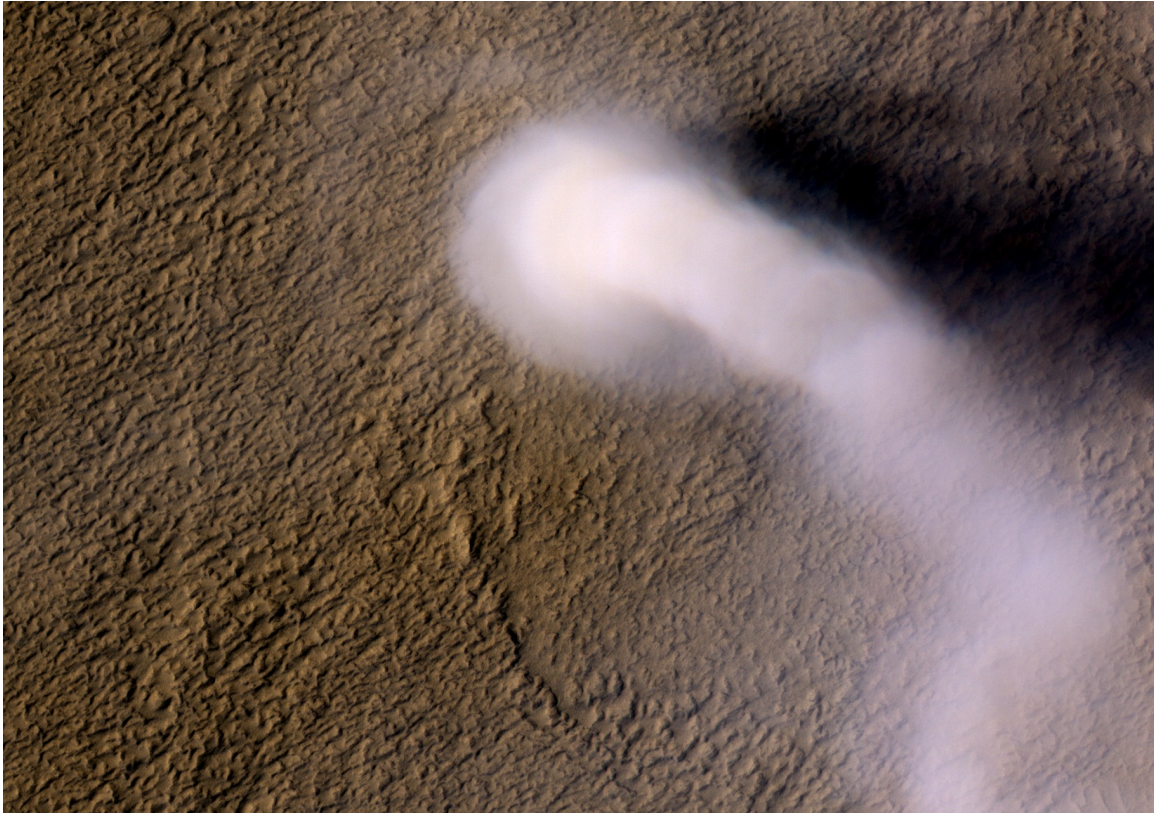


**Figure 9 A dust devil on Northern Mars captured by NASA's Reconnaissance Orbiter [27]**

Wind speed, pressure, temperature and dust loading are all important parameters if we want to have a better understanding of the dust devil on Mars. Although past Mars missions have provided us a lot of information about wind speed in horizontal direction, there is still a lot more we can study. An ultrasonic anemometer consists of three pairs of ultrasonic transducers, which enables measurements of the wind speed in 3D, and it is important for us to study Reynold stress. The past anemometers were only capable of measuring wind speed at 1 Hz maximum. Because of the faster wind speed of dust devils, a faster updating rate of 10-20 Hz is also extremely useful for measuring dust devil on Mars and achievable by ultrasonic anemometers.



## 2.4.2 Mars Exploration and Wind Speed Measurement

Mars exploration programs have started by the US and the Soviet Union in the mid-20th century. The first successful flyby of the planet Mars was made by the Mariner 4 from NASA, which took the first picture of the Martian surface. Two of the Soviet probes are the first to contact Martian surface. In 1975, the Viking 1 lander safely landed on the Mars surface, which is the first mission to successfully land on Mars. The mission has discovered the existence of Nitrogen in Martian atmosphere, which has never been discovered before [28]. There have been various successful landers and rovers with different purposes throughout the years since the Viking Program. The knowledge of the surface and atmosphere properties has been greatly increased through these explorations.

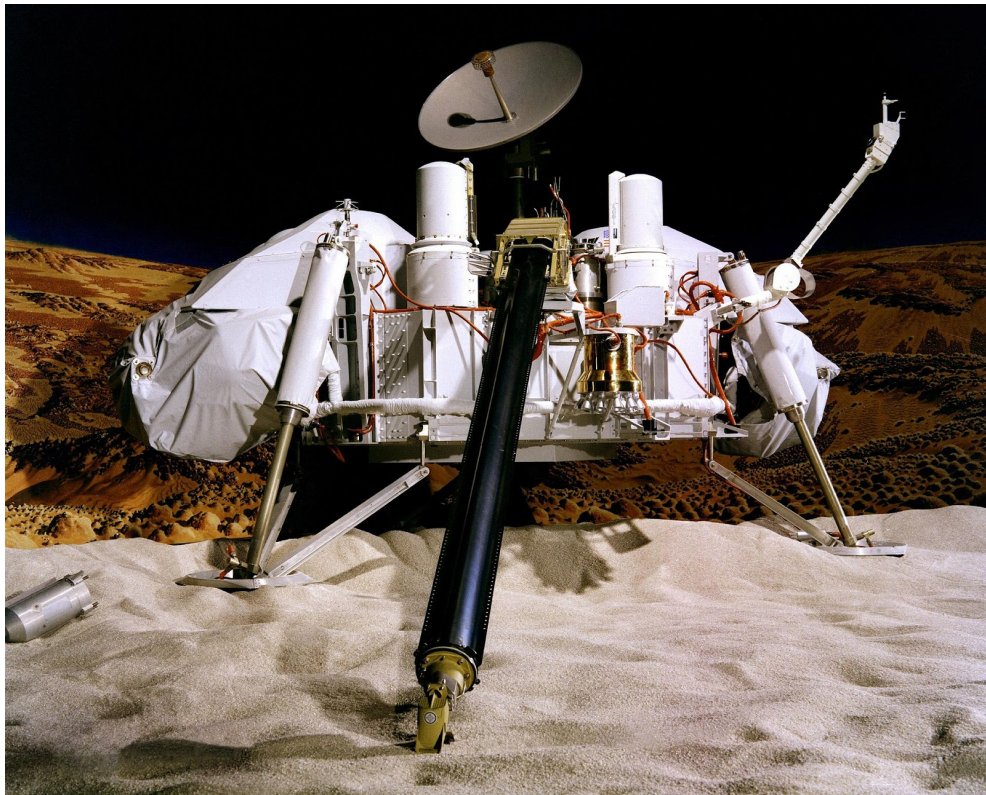
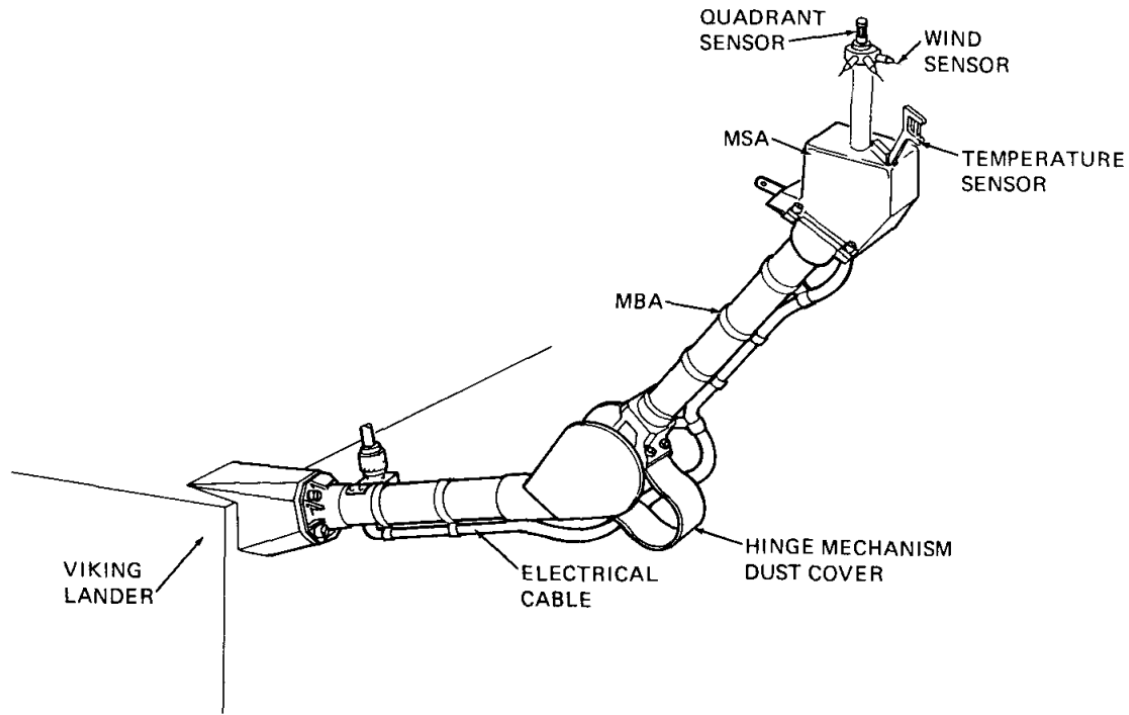


Figure 10 Model of a Viking lander [29]

Source	0240 LLT		0701 LLT		1122 LLT	
	Module Mean	20-Sol Mean	Module Mean	20-Sol Mean	Module Mean	20-Sol Mean
Wind speed, m/s	3.4	2.5	4.0	3.3	6.7	6.8
Wind direction, deg	204	201	240	223	187	192
Temperature, °K	192	190	199	198	234	234

**Table 2 Comparison of Module Mean Data with the 20-Sol Mean Results at the same LLT (Local Lander Time) for wind speed, direction and temperature on the Viking Lander [30]**

Wind speed measurements have been crucial to the understanding of the Mars atmosphere and weather changes. To measure the wind speed on Mars, an anemometer is normally used. The Viking program includes two spacecraft (Viking 1 and 2) that were launched in the 1970s. Both landers that were carried by Mars orbiters landed successfully on separate locations in the northern hemisphere of Mars. Valuable scientific data was measured and recorded. The Viking landers carried two hot-film sensors that were 90 degrees apart. The hot-film sensors were maintained at nominal 100°C above the ambient temperature and provided wind speed and direction measurements in 2D [31]. The accuracy of wind speed measurement is about 10% over the most range (2-150 m/s) and the overall accuracy of wind direction measurement is about +/- 10 degrees [30].



**Figure 11 The hot-wire anemometer model on the Viking lander [26]**

The Pathfinder spacecraft, which consists of a rover, landed on Mars in the 1990s. The rover, named as “Sojourner”, became the first rover to successfully operate on Mars, and wind speed was measured at various locations on Mars surface. To measure the wind velocity and direction, a six segment hot-wire anemometer was used. The wires were heated by a current that pass through six segments and the wind speed and direction are calculated using temperature differences between low and high current in each segment [32]. Dust devils were imaged, and speed was measured using the sensor. The wind speed measurement was straightforward, but issues exist in the calibration of the hot-wire electronics and the sensitivity of the wind socket for determining direction. It was also a concern that the position of the windsock relative to other components or materials on the rover might not be ideal, because wind direction could be altered by airbag materials on the rover [33].

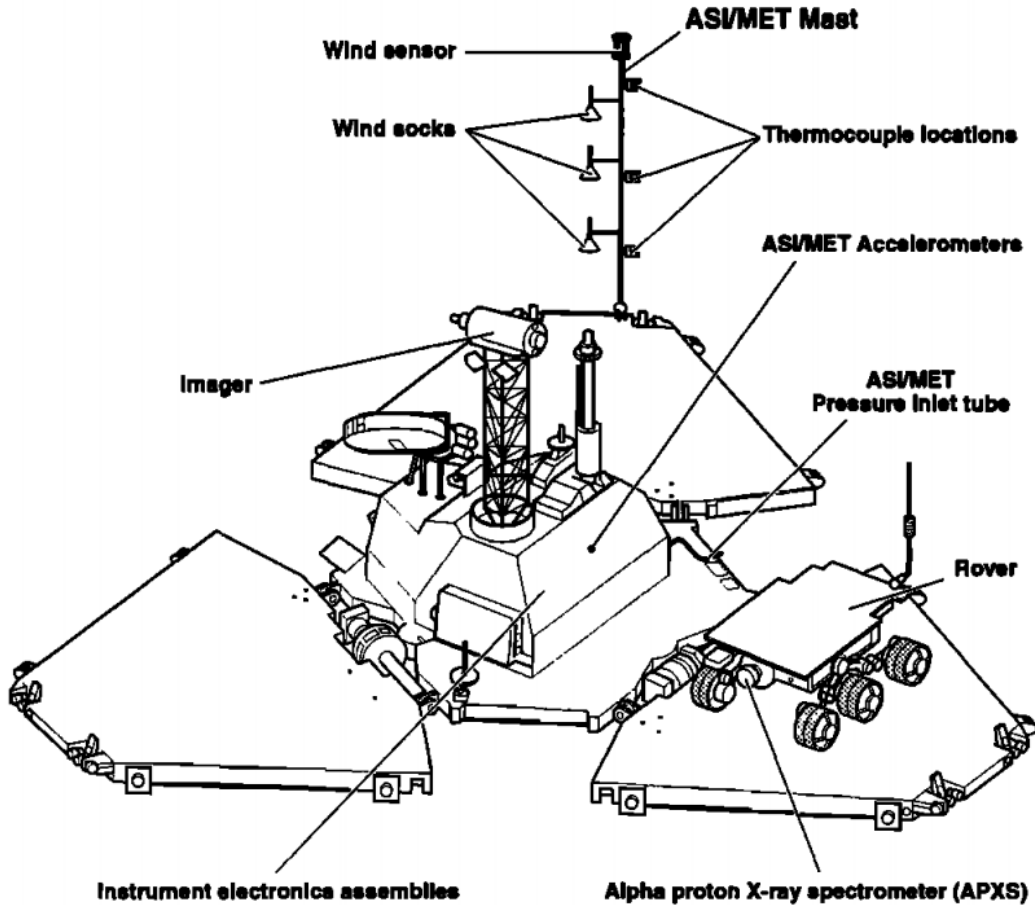


Figure 12 Pathfinder Rover Schematic [34]

The Phoenix spacecraft was sent to Mars in 2008, aimed to explore the polar environment on Mars. A Meteorological Station (MET) was installed to help access the weather on Mars on a regular basis. The Telltale was included on the MET of the Pathfinder rover as the wind speed and direction sensor. When the wind blows, the deflection occurs on the Telltale. The amount of deflection from vertical axis determines the wind speed and direction is determined by which way it blows. The pictures of the deflection were then analyzed. The imaging system had an accuracy of 0.3 pixels and the Telltale were theoretically modeled and verified in 2D [35], but the speed of measurement was slower than 1 sample/s since it requires photographing to return [36].



**Figure 13 Telltale wind indicator on Phoenix [35]**

Curiosity Rover from the Mars Science Laboratory was launched in 2011. The rover consists of a REMS (Rover Environment Monitoring Station) with a hot-wire anemometer for wind speed measurement. Ultrasonic anemometers have not been used for wind speed measurement on any of the Mars missions before.

Ultrasonic anemometers can provide us measurements of both horizontal data and vertical wind speed, which can be used to calculate the Reynolds' Stress (RS). The signals received for all direction can also be used for power spectral analysis, friction velocity and heat flux [37]. The design goal for the ultrasonic anemometer is to be able to measure wind speed from 0-40 m/s with sensitivity of 0.05 m/s. Plans have been made for sending landers and orbiter to the red planet in the coming years by several countries, including the Mars 2020 rover from NASA, ExoMars rover by the European Space Agency, Yinghuo 2 from Chinese Space Agency and SpaceX Red Dragon. These could all be good opportunities for an ultrasonic anemometer to operate on Mars.

### **2.4.3 Need for a better method**

Although anemometers on previous Mars missions have provided us valuable data of the 2D horizontal wind speed, the previous wind speed measurements on Mars are relatively limited. None of the anemometers are capable of measuring wind speed in 3D. The hot-wire anemometer was difficult to calibrate after it was sent to Mars: the varying temperature on Mars surface and solar radiation all generate difficulties for calibration. Also, due to the low atmospheric pressure on Mars, the heat loss is a lot slower than that on earth, which will cause a slower updating rate. Telltales can measure the wind speed by using the angle of deflection, but they require the use of large quantities of resources, such as high-resolution camera and downlink data volume [38]. The updating speed of telltale is also extremely slow. The wind sock had a sensitivity issue: it turns out the wind sock were too heavy for some of the light wind to register.

Ultrasonic anemometers have been used on earth in various fields and locations. It can be used not only in weather stations, but also in environmental research such as Aeolian sediment transport. It can provide measurements on quasi-instantaneous velocity fluctuations, Reynolds Stress, turbulence spectra and resultant two and three dimensional flow vectors [39]. Ultrasonic anemometers have the potential to overcome these limits: the target specifications for this instrument are a high time resolution (100 Hz), high sensitivity (5 cm/s) and it measures wind speed from 0-40 m/s in 3D [2]. The signal processing electronics can also be calibrated remotely. 3D wind speed can be studied for deeper understanding of turbulent flow boundary layer and other properties of the Martian atmosphere.

### **2.4.4 Challenges for ultrasonic anemometer operating on Mars**

There are a couple of factors that will be different for ultrasonic transducers on Mars that we need to overcome. The first factor is the air density. Moving the anemometer from atmospheric

pressure (101000 Pa) to 6 mbar (600 Pa) will reduce the air density drastically, therefore affecting the source strength of the transducer. Such change will introduce a signal loss of 44 dB.

The second factor is the transducer transfer function. Moving from atmosphere to low-pressure CO<sub>2</sub>, the mechanics of the transducers may go through following change: shift in resonance frequency; change in damping ratio and change in effective mass and capacitance. These factors are directly related to the transfer function of the transducers. Therefore, in atmospheric air and low-pressure CO<sub>2</sub>, for same AC voltage applied to the transducers, the pressure generated will be different; for same pressure applied on the diaphragm, the voltage generated will be different as well.

The third factor is the attenuation of low pressure CO<sub>2</sub>. Based on the theoretical work done by Williams, the absorption coefficient on Mars is about 4.4 Np /m at a frequency of 40 kHz at 220 K. Depending on the size of the anemometer and the distance between the facing transducers, this will introduce a 38.2dB/m loss at 40 kHz at 220 Kelvin. The absorption coefficient increases rapidly with frequency in the ultrasound range so at 150kHz at 220 Kelvin, the absorption coefficient on Mars will be 58 Np/m [8].

The fourth factor is that the speed of sound changes from atmospheric air to 6 mbar CO<sub>2</sub> will lead to a change in diffraction gain/ loss of sound. This will be a minor effect comparing the other effects.

Lastly, just like on earth, there will also be ambient acoustic noise and electrical noise on Mars. The electrical noise will be not much different from the noise on earth. Just like the acoustic signal, the acoustic noise will undergo absorption in Martian atmosphere. This means that most of the acoustic noise will not be able to transmit over 1 meter on Mars. The acoustic source mainly comes from wind noise fluttering. We want to make sure the received signal has high enough

signal to noise ratio so that by using cross correlation, we can figure out the time delay for both of the simulation here on earth and in Martian atmosphere.

Combining these factors, we can conclude that the density change, which directly affects source strength, is the primary difficulty we need to overcome if we want to use ultrasonic anemometer on Mars. A secondary concern is changes that the transducer transfer function may undergo due to the pressure change. No commercially available ultrasonic anemometers have been found that can transmit and receive ultrasonic signals in 6 mbar CO<sub>2</sub>. To achieve this goal, a combination of transducers and electronics with relatively high gain is required. Once the signal is received, the signal can be analyzed using Digital Signal Processing technique for anemometers.



## Chapter 3      Testing Methods

### 3.1 *Selecting transducers*

For successful testing, a wide range of ultrasonic transducers were considered and tested. A few selection criteria for the transducers were considered. First, there are limits on voltage applied to the transducers. The power supply on the Mars Rover will have limited power output. Therefore, transducers that were selected generates ultrasound with a maximum AC voltage of  $40 V_{pp}$ .

Damping ratio of the transducer is another factor for selection. We have observed saturation in the beginning of time domain signals for some of the transducers. This happens because that in our device there are only two channels. When signals are being sent from one channel, the receive amplifier on the channel picks up the drive voltage and saturation forms and rings down. If the Q factor of a transducer is high, the damping ratio of the transducer will be small, the received signal will be a lot longer in time than the signal being sent. Therefore, ultrasonic transducers with a relatively smaller change in damping ratio from air to 6 mbar CO<sub>2</sub> or with a higher damping ratio in 6 mbar CO<sub>2</sub> are preferred in our experiments.

Furthermore, the transducers should have an appropriate resonance frequency so that it is close to the central frequency of the electronics transfer function. A higher gain of the signal can be achieved if all of the transfer functions in the system have high gains at the testing frequency.

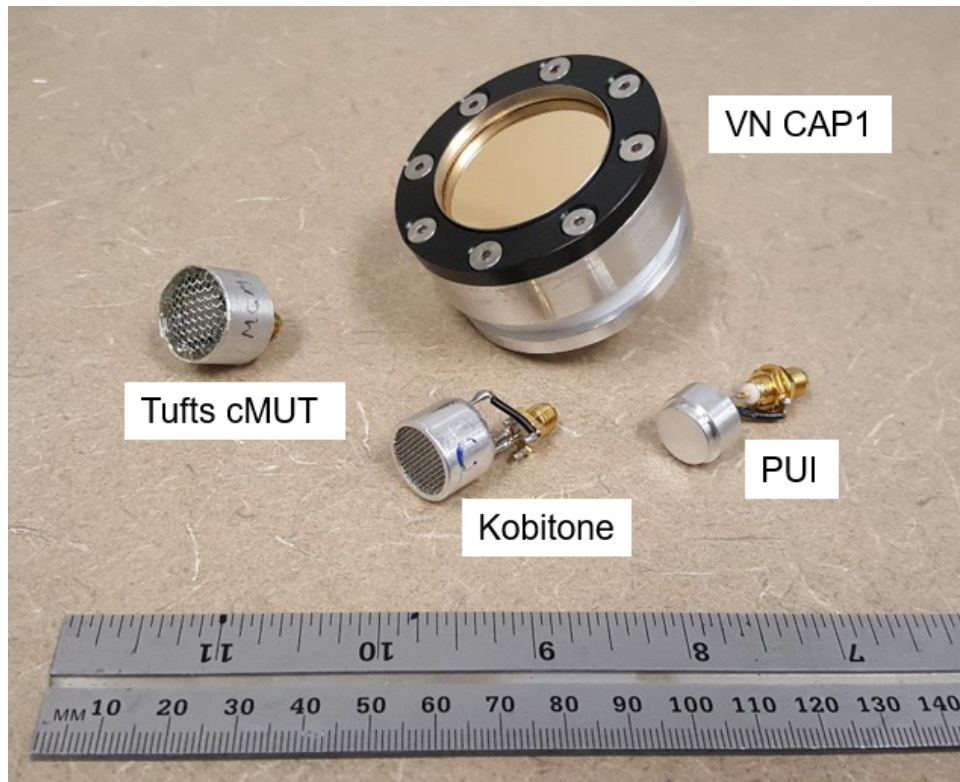


**Figure 14 Ultrasonic transducers that were tested**

Four transducers were selected based on their properties as you can see in Table 3 below. The transducers are soldered with BNC or SMA cable, which are then tested in atmospheric air and 6 mbar CO<sub>2</sub>. Two of the transducers are commercialized piezoelectric transducers: PUI and Kobitone transducers. Tufts cMUT transducers are designed and manufactured in our lab and CAP1 transducers are provided from VN instrument [14].

Transducers	Drive AC Voltage ( $V_{pp}$ )	Central Frequency (kHz)	Datasheet Bandwidth in atmosphere (kHz)	DC Bias (V)	Outer Diameter (mm)
Kobitone 255-400PT160-ROX	28.3	40	2	0	$16.2 \pm 0.2$
PUI UTR-1440K-TT-R	140	40	1.4	0	$14.4 \pm 0.3$
Tufts cMUT	20	280	100	10-30	$19 \pm 0.2$
VN instruments CAP1	20	68	55.3	220	$57.5 \pm 0.2$

**Table 3 Basic properties from datasheet of the transducers tested**

## **3.2 Parameters**

Transducers were characterized using Laser Doppler Vibrometry and Input Impedance measurements. Models were fitted to the measurement and parameters were calculated for the transducers.

### **3.2.1 Laser Doppler Vibrometry (LDV)**

Laser Doppler Vibrometry was applied to all the transducers that are being tested and parameters for these transducers were determined. Light waves transmitted by the laser were focused on the surface of the diaphragm on the transducers; photo detector receives the reflected light waves and frequency shift were analyzed. In such application, there are usually two ways for extracting the Doppler frequency information: Mach- Zehnder interferometer and the Michelson interferometer [40]. If the diaphragm of the transducer is stationary (no AC voltage applied to the transducer), then the frequency of light waves received will be the same with the frequency of light waves that are being transmitted. After the transducers being driven by certain AC voltage with

operating frequency, the diaphragm will be vibrating, creating a frequency shift on the incoming waves, so the received wave will have a different frequency at the specific point on the diaphragm that is being tested. Frequency shift can be then used to simulate the vibration under certain AC voltage drive [14]. For all four transducers, both LDV of a single point and scanning LDV of the transducer surface were done. For the single point LDV measurement, we can model the displacement as a second order transfer function as you can see in the red line below.

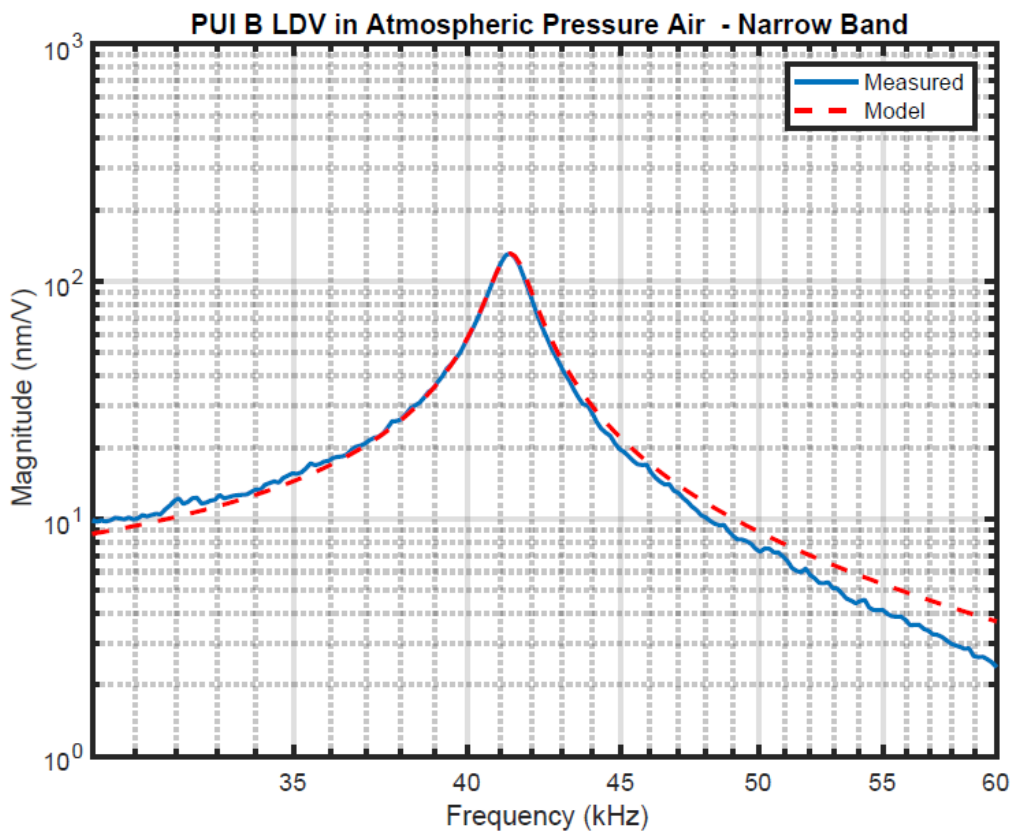


**Figure 15 LDV measurement for PUI-B transducer at a single point across frequency**

The LDV surface scan provides a maximum displacement of points across the surface of the transducer diaphragm, which can be seen in the figure below. Unlike the other three transducers, CAP 1 transducer displays a non-modal vibration pattern at all frequencies tested from

30 kHz to 100 kHz range. The peak amplitude of the transducers is smaller than the other three, but due to the larger diaphragm size, a larger source strength is expected.

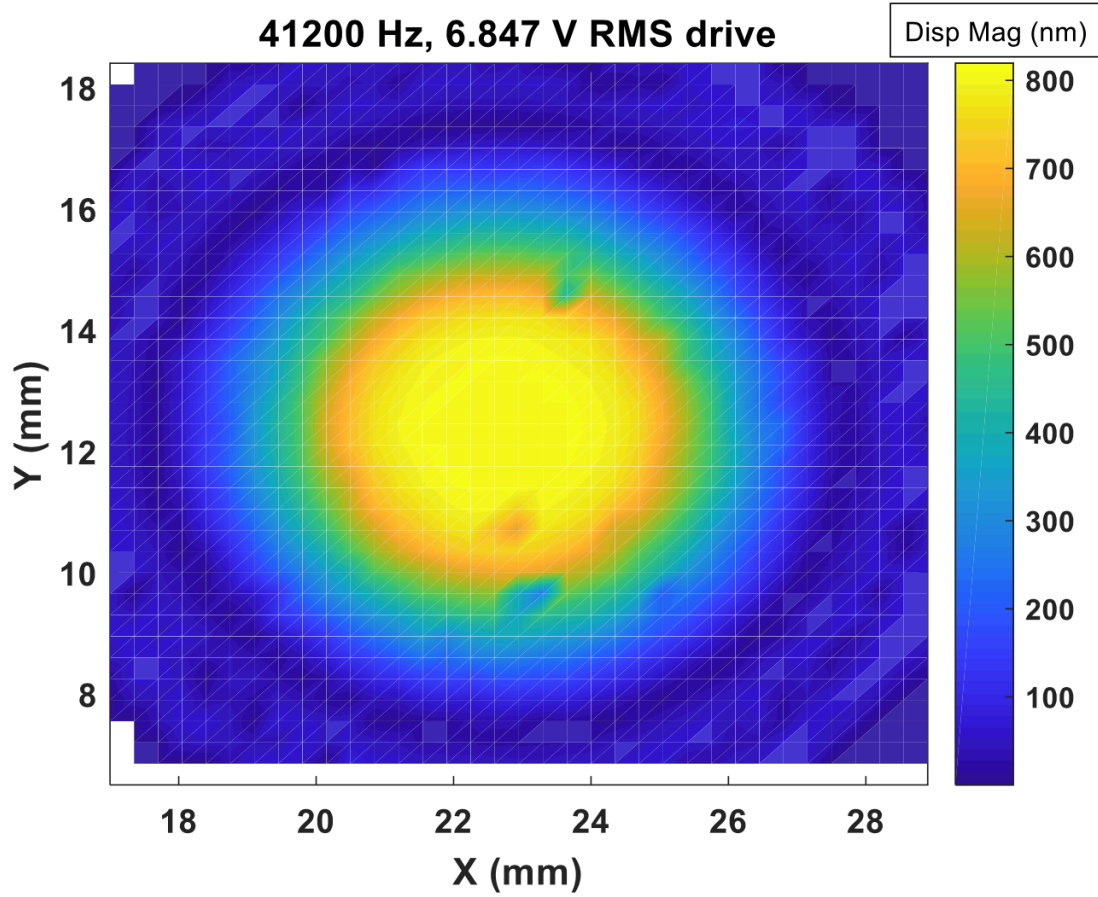


Figure 16 Surface LDV scan of PUI-B transducer at 41200 Hz

The models for all other transducers can be found in the appendix. Using LDV, the following results have been determined.

	Center frequency (kHz)	Resonance frequency $f_r$ (kHz)	Peak displacement (nm/V)	$k_p/m$ (N/(V·kg))	Q	-3dB beam width	Effective Surface area (m <sup>2</sup> )
PUI	41.3	41.3	131.2	276	32	$\pm 42^\circ$ at $f_r$	$3.1 \cdot 10^{-5}$
Kobitone	39	39	55.2	126	26	$\pm 45^\circ$ at $f_r$	$6.9 \cdot 10^{-5}$
Tufts cMUT	291	284	1.2	1000	3.1	$\pm 5.5^\circ$ at 245 kHz	$1.8 \cdot 10^{-4}$

Table 4 Transducer parameters based on LDV model in air

Using the LDV data, a farfield beam pattern was calculated using the Rayleigh integral. To calculate Rayleigh integral, same frequency with LDV surface scan was used. It is also worth noting that the beam pattern is a function of frequency: a higher testing frequency results in narrower beam width and a lower testing frequency results in a broader beam width. For the piezoelectric transducers tested, the beam width is wide, it was calculated that the acoustic source will have a broad beam width for any of the frequencies within the testing range (39.25-41.75 kHz). For CAP1 and Tufts cMUT transducers, a relatively narrower beam width was calculated. More beam pattern can be found in appendix.

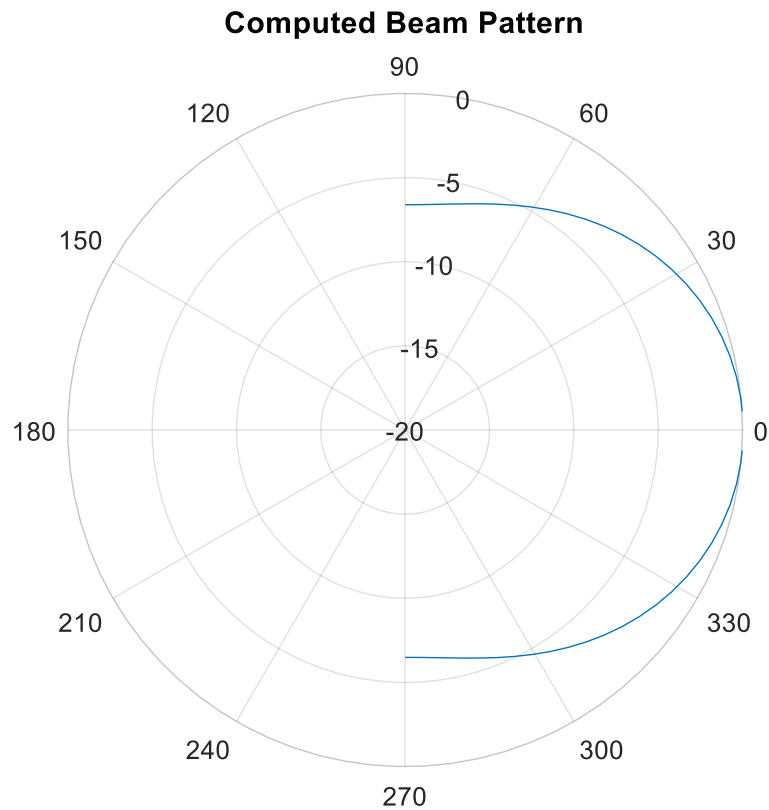


**Figure 17** Calculated beam pattern for Kobitone transducer using LDV

### 3.2.2 Input Impedance measurement

Input impedance measurements were done for all ultrasonic transducers in atmospheric air and 6 mbar CO<sub>2</sub> and both real and imaginary impedance were plotted. Input impedance measures the opposition of current flow. We measure the input voltage at different frequencies at the input terminal and the current in series with the signal generator. Input impedance can be plotted across frequencies as:

$$Z = \frac{\text{input voltage}}{\text{input current}} = \frac{V_{in}}{I_{in}} \quad (3-1)$$

where voltage is measured across the input terminals and the current is measured in series with the load. The measured complex input impedance can be plotted in terms of resistance R and reactance X:

$$Z = R + jX \quad (3-2)$$

Impedance model was created for the transducers. Input impedance can be compared with modeled data and electromechanical coupling can be derived. Using the input impedance modeling parameters in air and CO<sub>2</sub>, we were able to calculate the resonance frequency, Q factor, equivalent capacitance C and resistance of the transducers in air and CO<sub>2</sub>. The equivalent electrical inductance L was also calculated, which is equal to  $m/k_p^2$ . The parameter m represents the effective mass of the transducer and  $k_p$  represents the electromechanical coupling coefficient of the transducer.

	Center Frequency (kHz)	$\text{kp}^2/\text{m} ((\text{N/V})^2/\text{kg})$	C (pF)	Q factor	Damping ratio
PUI-B in air	41.7	4.89	1617	49	0.01
PUI-C in CO <sub>2</sub>	41.4	5.57	1624	36	0.013
Kobitone-C in air	40	7.63	3018	35	0.014
Kobitone-C in CO <sub>2</sub>	40.49	9.37	3022	168	0.003
cMUT1-40 in air	332.4	12.3	179	4	0.125
cMUT1-51 in CO <sub>2</sub>	151.6	9.66	154	27.4	0.018

**Table 5 Transducer parameters from input impedance model**

Figure 18 shows the input impedance measurement and model in the same plot. LDV were done for PUI-B and PUI-C, which are different sensors for the same model. CMUT 40 and 51 are also different transducers made in our lab for the same model. For most transducers, we could expect a shift in transducer mechanics: since the air pressure changes, the air resistance for vibrating plate will also change. From these measurements and modeling we can conclude that PUI transducer doesn't have a huge shift in mechanics shifting from atmospheric air to 6 mbar CO<sub>2</sub>. Comparing to PUI transducers, Kobitone transducers have a relatively larger shift in damping ratio in two pressure conditions. Comparing to PUI transducer, which is a solid block of piezoelectric material, the Kobitone transducer is a thinner disk of the piezoelectric material, which is more heavily influenced by interaction with the fluid. The central frequency for Tufts cMUT transducers shifted from 332.4 kHz to 151.6 kHz due to the pressure change. The mechanics changes in Kobitone, Tufts cMUT and CAP1 is mainly due to the density change in air in both of the backing cavity and the environment. More input impedance plots can be found in appendix.



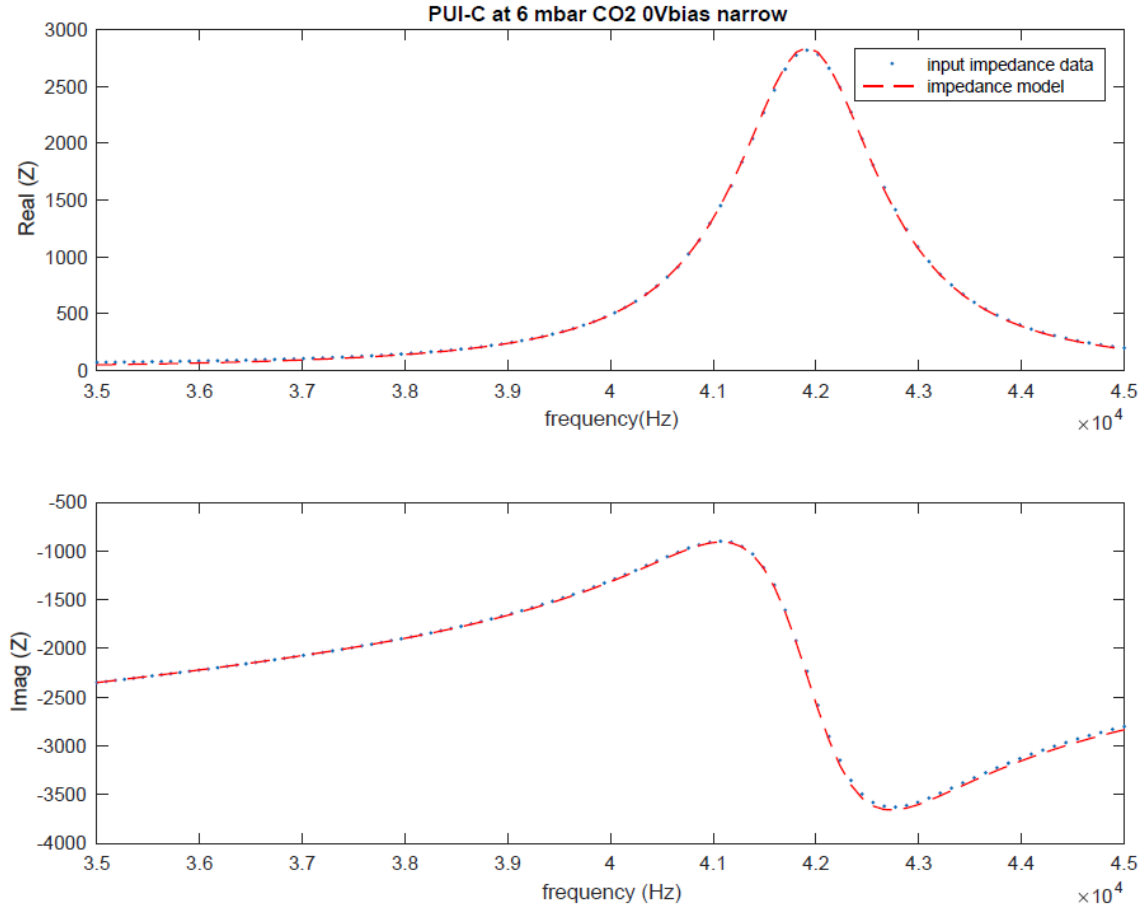


**Figure 18 Example of input impedance modeling of PUI transducers in 6 mbar CO<sub>2</sub>**

### 3.2.3 Combining LDV and Input impedance measurement results

In the LDV model, we determined that the electromechanical coupling over effective mass  $k_p/m$  in air. We have also determined the value of  $k_p^2/m$  from the input impedance model. Thus, both coupling coefficient  $k_p$  and effective mass  $m$  can be calculated for these transducers in air and 6 mbar CO<sub>2</sub>. Since the coupling coefficient  $k_p$  is the same for both air and 6 mbar CO<sub>2</sub> conditions, the effective mass will be different in two pressure conditions.

	$k_p^2/m$	$k_p/m$	Electromechanical coupling $k_p$ (N/V)	Effective Mass $m$ (kg)
PUI in air	4.89	276	0.018	$6.4 \cdot 10^{-5}$
PUI in CO <sub>2</sub>	5.57	314	0.018	$5.6 \cdot 10^{-5}$
Kobitone in air	7.63	126	0.061	$4.8 \cdot 10^{-4}$
Kobitone in CO <sub>2</sub>	9.37	154	0.061	$3.9 \cdot 10^{-4}$
Tufts cMUT1 in air	12.3	1000	0.012	$1.2 \cdot 10^{-5}$
Tufts cMUT1 in CO <sub>2</sub>	9.66	805	0.012	$1.4 \cdot 10^{-5}$

**Table 6 Transducer parameters combining LDV and input impedance model**

### 3.2.4 Speed of Sound

Speed of sound is used to calculate the time of flight, since the distance  $L$  is fixed on ultrasonic anemometer, the predicted time of flight is:

$$t = L / c \quad (3-3)$$

where  $c$  is the speed of sound. During the testing, the speed of sound in air and 6 mbar CO<sub>2</sub> was used depending on the pressure the transducers are in. According to Laplace's adiabatic assumption for an ideal gas, speed of sound can be calculated as [41]:

$$c = (\gamma P / \rho)^{1/2} \quad (3-4)$$

where  $p$  is the ambient pressure and  $\rho$  is the air density. In dry air, the metric speed of sound is approximately 331.5 m/s at 0 Celsius degrees. The metric speed of sound of CO<sub>2</sub> can be calculated if we extend Laplace's equation above [7]:

$$c_{CO_2} = \gamma R T_k M \quad (3-5)$$

where  $\gamma$  is the adiabatic constant for CO<sub>2</sub>, R is the universal gas constant, T<sub>k</sub> is the absolute temperature in Kelvin and M is the molecular mass of CO<sub>2</sub> in kg/mol.

Further analysis with variation in temperature, pressure, humidity and CO<sub>2</sub> concentration was achieved if we remove ideal gas assumptions [42]. The speed of sound squared as a function of pressure and temperature for a real gas becomes:

$$c^2 = \gamma \frac{RT}{M} \left(1 + \frac{2pB}{RT}\right) \quad (3-6)$$

where B represents second virial coefficient of state. The value of B can be found by:

$$B(T) = 33.97 - \frac{55306}{T} 10^{72000/T^2} \text{ cm}^3 \text{ mol}^{-1} \quad (3-7)$$

For 6 mbar CO<sub>2</sub>, the molar mass M is 44.00995 · 10<sup>-3</sup> kg/mol, gas constant R is 8.314 J/(K · mol), gas constant is 1.4029 J/(K · mol) and p is 600 Pa [42]. the speed of sound value is calculated to be 269.05 m/s for 0°C which is within 0.004% of difference from the calculation for an ideal gas for dry air 269.06 m/s. At 20°C the speed of sound is 278.7 m/s. Humidity has an effect to the value of gas constant, which are demonstrated in the figure below.

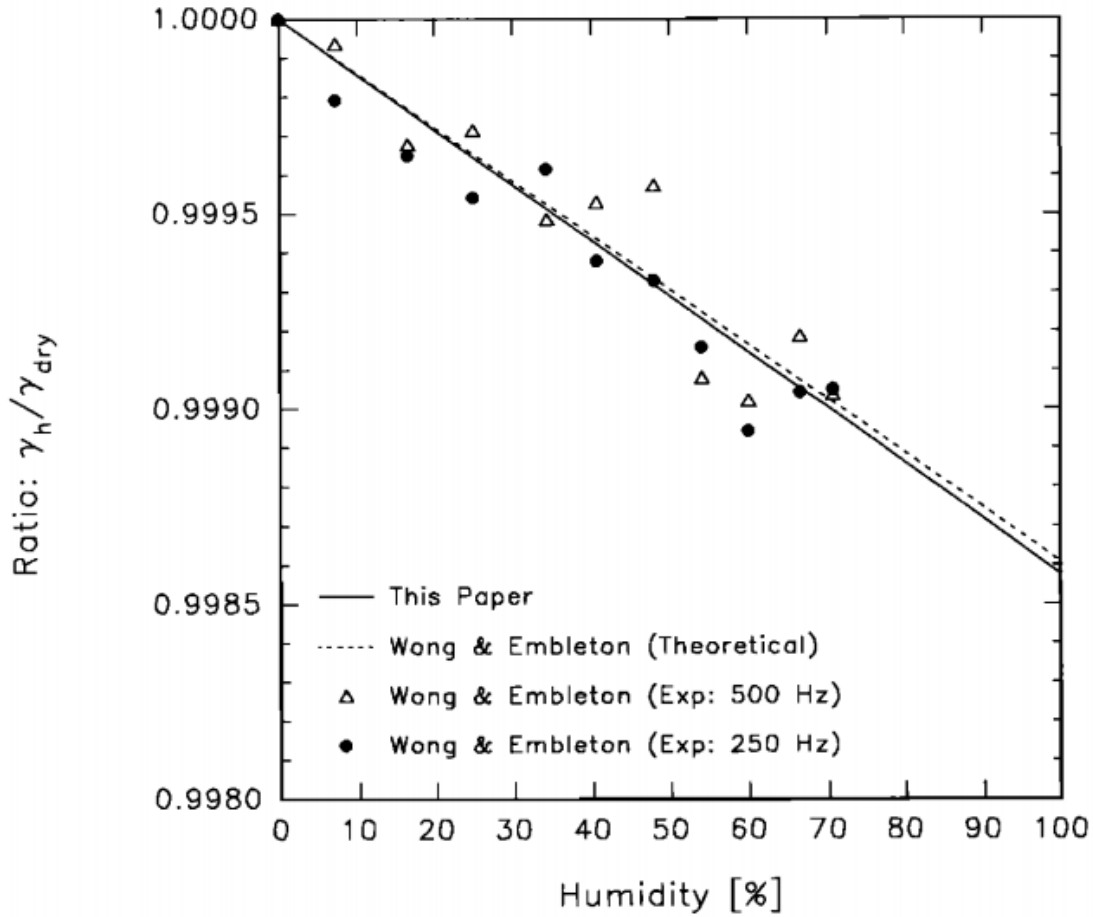


**Figure 19 Gas constant variation with humidity [37]**

The speed of sound in dry CO<sub>2</sub> is 278.7 m/s, assuming dry CO<sub>2</sub> and 20 degrees Celsius and the speed of sound in dry air is 343 m/s at 20 degrees Celsius, assuming dry air. These are the values we used in the time of flight calculation. The humidity might play an important role in the testing process, since the testing chamber will not be absolutely dry. After speed of sound is calculated, the predicted time of flight can be plotted in the time domain signal plot to see if it matched the beginning of the received signal. A more accurate time of flight analysis can be calculated using cross correlation.

### 3.3 Experiment setup

#### 3.3.1 Chamber and pressure

Mars has an air pressure of 6.36 mbar at mean radius with 96% of Carbon Dioxide. To receive detectable signals on Mars, detectable signal at 6 mbar CO<sub>2</sub> at 1.8m are needed. 1.8m was selected so that the ultrasonic transducers were not critically perturbed by the shape of the lander [43]. The testing was done in atmospheric air pressure and 6 mbar CO<sub>2</sub>.

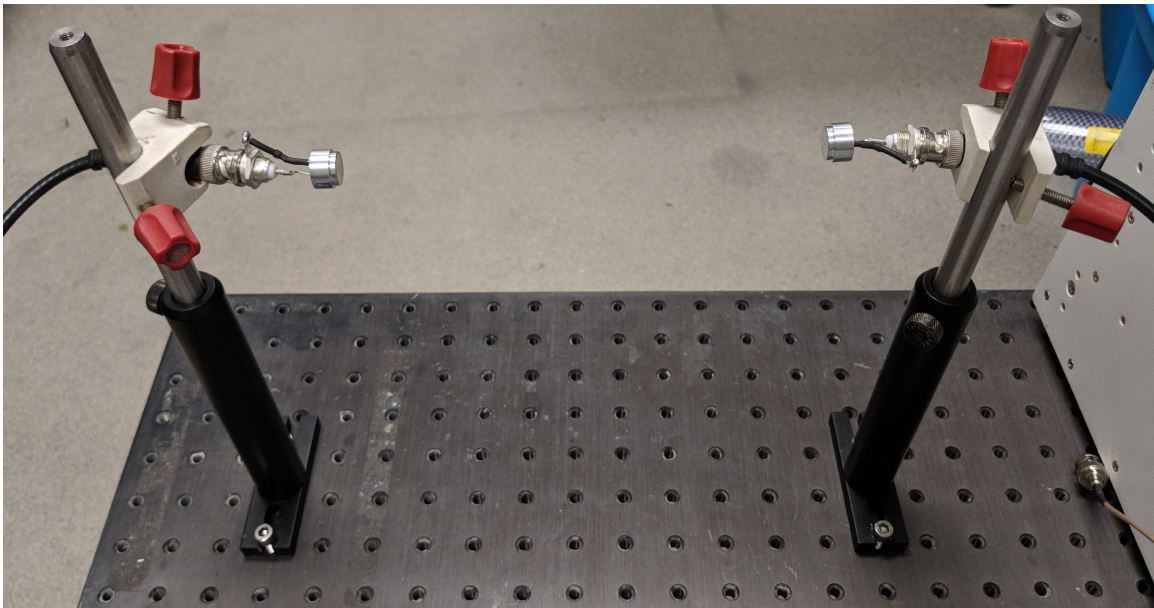


**Figure 20 Testing setup for transducers in air**

A Tufts test chamber was used for creating low-pressure CO<sub>2</sub> environment for simulation of transmission. The chamber has an inner diameter of 11.5 cm. It is connected to a vacuum pump and a CO<sub>2</sub> gas tank through a series of valves. It has also been modified with two SMA feedthroughs. The vacuum pump creates a minimum pressure of 0.2 mbar in the chamber. By releasing the needle-value between the CO<sub>2</sub> tank and the chamber, a constant flow of CO<sub>2</sub> or air into the chamber can be created by using a thermocouple gauge (Edwards D35108000), therefore,

the chamber remains a constant pressure. Pressure values was also adjusted in between the tests to ensure constant pressure in the chamber during testing.

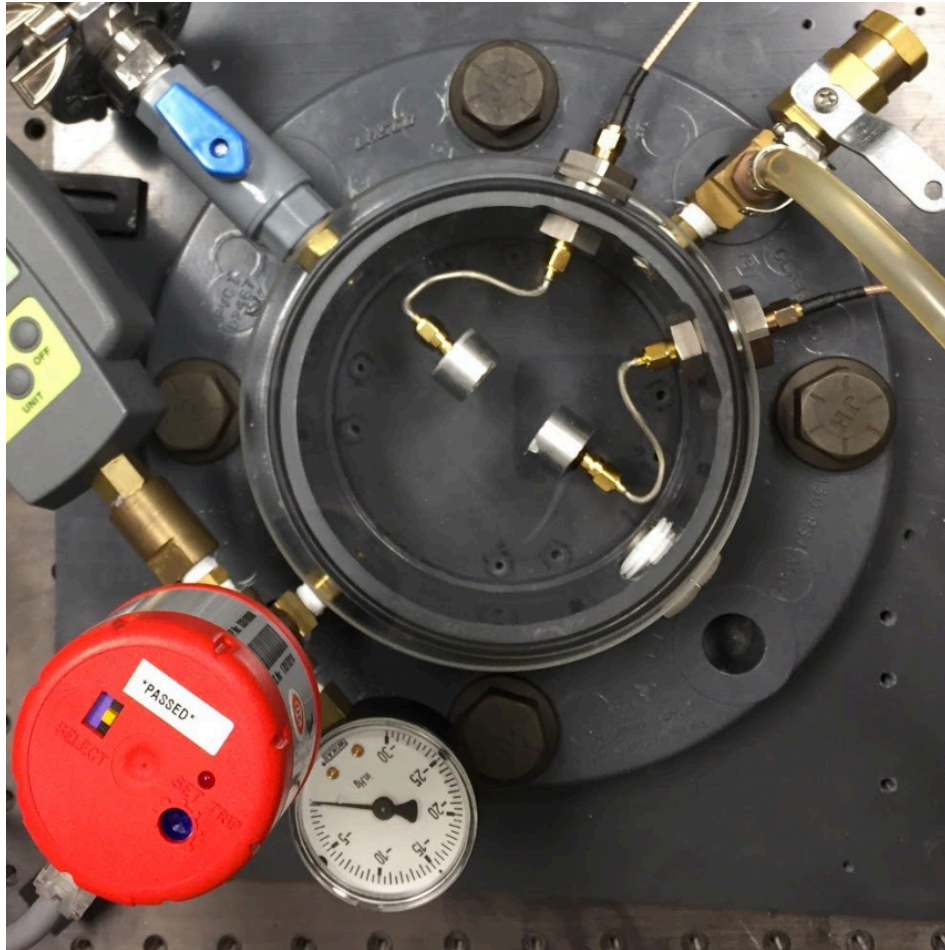


**Figure 21 Testing setup for Kobitone transducers in vacuum chamber**

### **3.3.2 Setup and alignment**

Directivity of the transducers is key to how we want the transducers to be aligned. Using the beam pattern calculated by the LDV data, the beam width was analyzed. Since the actual misalignment is a lot smaller than 10 degrees for PUI and Kobitone, we determined that the loss due to misalignment for these transducers is negligible at 40 kHz, which is the central frequency for both transducers. CAP1 and Tufts cMUT are more directional so they are aligned with extreme care. For a cMUT transducer, the -3dB beam width at 245kHz is  $\pm 5.5^\circ$ .

These transducers are mounted with optical mounts in air and held with SMA cables in the chamber. It was also confirmed before each measurement that the transducers are at the same height and are facing directly to each other. To make sure that the transducers provide the maximum signal amplitude, multiple iteration of data measurement was used to determine the best alignment.

### **3.4 Measurement**

#### **3.4.1 Tiva UT and Configuration**

A Digital Signal Processing control device called Tiva UT was used for the communication between the computer and the transducers. The module was designed and created by VN instrument. It is a network device so the device and the computer are set to be in the same subnet set up by a router. It takes in up to 15W of power and 12 V of voltage and it can supply up to 300 VDC bias. The device works with either contact, immersion or air coupled transducers from 20 kHz up to about 8MHz.

The device can be used in two running modes: transmission mode and reflection mode. In transmission mode, two transducers, which are connected to two channels separately, are set up to be facing each other: one transducer transmits signal and the other transducer receives signal. In the receiving mode, only one transducer is used on one side and reflection surface is on the other side. For our experiments, we are only using the transmission mode, which always involves using two transducers.

This MATLAB-controlled device configures a digital signal based on the percentage assigned, converts them to voltage and then apply the voltage to the transducers. Transducer 1 are connected to channel 1 and transducer 2 are connected to channel 2. The transmitters generate

pressure signals and the receivers converts the pressure signal to voltage, and then the voltage is converted to the digital number in the device's memory, which is then passed down to the computer.

MATLAB controls the configuration settings applied to the transmitter including the time settings, the voltage applied to the transducers, the frequency range of the chirp signal and the windows applied. Receiver amplifier gain in low, medium, high levels can be configured as well.

### **3.4.2 Time domain measurement**

Using MATLAB and TivaUT, various settings are applied to the transducers for transmission. For a transmit-receive experiment, input and output signals for both transducers are plotted in percentages of Digital Number in time domain. The input has a value from 0 to  $2^{14}$  in digital number and the output has a value from 0 to  $2^{12}$  in digital number. Time domain data were plotted as in Figure 22, the received data at channel 1/ transducer 1 transmitted from transducer 2 are plotted in subplot 4 and the received data at channel 2/ transducer 2 transmitted from transducer 1 are plotted in subplot 2.



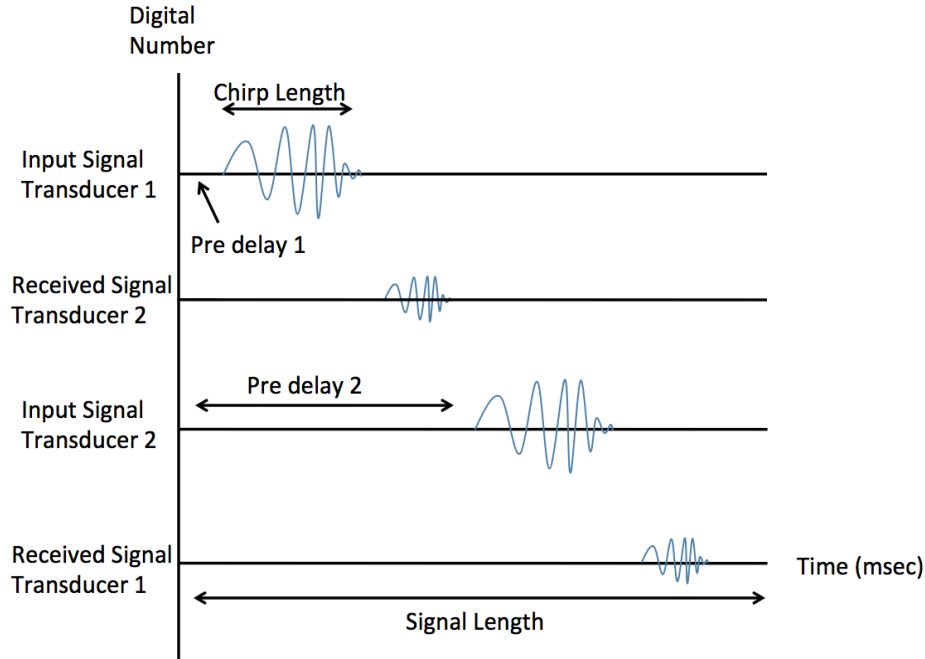


**Figure 22 An example of a time domain plot**

A couple of standards are applied to figure out the optimal time configuration. First, the received signal should not be saturated. For a received signal, saturation represents that the signal is above the value of maximum digital number allowed, which is  $2^{11} \text{ DN}_{\text{peak}}$ . Therefore, a saturated receive signal will be useless. To make sure the received result is useful, a maximum voltage of 40 V<sub>pp</sub> and receiver gain (low, medium, high) are carefully selected. Optimal voltages and gain was able to provide results that are not saturated but high enough for cross spectral analysis.

Second, the pre-delay of both transducers should be long enough to avoid the damping of saturation in the beginning as stated in previous section but not too long to sacrifice updating rate. Most transducers can be seen as second order systems. The damping ratio of the transducers is used to calculate the ring down time of the transducer from saturation. The decay of a saturated signal can be expressed as  $e^{-\zeta\omega t}$ . We want to only receive signal on the transducer after the transducer has stopped ringing from second order system response (amplitude is 1% of the saturated amplitude), so we can solve for t using:

$$e^{-\zeta\omega t} = 0.01 \quad (3-8)$$

For given transducer, the  $t$  calculated can be used for calculating pre-delay, which is the time before the signal has been sent to avoid the overlap between actual signal and the saturation-ring down in the beginning of voltage trying to drive the transducers.

	DC bias (V)	AC Voltage (V <sub>pp</sub> )	Central Frequency (kHz)	Bandwidth (kHz)	Chirp Length (ms)	Signal Length (ms)	Pre-Delay 1 (ms)	Pre-Delay 2 (ms)
Kobitone in air	0	10	39.5	1.5	0.2	8	2	5
Kobitone in 6 mbar CO <sub>2</sub>	0	40	39.5	1.5	0.2	14	2	7
PUI in air	0	40	41	1.5	0.2	8	2	5
PUI in 6 mbar CO <sub>2</sub>	0	40	41	1.5	0.2	8	2	5
cMUT in air	20	20	272	50	0.2	8	2	5
cMUT in 6 mbar CO <sub>2</sub>	20	20	159	10	0.2	8	2	5
CAP 1 in air	220	20	65/50	5	0.2	8	2	5

**Table 7 Time settings for time domain testing for transducers**

Table 7 provided some of the parameters used in the time domain plots. Center frequencies and bandwidth are determined using LDV and input impedance. For easier operation of the received data, chirp length is approximate half of the expected time delay. The signal length represents how long we want to take data for. This is the time it takes for the signals to be fully received in the time domain plot.

At  $T=0$ , a sharp transient occurs in the signal since the Digital Number jumps from 0 to 4096 DN, which is equivalent to 0 Volts out. To avoid this effect on the signal, a 0.4 Tukey window was applied to the chirp to reduce noise and sudden increase of amplitude at  $t=0$ . A Tukey window is a rectangular window with the first and last portion equal to a part of a cosine function. A real

number between 0 and 1 is defined in MATLAB to represent the cosine portion. The window is definition by [44]:

$$x(n) = \begin{cases} 1.0 & 0 \leq |n| \leq \alpha \frac{N}{2} \\ 0.5 \left[ 1.0 + \cos \left[ \pi \frac{n - \alpha \frac{N}{2}}{2(1 - \alpha) \frac{N}{2}} \right] \right] & \alpha \frac{N}{2} \leq |n| \leq \frac{N}{2} \end{cases} \quad (3-9)$$

Tukey window can be plotted as the figure below:

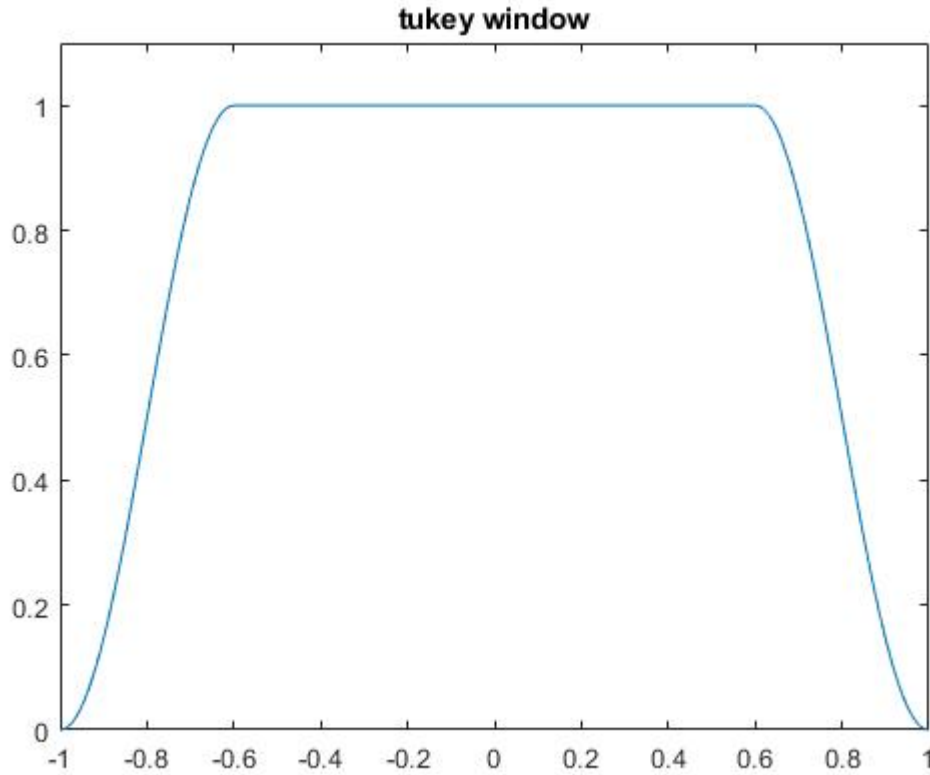


**Figure 23 40% percent Tukey window used in the experiment**

### 3.5 Analytic method

#### 3.5.1 Power Spectral Density (PSD) and Cross Power Spectral Density (CPSD)

MATLAB functions including Fast Fourier Transform (FFT) and Power Spectral Density (PSD) were used to analyze the frequency components of the signal input and the signal received.

The Power spectrum is defined by:

$$P_k = \frac{2}{\Delta f} \left( (X_k \cdot \bar{X}_k) \frac{1}{N^2} \right) = \frac{2(X_k \cdot \bar{X}_k)}{F_s N} \quad (3-10)$$

where  $X_k$  is the Discrete Fourier Transform,  $\bar{X}_k$  is the conjugate of  $X_k$  and  $F_s$  is the sampling frequency. Coherence of the input and the output data is analyzed using:

$$C_{xy} = \frac{P_{xy} \bar{P}_{xy}}{P_{xx} P_{yy}} \quad (3-11)$$

where  $P_{xy}$  is the cross spectrum:

$$P_{xy} = 2Y_k X_k \frac{1}{F_s N} \quad (3-12)$$

Frequency response of the transfer function between the input and the output was plotted as well:

$$H = \frac{P_{xy}}{P_{xx}} \quad (3-13)$$

#### 3.5.2 Cross correlation and time delay calculation

Cross correlation measures the similarity of two functions in their correlation in terms of displacement. The signal received is compared with the original signal with a transfer function model being applied. Using cross correlation function in MATLAB, an accurate time delay was

calculated between the original signal and the received signal and the time delay. Cross correlation of two continuous real functions is defined by following equation:

$$\phi_{xy}(t) = \int_{-\infty}^{\infty} f(\tau - t)g(\tau)d\tau \quad (3-14)$$

where  $\tau$  represents the lag. The convolution of  $f$  and  $g$  is defined as:

$$f(t) * g(t) = \int_{-\infty}^{\infty} f(t - \tau)g(\tau)d\tau \quad (3-15)$$

thus, the cross correlation is related to the convolution by:

$$\phi_{xy}(t) = f(-t) * g(t) \quad (3-16)$$

The time delay is calculated by the argument of the maxima of the cross correlation, where the two functions are best aligned:

$$\tau_{delay} = \arg \max_t (\phi_{xy}(t)) \quad (3-17)$$

In the experiment, the MATLAB cross correlation function is used to conduct the mathematical operation above. Once the time difference is calculated, it is then compared with the time delay.

## Chapter 4 Modeling of the transmit- receive system

The transmit-receive system is modeled and verified in transfer functions. These transfer functions are applied to the original time domain signal in digital number. The transfer functions include  $H_1$  (drive amplifier),  $H_2$  (transmitter transducer),  $H_3$  (air or  $\text{CO}_2$  absorption plus time delay),  $H_4$  (receiver transducer),  $H_5$  (receive amplifier). After each transfer function being applied, a predicted signal can be generated to compare with the measured. If the model proposed provides similar results to the measurement, then we can use the model to predict received data for various pressure and setting combinations for the transducers tested.

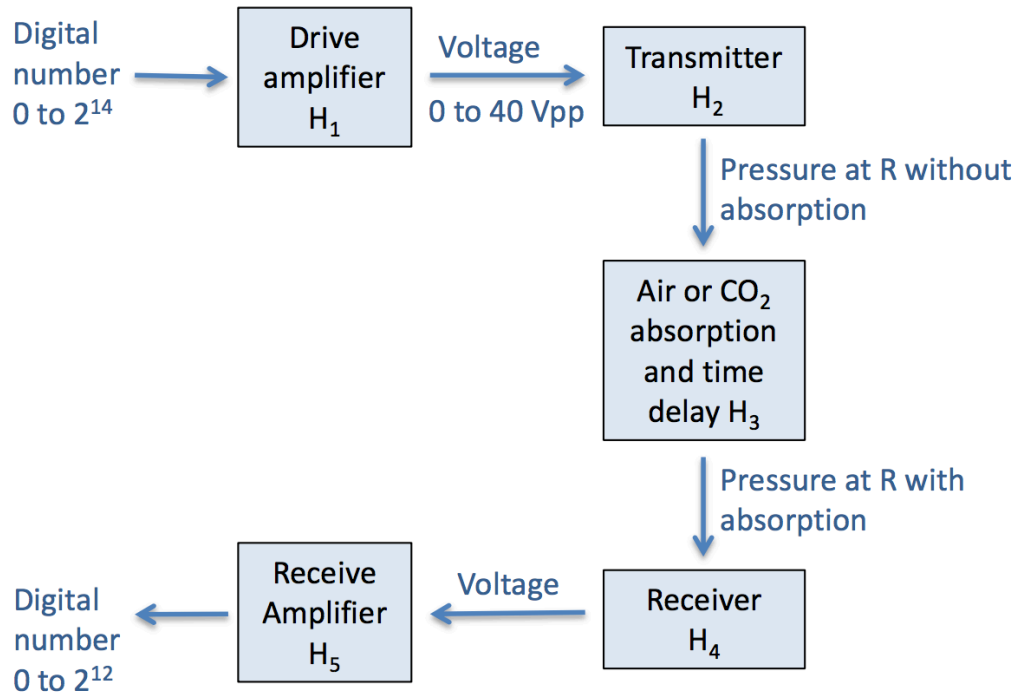


Figure 24 Block diagram of transfer functions in the transmit receive system

The system transfer function has an input of digital number and an output of digital number:

$$H_{sys}(s) = \frac{\text{digital number received (DN)}}{\text{digital number sent (DN)}} \quad (4-1)$$

## 4.1 Key assumptions

In the modeling section, several assumptions were made for simplifying the modeling process. First, we have made the assumptions that the piezoelectric transducers are distributed sources. For PUI transducer, the geometry, the vent holes and the material layers are unknown. With the help of LDV and this assumption, we can predict the source strength for the transducers, therefore predicting the pressure variation with distance.

The second assumption is seeing the mechanical model of piezoelectric transducer as a mass string damper system and the electrical model as a resistance, capacitance, and inductance model. The detail of the assumption can be found in the H<sub>3</sub> section below.

We have also checked that if the far field approximation applies in the Tufts chamber we use. There are two criteria for the far field approximation. First, the distance should be at least five times larger than the diameter of the transducer:

$$r \gg d \quad (4-2)$$

In the chamber, the transducers we have tested has a minimum distance of 1.8 cm, whereas the separation should ideally be more than 7.5 cm based on this criterion, which is five times of the transducer diameter we have tested. The second criterion is that the distance of the transducers should be bigger than the Rayleigh length:

$$r > S / \lambda \quad (4-3)$$

The Rayleigh length is calculated to be 2.4 cm. Neither of the criteria can be well satisfied, therefore, the Farfield approximation is questionable in the small chamber, a larger chamber may be needed to verify our results.

## 4.2 Modeling

### 4.2.1 Drive amplifier

The first transfer function represents the frequency response of the drive amplifier on the TivaUT model; the input is a digital number ranging from 0 to  $2^{14}$ :

$$H_1(s) = \frac{\text{voltage applied to the transducer (V)}}{\text{digital number sent (DN)}} \quad (4-4)$$

We can adjust this input on a percentage scale in the MATLAB code. A value of 100 percent represents  $2^{13}$  peak-to-peak in Digital Number and a 0 percent correspond to a Digital Number of 0. The drive amplifier converts the input to a voltage output, with a maximum voltage about 40 V<sub>pp</sub>. To model the transfer function, chirp signals from the drive amplifier were sent directly to the oscilloscope.

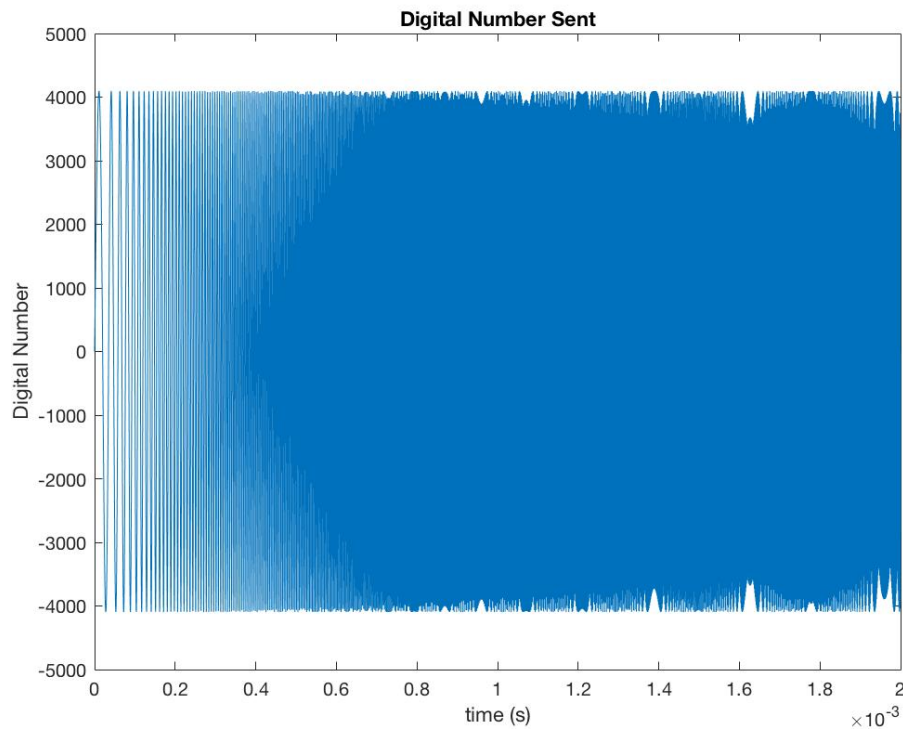


**Figure 25 Time domain chirp signal for Digital Number Sent (input)  
using 50% voltage and a bandwidth of 20-1020 kHz**



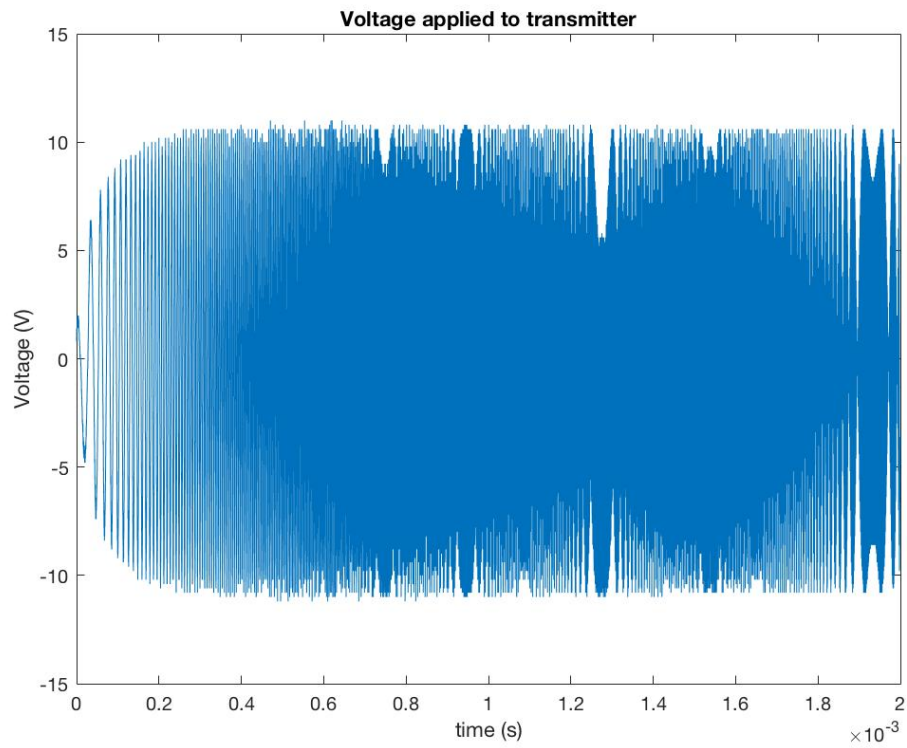


**Figure 26 Received chirp signal on oscilloscope (output)**

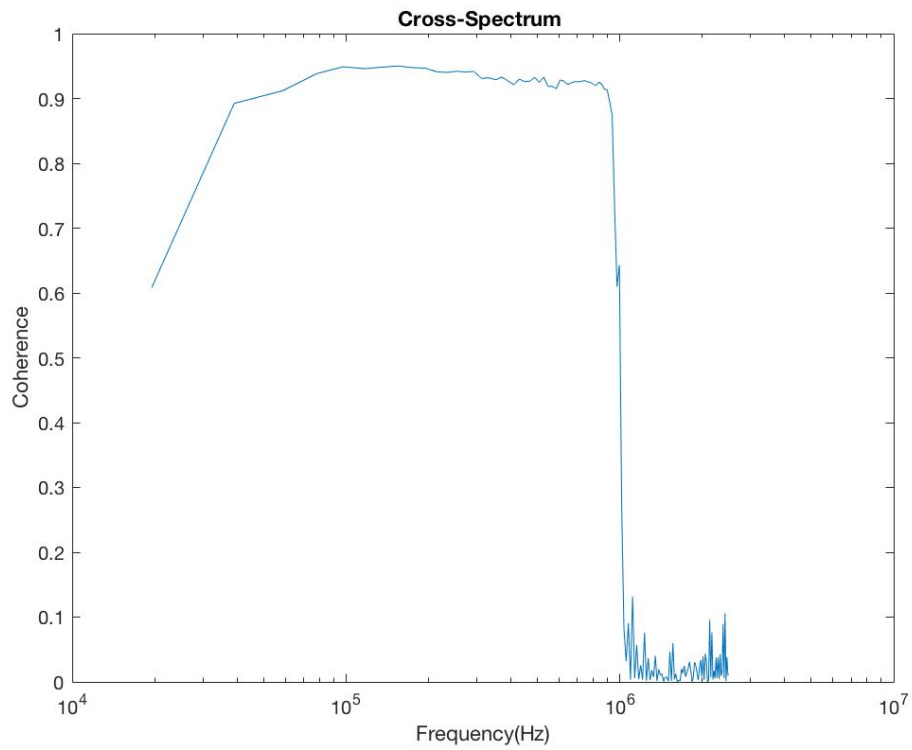


**Figure 27 Coherence plot between the signal sent and received**

The input and output are then compared using cross power spectral density and coherence was calculated. For the bandwidth that are being tested 20-1020 kHz, the coherence remains a value of 0.9 and above; for frequencies that are below 20 kHz and above 1020 kHz, the coherence drops drastically since there were no such frequency components. Therefore, frequency response was calculated in this frequency range for the power amplifier. To model the power amplifier transfer function, a band pass model was created using values from the bode plot and a transfer function is derived:

$$H(s) = \frac{H_0 \frac{\omega_0}{Q} s}{s^2 + \frac{\omega_0}{Q} s + \omega_0^2} \quad (4-5)$$

where  $\omega_0$  is the center angular frequency and Q can be calculated using:

$$Q = \frac{F_0}{F_H - F_L} \quad (4-6)$$

$F_L$  and  $F_H$  are the frequencies correspond to the lower -3dB and higher -3dB frequency. System gain is represented as:

$$H_0 = H / Q \quad (4-7)$$

Using the system Gain and center frequency from the data we plotted modeled transfer functions.

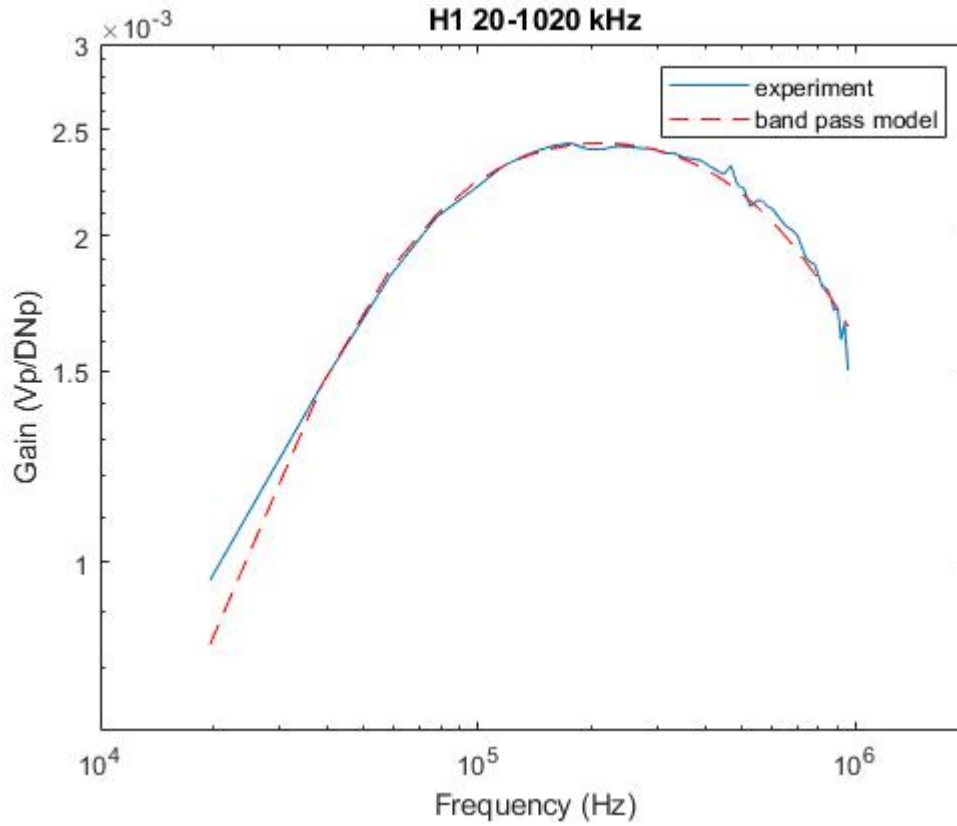


**Figure 28 Gain plot model vs. experiment**

The transmit amplifier was modeled as a band pass:

$$H_1(s) = \frac{12834s}{s^2 + 5276900s + 1.66 \times 10^{12}} \quad (4-8)$$

which is plotted as the red line in Figure 28. The gain has pretty good agreement across frequencies.

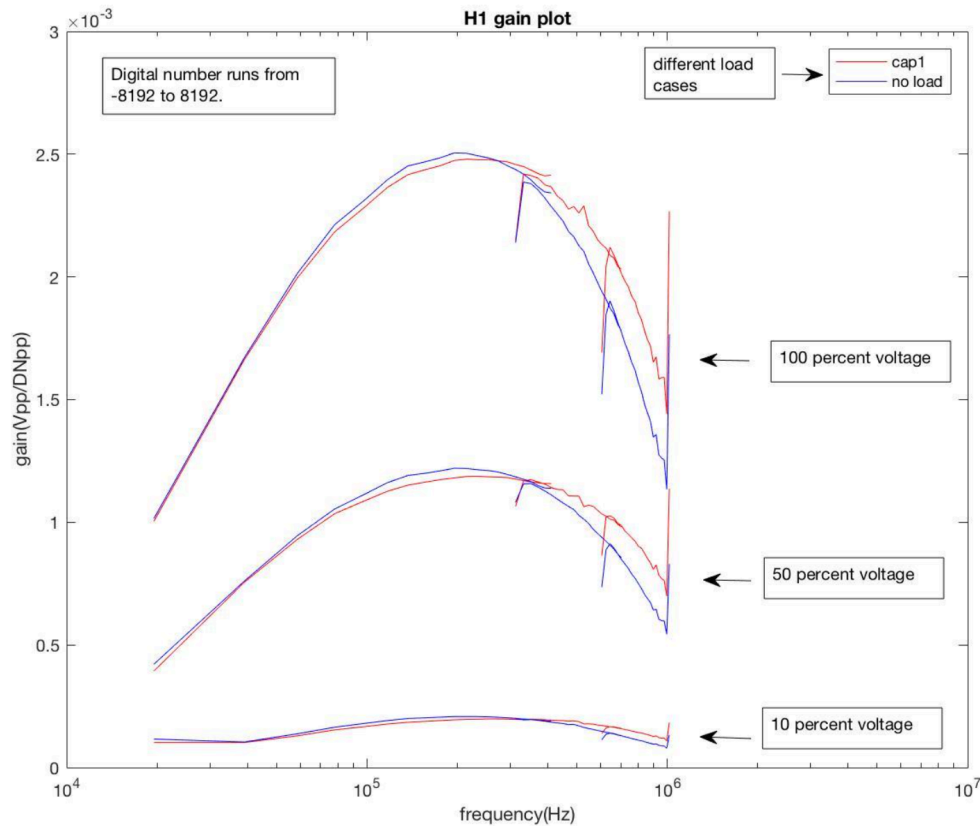


**Figure 29 Gain plot for two load cases at three different percentages**

Figure 29 shows the gain plot for six different cases including 3 percentage settings (10%, 50% and 100%) and 2 load cases (no load and CAP1 load) for power amplifier frequency response. For each load and percentage cases, three measurements were done covering 20-420 kHz, 320-720 kHz, 620- 1020 kHz. We can see the overlap in gain plot since the band passes are overlapped. The spikes represent the gain plot calculated outside of the 20-420 kHz, 320-720 kHz, 620-1020 kHz range for each measurement, which should not be considered. There are three things we can conclude from the graph: first, the power amplifier transfer function acts as a band pass filter to the signal. Second, there is no significant change in gain when we add transducer as a load except for slight shift in central frequency. Three, the gain plot values are proportional to the percentage setting applied in the code.

## 4.2.2 Transmitter transfer function

The second model in the system is the transmit transducer transfer function: we can model the transfer function of the transmitter:

$$H_2(s) = \frac{\text{pressure amplitude at R with no absorption (Pa)}}{\text{voltage applied to the transmitter (V)}} \quad (4-9)$$

the input is the voltage applied to the transmitter and the output is the pressure amplitude at distance R with no absorption. Pressure variation is created by the displacement of the diaphragm of the transducer and the magnitude of diaphragm vibration depends on the magnitude and the frequency of the voltage applied. LDV and input impedance are used for characterization of the frequency response. For a given voltage, each transducer has a different frequency response; therefore, it is necessary to build model for the transducers using their parameter.

### 4.2.2.1 Modeling with LDV data

For piezoelectric transducers, pressure force is generated by displacement of the diaphragm after the voltage is applied to the system:

$$F = k_p \cdot V_{ac} \quad (4-10)$$

Where  $k_p$  is the electromechanical coupling factor in N/V. For each piezoelectric transducer types, LDV is measured in two ways: single point LDV across frequency and surface scan LDV at fixed voltage. The results are then combined to calculate the source strength. Source strength can be seen as an integration of velocity across the surface of the transmitting plate:

$$Q = \int v(x, y) dx dy = \int v(r, \theta) r dr d\theta \quad (4-11)$$

Based on the assumption that piezoelectric transducers are distributed sources, the pressure amplitude on axis as a function of distance can be expressed as:

$$P(R) = \frac{1}{2} \rho c Q / \lambda R \quad (4-12)$$

where  $\rho$  represents the density of air or CO<sub>2</sub>,  $c$  represents speed of sound,  $\lambda$  being the wavelength of the sound wave and  $R$  represents the distance from the vibrating plate. The pressure variation with time is [7]:

$$p(R) = \frac{1}{2} j \rho c (Q / \lambda R) e^{j(\omega t - kR)} = \frac{j \rho \omega Q}{4 \pi R} e^{j(\omega t - kR)} \quad (4-13)$$

the pressure can be written as:

$$p(R) = \frac{\rho s}{4 \pi R} H(s) V_{ac} \quad (4-14)$$

where  $V_{ac}$  is the AC peak to peak Voltage.  $H(s)$  is represented as:

$$H(s) = \frac{Q}{V_{ac}} = \frac{\int v(x, y) dx dy}{V_{ac}} \quad (4-15)$$

As mentioned above, displacement at a point of the diaphragm was measured across frequency and a surface LDV scan was also measured for all the transducers tested. To calculate  $H(s)$ , a derivative is first taken at the displacement surface scan to get velocity scan results. Then the velocity is integrated across the surface to calculate the source strength. The surface scan was done with a RMS voltage of 6.847V at a frequency of 41200 Hz, this indicates a peak drive voltage of 9.683 V. An effective surface area of  $3.1 \cdot 10^{-5} \text{ m}^2$  was derived for the PUI transducer by dividing the source strength by the velocity at 6.847 V and 41200 Hz from the single point LDV. For Kubitone transducers, the effective surface area is calculated to be  $6.9 \cdot 10^{-5} \text{ m}^2$  and an  $k_p/m$  value of 126 N/(V·kg) was derived in air.

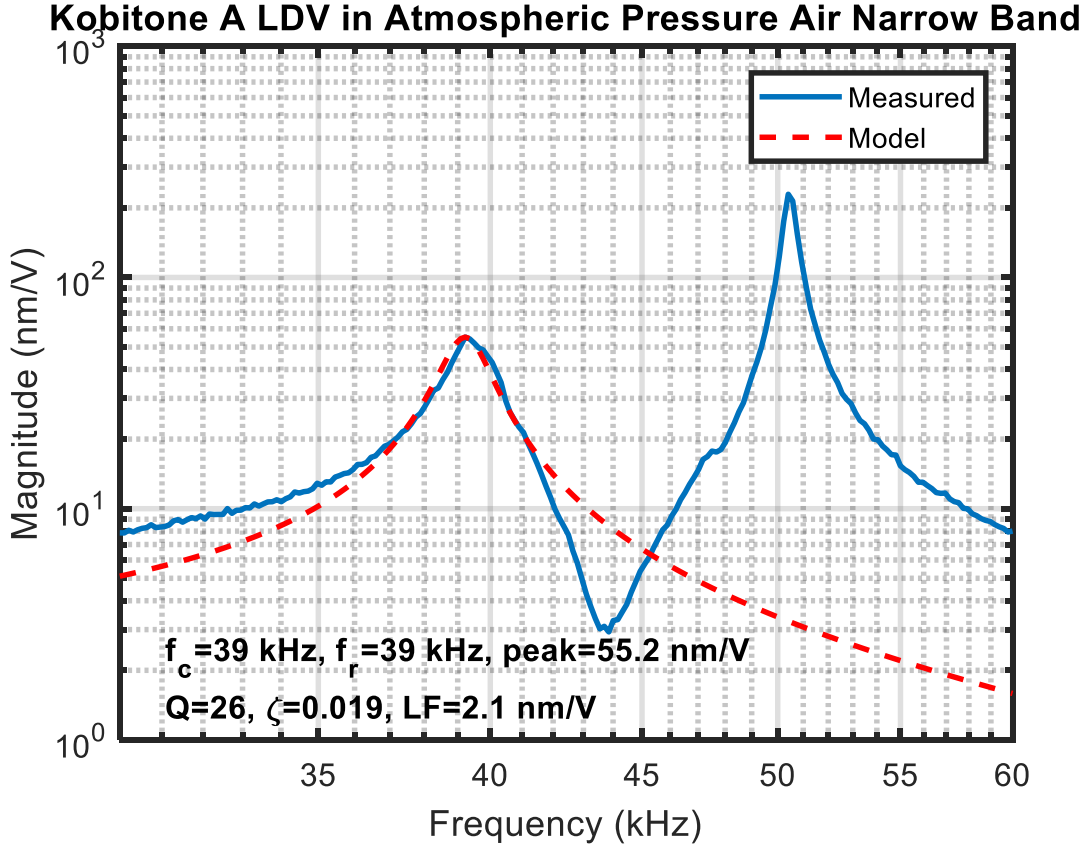


**Figure 30 Single point LDV for Kobitone transducer**

The model fit for the single point LDV data can be plotted, which is 2<sup>nd</sup> order transfer function:

$$H_{mech}^{TX}(s) = \frac{Disp}{V} = \frac{k_p / m}{s^2 + 2\zeta\omega_n s + \omega_n^2} \quad (4-16)$$

System gain can be calculated using the peak value of the data. Using this model, we can calculate source strength as a function of frequency, therefore calculating  $H_2(s)$  and  $p(R)$ . The final transfer function for the second model is then:

$$H_2(s) = \frac{p(R)}{V_{ac}} = \frac{\rho s^2}{4\pi R} H_{mech}^{TX}(s) S_{eff} = \frac{\rho s^2 S_{eff}}{4\pi R} \frac{k_p / m}{s^2 + 2\zeta\omega_n s + \omega_n^2} \quad (4-17)$$

#### 4.2.2.2 Modeling with Input impedance measurement

To further verify the parameters of the piezoelectric transducers and calculating the electromechanical coupling coefficient  $k_p$ , a simple mechanical and electrical model can be constructed for a piezoelectric transducer. The piezoelectric ultrasonic transducer was modeled into a mass spring damper mechanical system.

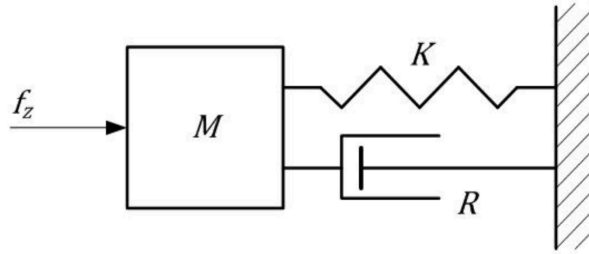


Figure 31 Mechanical model of a piezoelectric transducer [39]

In the mechanical system, the damping coefficient  $R$  represents the force of friction, spring constant  $K$  represents the force of elasticity, and effective mass  $M$  represents the force of inertia. These parameters are all pressure dependent, which indicates that as the pressure drop from 1 atmospheric pressure air to 6 mbar  $\text{CO}_2$ , the values of these effective coefficient will change. The equivalent mechanical impedance can be expressed as:

$$\underline{Z}_{mech} = \frac{F_z}{V} = R + j\omega M + \frac{1}{j\omega K} = R + j(\omega M - \frac{1}{\omega K}) = Z_{mech} e^{j\varphi} \quad (4-18)$$

Vibrating transducer will have the greatest amplitude if the mechanical impedance has the smallest value [45]. At the same time, an electrical system can be modeled for equivalence circuit with the mechanical one. We can think of the system as a series circuit including a resistance, an inductance and a capacitance.

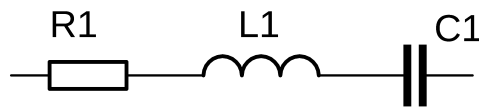


Figure 32 Equivalent electrical circuit



The coupling coefficient, capacitance, resistance of the system, will not change with pressure variation. The equivalent electrical impedance can be derived in a similar fashion:

$$Z_1 = R_1 + j\omega L_1 + \frac{1}{j\omega C_1} \quad (4-19)$$

The impedance can be used for derivation of voltage in the series:

$$V = L_1 \frac{d^2 q}{dt^2} + R_1 \frac{dq}{dt} + \frac{q}{C_1} = L_1 \frac{di}{dt} + R_1 i + \frac{1}{C_1} i d\tau \quad (4-20)$$

where the following relations can be defined:

$$F = k_p \cdot V \quad (4-21)$$

$$i = k_p v \quad (4-22)$$

From the mechanical impedance we can rewrite:

$$V = \frac{M}{k_p^2} \frac{di}{dt} + \frac{R}{k_p^2} i + \frac{1}{k_p^2 K} \int_{-\infty}^t i(\tau) d\tau \quad (4-23)$$

The electromechanical coupling is indicated below as  $C_0$  being the capacitance for the transducer and  $L_1$ ,  $C_1$  and  $R_1$  being the equivalent mechanical parameters. The values of these parameters can be determined below:

$$L_1 = \frac{1}{C_1 \omega_s^2} \quad (4-24)$$

$$R_1 = \sqrt{\frac{(Z_{os})^2}{1 - (C_0 \omega_s Z_{os})^2}} \quad (4-25)$$

$$C_1 = C_0 \left[ \left( \frac{\omega_p}{\omega_s} \right)^2 - 1 \right] \quad (4-26)$$

$$C_0 = \sqrt{\frac{(Z_{os})^2(\omega_p^2 - \omega_s^2) + \sqrt{(2\omega_p^2 Z_{os} Z_{op})^2 + (Z_{os})^4(\omega_p^2 - \omega_s^2)^2}}{2(\omega_p^2 Z_{os} Z_{op})^2}} \quad (4-27)$$

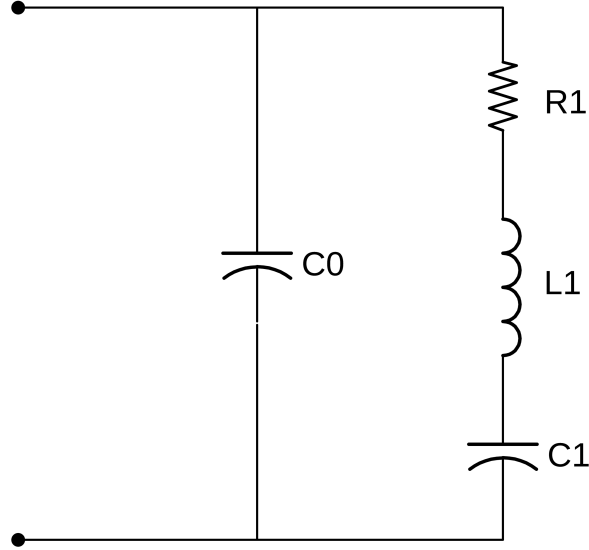


**Figure 33 Equivalent circuit model of an ultrasonic transducer**

The overall impedance model of the circuit can be plotted as:

$$Z_T = \frac{(L_1 C_1 \omega^2 - 1) - j(R_1 C_1 \omega)}{(R_1 C_0 C_1 \omega^2) + j[LC_0 C_1 \omega^3 - \omega(C_0 + C_1)]} \quad (4-28)$$

Resonance and anti-resonance frequency, along with the impedance values were found using input impedance plots. By comparing the input impedance measurement to the model, optimal values for these parameters were found, and electromechanical coupling coefficient was calculated using the model.

$$C_{eq} = (C_0 C_1) / (C_0 + C_1) \quad (4-29)$$

$$C_1 = k_p^2 \cdot K \quad (4-30)$$

$$R_1 = \frac{R}{k_p^2} \quad (4-31)$$

$$L_1 = \frac{M}{k_p^2} \quad (4-32)$$

### 4.2.2.3 Combining LDV and input impedance model

Since we have calculated  $k_p/m$  in air from LDV model and  $k_p^2/m$  from input impedance model, both  $k_p$  and effective mass are calculated as provided in Table 6. Calculation was also done for  $k_p/m$  in 6 mbar CO<sub>2</sub>. These parameters are used in the model for different pressure and transducer scenarios.

### 4.2.3 Absorption

Another factor to consider in the progress of air transmission is the absorption  $H_3$ . This transfer function can be modeled as:

$$H_3(s) = \frac{\text{pressure amplitude at R with absorption (Pa)}}{\text{pressure amplitude at R with no absorption (Pa)}} \quad (4-33)$$

where the input is the pressure at distance R assuming no absorption, and the output is the pressure at distance R with absorption. The third transfer function will be:

$$H_3(s) = e^{-\alpha R} \quad (4-34)$$

6 mbar CO<sub>2</sub> have a larger absorption coefficient than in air, as a result, a carefully derived value for absorption coefficient on Mars is used. According to Williams [8], The absorption coefficient is a combination of viscous absorption coefficient, thermal diffusion absorption coefficient and molecular relaxation absorption coefficient as indicated below:

$$\alpha_v = \frac{2}{3} \frac{\omega^2 \eta}{\rho_0 c^3} = \frac{8}{3} \frac{\pi^2 f^2}{\rho_0 c^3} \eta \quad (4-35)$$

$$\alpha_T = \frac{dQ}{I} = \left( \frac{\gamma - 1}{\gamma} \right) \frac{4\pi^2 f^2 K}{\rho_0 c^3 C_v} \quad (4-36)$$

$$\alpha_m = \frac{2\mu_{\max} f_M f}{f_M^2 + f^2} \quad (4-37)$$

where  $f$  is the frequency of the sound wave,  $\eta$  is the viscosity coefficient in  $\text{N}\cdot\text{s}/\text{m}^2$ ,  $\rho$  represents the air density in Mars atmosphere. The values and units of each parameter are summarized in the table below.

	Value	Unit	Definition
$T_k$	220	K	Temperature in Kelvin
$\eta$	$11.9 \cdot 10^{-6}$	$\text{N}\cdot\text{s}/\text{m}^2$	Viscosity coefficient
$K$	0.01083	$\text{W}/(\text{m}\cdot\text{K})$	Thermal conductivity
$C_v$	568.1	$\text{J}/(\text{kg}\cdot\text{K})$	Heat capacity
$\Upsilon$	1.338	N/A	Ratio of specific heat
$\mu_{\max}$	0.16	N/A	Maximum value of the function plotted against the log of the frequency
$f_M$	129	Hz	The corresponding frequency for $\mu_{\max}$

**Table 8 Parameters used in the calculation for absorption coefficient [8,46]**

A total absorption coefficient can be plotted but summing up the three absorption coefficients:

$$\alpha_{tot} = \alpha_v + \alpha_T + \alpha_m \quad (4-38)$$

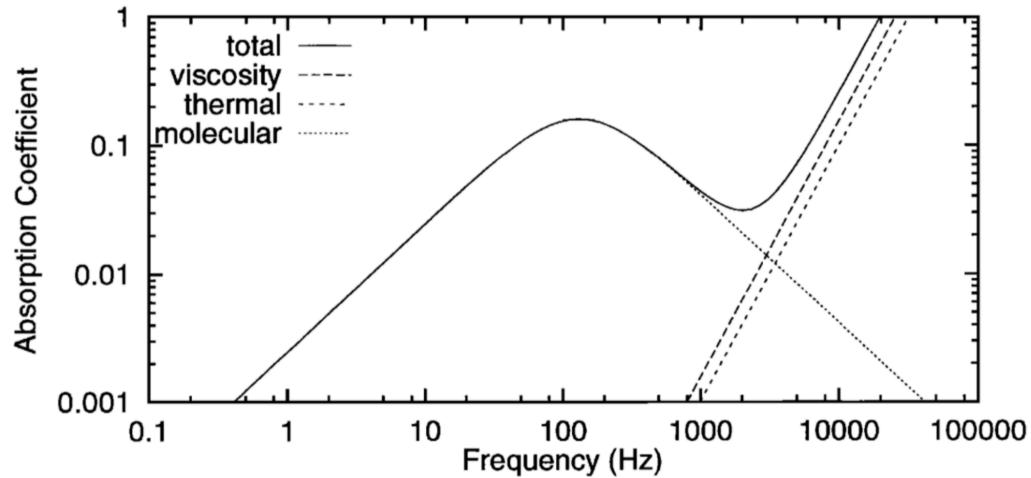


**Figure 34 Absorption coefficient in Np/m as a function of frequency in Martian atmosphere for a 6 mbar CO<sub>2</sub> atmosphere at 220K [8]**

In order to model absorption correctly, the absorption coefficient is found for the frequencies of transducers we are testing. The PUI and Kobitone transducers requires a central frequency of around 40 kHz in both air and 6 mbar CO<sub>2</sub>. The absorption coefficient in atmospheric air, based on Kinsler, is 0.02 Np/m at 40 kHz in dry air. Using Williams's calculation, the absorption coefficient is approximately 4.4 Np/m on Mars at 40 kHz, which is equivalent to 38.2 dB/m at 40 kHz. For testing cMUT transducers in air, an absorption coefficient is found to be 1.2 Np/m at 280 kHz. In 6 mbar CO<sub>2</sub>, a frequency of 150 kHz is

required for cMUT. The absorption coefficient at this frequency in 6 mbar CO<sub>2</sub> is calculated to be 58 Np/m. In our Simulink model, the time delay is also added in H<sub>3</sub>.

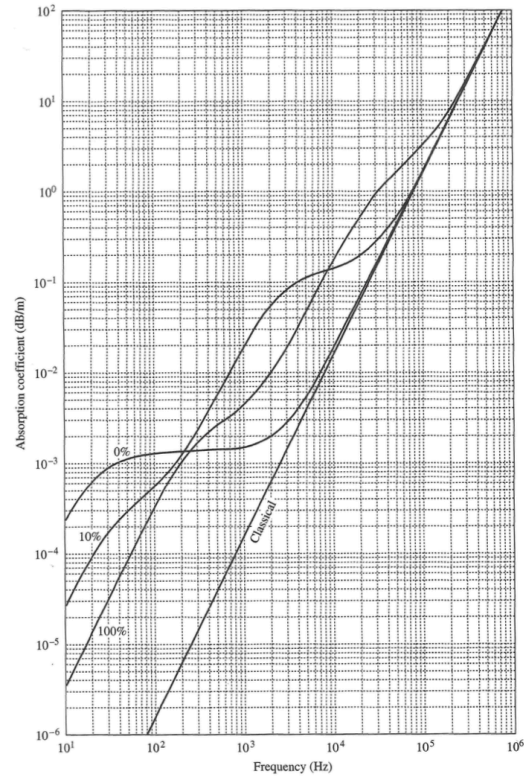


Figure 35 Absorption of sound as a function of frequency in 1 atm air [7]

#### 4.2.4 Receiver transfer function

Since we know the force and displacement coupling, the fourth transfer function can be derived.

$$H_4(s) = \frac{\text{current generated at the receiver (A)}}{\text{pressure amplitude at R with absorption (Pa)}} \quad (4-39)$$

From the previous coupling analysis, we can infer:

$$k_p = \frac{I}{v} = \frac{N}{V} \quad (4-40)$$

The ratio of the current and the pressure equals to:

$$\frac{I}{P} = \frac{I}{F / S_{eff}} = S_{eff} \cdot k_p \cdot j\omega \cdot H_{mech}^{RX} \quad (4-41)$$

where the input of the receive amplifier transfer function is the pressure force and the output is the displacement. The transfer function can be written as:

$$H_{mech}^{RX}(s) = \frac{1/m}{s^2 + 2\zeta\omega_n s + \omega_n^2} \quad (4-42)$$

The receiver mechanical transfer function is different from the transmitter by a factor of  $k_p$ . As a result, the transfer function for the receiver transducer is:

$$H_4(s) = \frac{(S_{eff} \cdot k_p / m)s}{s^2 + 2\zeta\omega_n s + \omega_n^2} \quad (4-43)$$

#### 4.2.5 Receive amplifier

The final step for the transmit and receive system is the receiver amplifier. The input of the transfer function is the current generated by the transducers and the output is the final digital number received by the computer:

$$H_5(s) = \frac{\text{digital number received (DN)}}{\text{current generated at receiver (A)}} \quad (4-44)$$

The final transfer function is tested by sending a small voltage signal to the receive amplifier and receive the signal in digital number on the computer end. The voltage that was sent in had to be small enough so that it does not do any damage to the preamplifier. A better estimate of the receiver amplifier gain can be estimated if we know the receiver amplifier circuit.

Based on the testing, the simplified charge amplifier circuit was modeled to be the circuit below. A voltage is applied to the op amp. The voltage is calculated by integrating the output current of the transducer and then dividing the transducer capacitance:

$$V = \frac{1}{C_0} \int i(t) dt \quad (4-45)$$

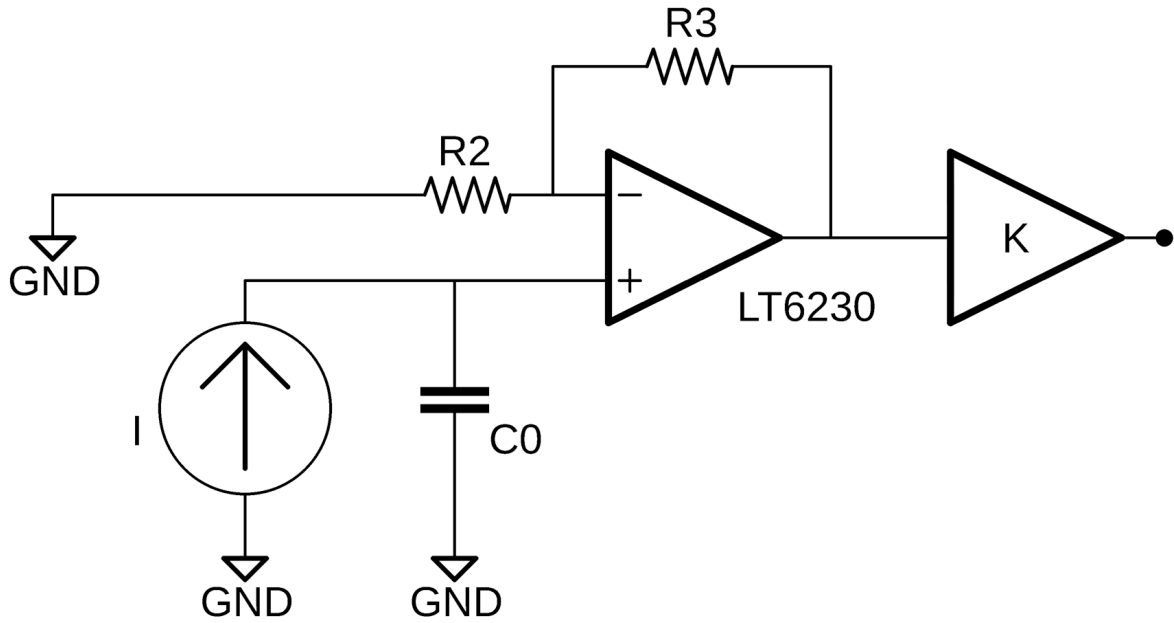


**Figure 36 Preamplifier circuit diagram**

In the diagram,  $R_2$  and  $R_3$  are resistors of same value, which is  $2200 \, \Omega$ . Therefore, the op-amp has a unity gain. The output of this diagram is further amplified by  $K$  conditioned by different gain settings. Since the band pass we have characterized seemed to be wide enough, we can see  $K$  as a flat gain across the frequency of interest.  $K_2$  can be represented by:

$$K = \begin{cases} 7466.7 \frac{DN}{V} & \text{Low Gain} \\ 32667 \frac{DN}{V} & \text{Medium Gain} \\ 140000 \frac{DN}{V} & \text{High Gain} \end{cases} \quad (4-46)$$

The last transfer function can be written as:



$$H_5 = \frac{1}{C_0 s} \cdot \begin{cases} 7466.7 \frac{DN}{V} & \text{Low Gain} \\ 32667 \frac{DN}{V} & \text{Medium Gain} \\ 140000 \frac{DN}{V} & \text{High Gain} \end{cases} \quad (4-47)$$

#### 4.2.6 System transfer function

The system transfer functions for the three pair of transducers can be calculated using the transfer functions derived above. The power amplifier and the receive amplifier transfer function does not change for all the transducer and pressure cases. Each transducer will have different transfer functions based on the parameters derived in LDV and input impedance measurement. The absorption coefficient in air and 6 mbar CO<sub>2</sub> are also different. All the transfer functions were applied to a simulated chirp in SIMULINK, as well as a MATLAB function to predict peak digital number received and to calculate time delay.

## Chapter 5 Results

### 5.1 Time domain plot

By using appropriate time and voltage settings, all of the four transducers we have tested are capable of transmitting linear chirp signal in air. Three transducers were tested in the vacuum chamber in 6 mbar CO<sub>2</sub>. Both PUI and Kobitone were capable of transmitting and receiving ultrasound chirp signals in 6 mbar CO<sub>2</sub> in the chamber.

In the time domain plot indicated below, the signal applied to transducer 1 and transducer 2 are indicated as SigOut1 and SigOut2, respectively. Received signal at transducer 2 from transducer 1 are plotted in ADC1 and received signal at transducer 1 from transducer 2 are plotted in ADC2. A red line was plotted in the time domain plot which is calculated by distance measured between the transducers divided by the speed of sound in the corresponding media.

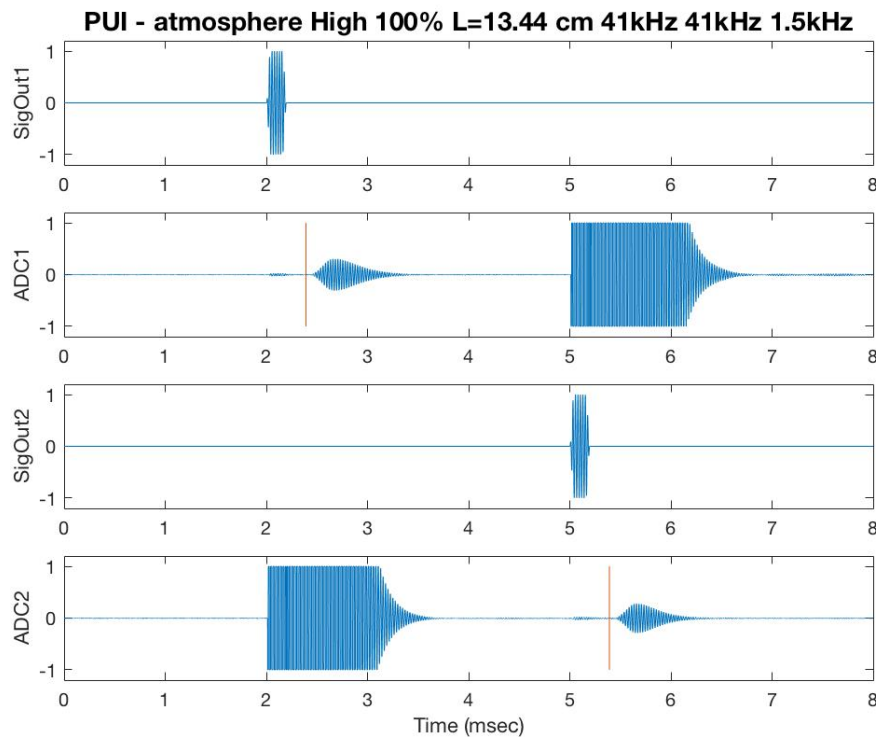
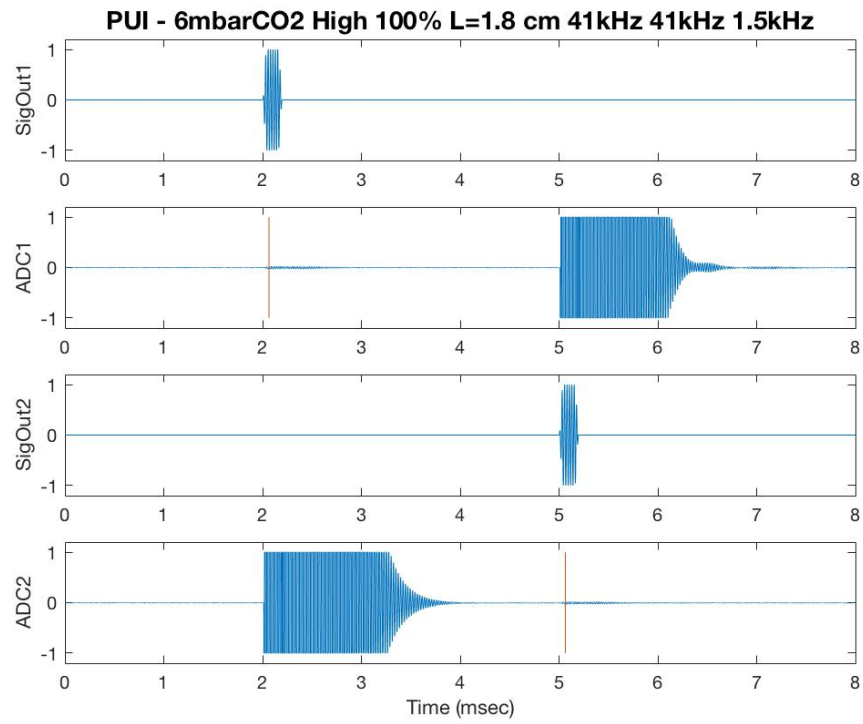
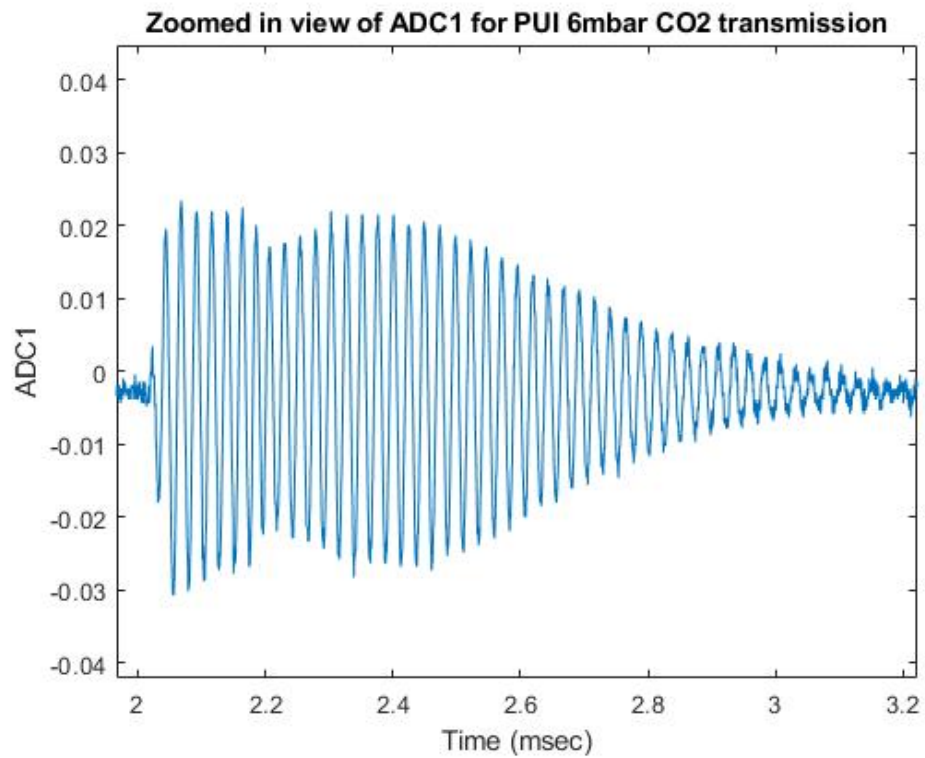


Figure 37 Time domain plot for PUI in atmospheric air

(a)



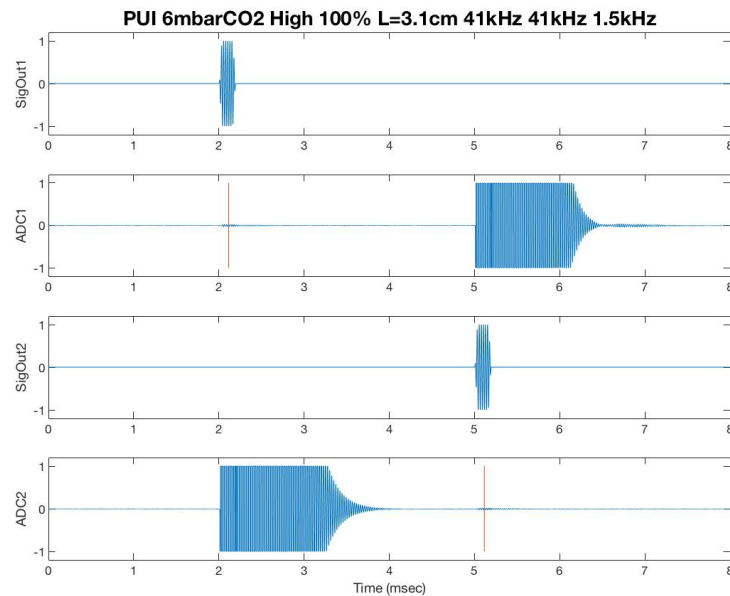
(b)



**Figure 38 Time domain plot for PUI in CO<sub>2</sub> at 1.8 cm  
(a) for both channels (b) zoomed in view for ADC1**

PUI transducer was able to transmit and receive ultrasound chirp signal in both atmospheric air and 6 mbar CO<sub>2</sub>. The signal can be seen in Figure 38. Unlike what we have observed in air, the shape of the received chirp is not symmetrical. To verify if beginning part of the received signal is crosstalk, the distance between the PUI transducers was increased to 3.1 cm and a second chirp signal was sent as in Figure 39. By increasing the distance, the Digital Number received for the acoustic signal was decreased as you can see in Figure 39(b) and the crosstalk remains the same amplitude in Digital Number. It is then verified that the cross talk overlapped with the acoustic signal. Figure 39 implies that in order to separate the crosstalk with the acoustic signal completely, we have to make the distance between the transducers bigger. But since the acoustic strength decreases with distance, a much further distance would result indistinguishable acoustic signal with noise. We have proved that the cross talk will not affect the cross-correlation results of prediction the time delay, provided that the PUI transducers are within 3.1 cm. But if the distance increases to 4.1 cm, the received signal can no longer be identified.

(a)



(b)

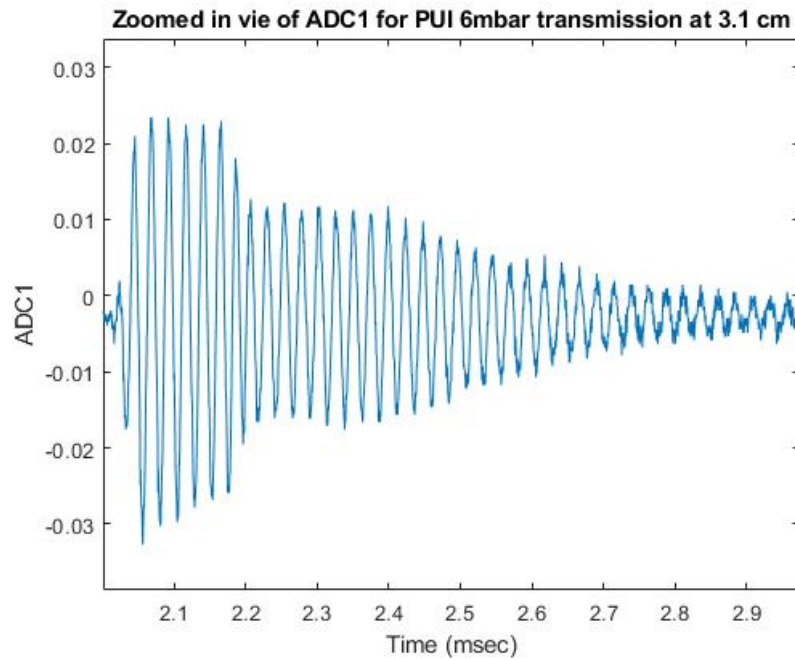


**Figure 39 Time domain plot for PUI in CO<sub>2</sub> at 3.1 cm**  
**(a) for both cannels (b) zoomed in view for ADC1**

Compare to PUI, Kobitone was able to generate Digital Number at the same level only requiring 25% voltage and low gain. In 6 mbar CO<sub>2</sub> chamber, ultrasonic signals were transmitted and received between a pair of Kobitone transducers for 100% AC Voltage and high gain. Comparing to PUI, with more than twice the distance, Kobitone was able to receive approximately

twice as much in Digital Number. Due to the larger distance, the crosstalk has less of an effect for the received chirp in CO<sub>2</sub> comparing to PUI.

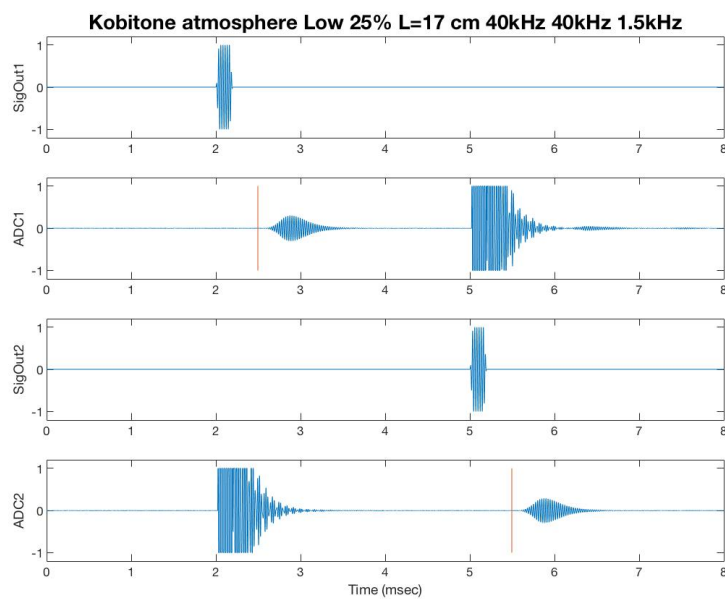


**Figure 40 Time domain plot for Kobitone in atmospheric air**

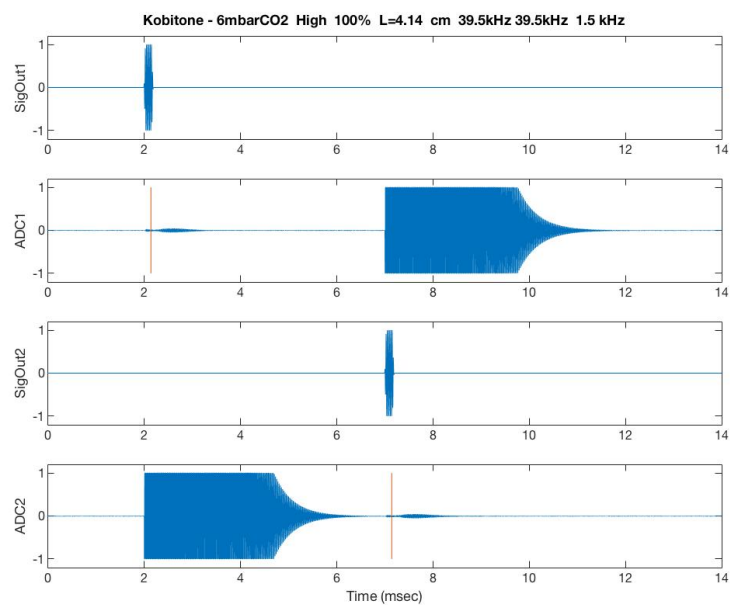
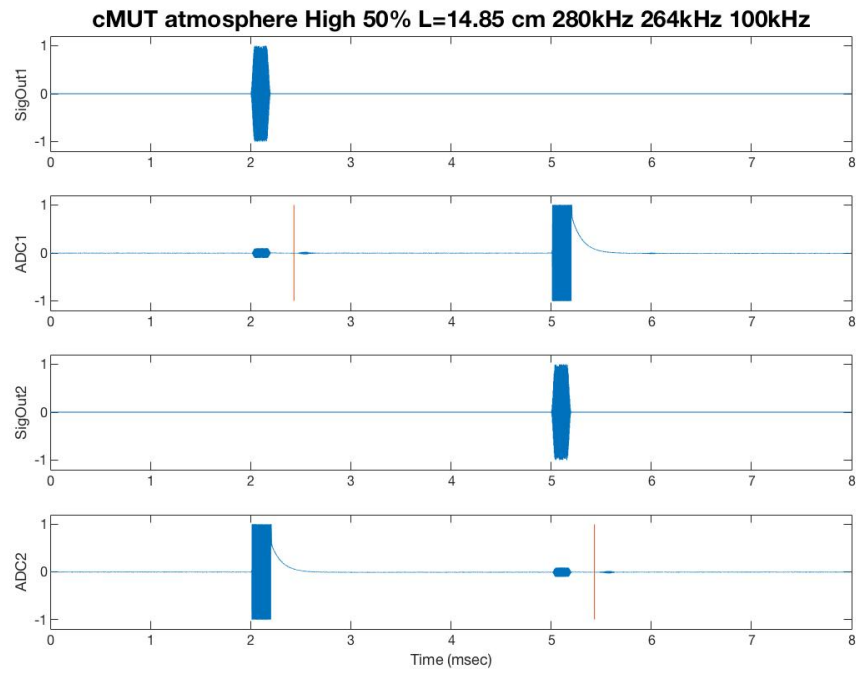


**Figure 41 Time domain plot for Kobitone in 6 mbar CO<sub>2</sub>**

(a)



(b)

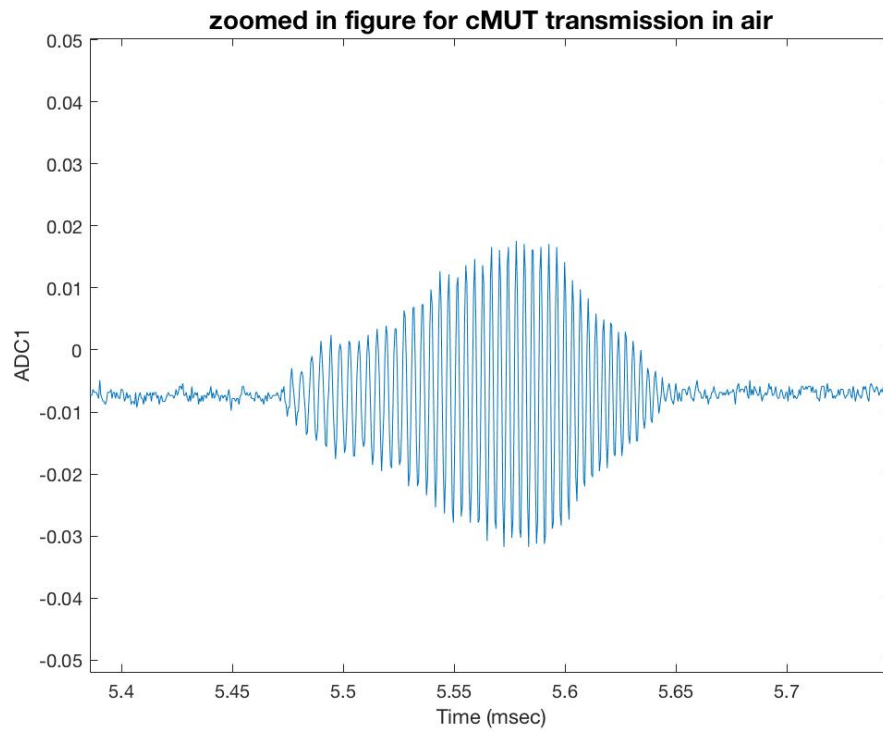


**Figure 42 Time domain plot for Tufts cMUT in atmospheric air  
(a) for both channels (b) zoomed in figure for ADC1**

Tufts cMUT transducers were able to send out signal with wider bandwidth in atmospheric air and signals were received. But no transmission was observed in 6 mbar CO<sub>2</sub>. To verify if there is any data received, a cross correlation was done between the signal sent and received for 6 mbar CO<sub>2</sub>. A time difference of 2.02  $\mu$ s was derived for the time delay, which is smaller than the distance /sound speed calculation, which is 68  $\mu$ s. Therefore, the signal was confirmed not to be observed. Our model has also predicted that the received signal will be below the noise level.

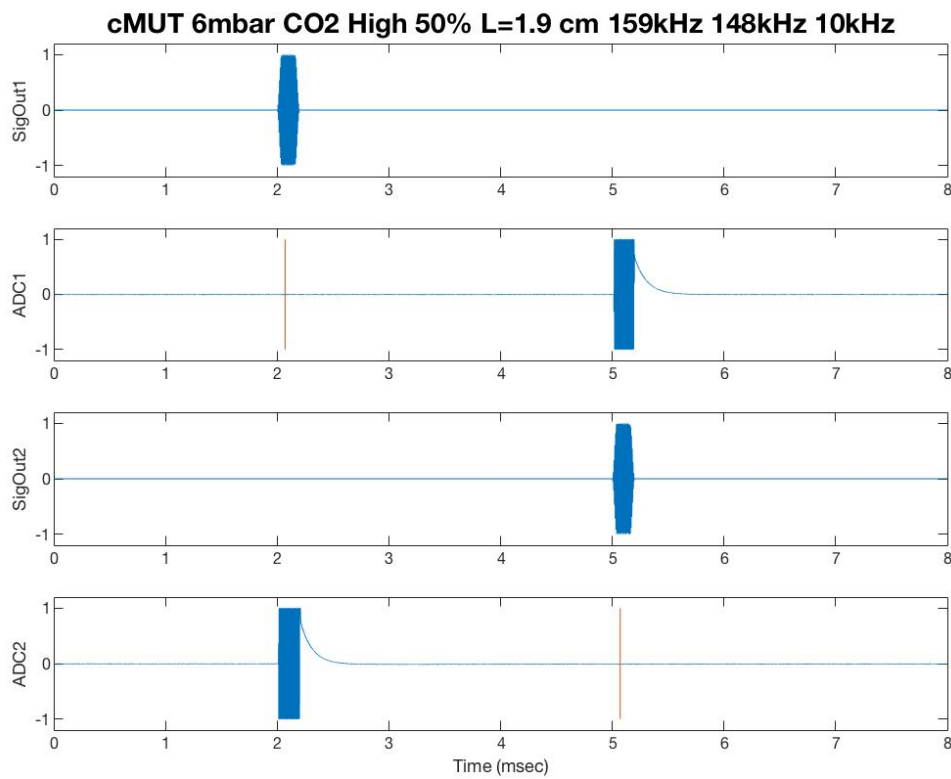


**Figure 43 Time domain plot for Tufts cMUT in 6mbar CO<sub>2</sub>**

CAP 1 transducers were also tested in air for chirp ultrasound signal transmission. It was able to provide high signal using Medium gain and 50% Voltage. The distance between the CAP1



transducers was also set to be 27.4 cm to avoid saturation of the signal. Due to the size of the transducers, it was not tested in Tufts chamber.

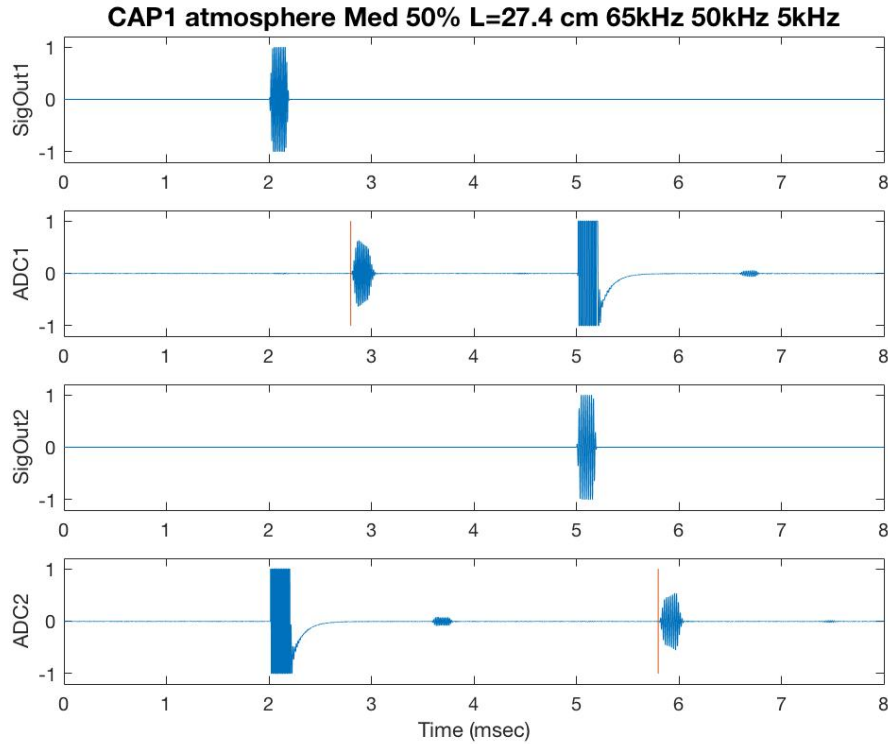


Figure 44 Time domain plot for CAP1 in atmospheric air

## 5.2 Peak amplitude of time domain chirp

SIMULINK was used to predict the amplitude of the chirp signal received for PUI, Kobitone and Tufts cMUT. The prediction is then compared with measured signal provided in the figures above. Using the parameters attained from LDV and electrical input impedance, we have successfully predicted and verified maximum signal strength for PUI transducers. For Kobitone and cMUT, the predictions are far away from the results. Comparing to Kobitone and cMUT transducers, the source strength of PUI are more predictable since it's a circular piston with fixed outside boundary conditions.

	Digital Number Percentage	Digital number peak input (DN)	Gain Settings	Predicted peak received signal (DN)	Actual peak received signal ratio at central frequency	Actual peak received signal (DN)
PUI D and E in air at 13.443 cm	100%	8192	Low	31.9	0.013	27
	100%	8192	Medium	139.5	0.069	141
	100%	8192	High	598.0	0.303	621
PUI in CO <sub>2</sub> at 41 kHz and 1.8cm	100%	8192	High	42.63	0.020	41
Kobitone D and E in air at 17 cm at 39.5 kHz	25%	2048	Low	2.6	0.300	612
Kobitone D and E in CO <sub>2</sub>	100%	8192	High	42.55	0.045	93
Tufts cMUT 31 39 in air at 14.85 cm	50%	4096	Med	596.7	0.020	41

**Table 9 Comparison of signal sent and received in various gain settings**

### **5.3 Time of flight**

The time of flight calculated from the distance is added to the damping time expected by the model, then it is compared with the time delay calculated by the cross correlation. The following table shows the comparison. The prediction of the Kobitone transducers does not agree with measured result.

Based on calculation, the cross talk can be separated with the acoustic signal if the transducers are 6.86 cm away, which based on the model, generates a signal strength of 9 DN<sub>peak</sub>,

which is about twice of the noise level. This means theoretically about half of the chirp can't be distinguished with the chirp.

Transducers	Distance (cm)	T1= L/c (ms)	T2= Cross correlation model prediction (ms)	Predicted T1+T2 (ms)	Cross correlation time delay (ms)
PUI in air	13.443	0.39	0.24	0.63	0.59
PUI in 6 mbar CO <sub>2</sub>	1.8	0.0646	0.2768	0.34	0.284
Kobitone In air	17	0.500	0.234	0.734	0.802
Kobitone in 6 mbar CO <sub>2</sub>	4.29	0.148	1	1.148	0.528
CMUT in air	17	0.500	0.005	0.505	0.517
CAP1 in air	27.4	0.799	N/A	0.799	0.811

**Table 10 Time of flight result for transducers tested**

## Chapter 6      Discussion

Among four of the ultrasonic transducers, all of them have the capacity of transmitting and receiving ultrasonic chirp signals using TivaUT electronics using the Tiva UT; two of them were also capable of transmitting and receiving ultrasonic signals in 6 mbar CO<sub>2</sub> using Tiva UT.

The transfer function model is verified for the transmit and receive system for PUI transducers. The peak digital number received is within 5% difference from the value predicted for PUI transducers in air and in 6 mbar CO<sub>2</sub>. Because of the size of the chamber, LDV measurement was not achieved for these transducers in 6 mbar CO<sub>2</sub>, which might have caused inaccuracies of the prediction for Kobitone and cMUT in 6 mbar CO<sub>2</sub>. Since the diaphragm of the Kobitone transducer have fixed center and the LDV is done in the center, it might be a good idea to perform multiple LDV scan to calculate and verify source strength. At the same time, our transfer function model was only done on the first mode of the Kobitone transducer, which might also have an effect on the prediction. cMUT transducer was capable of transmitting and receiving ultrasonic signals in air, however, the signal in 6 mbar was not observed due to the change source strength due to density change. But a detectable signal should still be expected in 6 mbar CO<sub>2</sub> if we increase the DC bias and AC voltage, as well as changing the electronics gain.

Using the transfer function model, time delay was predicted. The time of flight prediction is within 10% for the measurements in air for all four transducers. The time of flight prediction for PUI tested in 6 mbar CO<sub>2</sub> has a 16.8% percentage difference. A larger chamber can also be built for time of flight measurement in 6mbar CO<sub>2</sub> with increments in distance.

	Peak measured ( $DN_{\text{peak}}$ )	Peak predicted ( $DN_{\text{peak}}$ )	Percentage difference	Time measured (ms)	Time predicted (ms)	Percentage difference
PUI in air	621	598	3.7%	0.59	0.63	6.3%
PUI in 6mbar $CO_2$	41	42.63	3.8%	0.284	0.34	16.4%
Kobitone in air	612	2.6	99.6%	0.802	0.734	8.48%
Kobitone in 6mbar $CO_2$	93	42.55	54.2%	0.528	1.148	54%
cMUT in air	41	596.7	93.1%	0.517	0.505	2.3%
CAP 1 in air	1294	N/A	N/A	0.811	0.799	1.47%

**Table 11 Percentage difference between measurement and prediction**

In the modeling section, we have assumed that the ultrasonic transducers are seen as distributed source. No terms were included to model the diffraction and reflection from the transducer housing. The effective area was used and only a single point LDV scan was used to predict the transfer function of the transducer, it is a simplification. Only one mode of Kobitone transducers were modeled at a single point, it might be possible that the single point does not provide good representation of the source. Surface scan was also done only for resonance frequency, which might not represent the source strength and effective area across frequencies. An acoustic FEA model could be used to analyze the outer shell acoustics and acoustic reflection from the shell can be counted as effects as well. Last but not least, since the models are multiplied, any small difference in the model could end up being large for the received signal downstream.

PUI transducers have a relative narrower bandwidth and lower resonance frequency. But based on the input impedance model in both air and 6 mbar  $CO_2$ , the mechanics of the transducer does not change much transiting from atmospheric air to 6 mbar  $CO_2$ . This has made the

comparison between the transmission testing in air and CO<sub>2</sub> a lot easier: going from air to 6 mbar CO<sub>2</sub>, the main change of the system is air density. Since the mechanics does not change much, it was predicted that the main factor of the transmission loss is contributed by the change in pressure.

Comparing to PUI, Kobitone transducer receives a larger amplitude in digital number if we use the same voltage and distance setup in the same pressure environment. Switching from air to 6 mbar CO<sub>2</sub>, Kobitone transducer has a larger shift in transducer dynamics. The damping ratio of Kobitone might not be ideal because of the fact that the fast updating rate is one of the requirement for an ultrasonic anemometer. Kobitone transducer does not have a circular piston mode shape: the center of the diaphragm is fixed. Therefore, more LDV experiments can be done to verify the parameters calculated.

Tufts cMUT transducers have a relatively smaller capacitance, higher resonance frequency and broader bandwidth. The broader bandwidth can maximize the gain of the electronics, therefore maximized the gain of the ultrasonic transmission. The cMUT used in this experiment have not provided strong signals in air and no transmission was observed in 6 mbar CO<sub>2</sub>. But it is possible that an alternate control electronics with higher gain will make the transmission in 6 mbar CO<sub>2</sub> possible.

CAP1 transducer have a larger size. It was also able to create a large signal in air. But due to the size of the transducer, a time domain testing was not achieved. The transducer can be characterized in CO<sub>2</sub> in the future by using a larger chamber. The strong acoustic signal it transmits and receives is extremely useful for anemometers on Mars. A future version of the CAP1 with a smaller size may be a good candidate for future testing.

## Chapter 7      Conclusions and Future Work

### 7.1 *Conclusions*

An acoustic model has been built and verified for all the ultrasonic transducers. Using digital signal processing codes in MATLAB, the model is able to predict time of flight for all the measurements in air and PUI in CO<sub>2</sub>, as well as the peak value for all the measurement of PUI of the chirp transmitted from the transducers selected with a relatively small percentage difference. This model can be used to test more ultrasonic transducers and enables transducer selection and signal processing optimization for the system.

Among the four ultrasonic transducers being tested with TivaUT module, PUI and Kobitone transducers were the transducers that provide high enough signal to noise ratio in 6 mbar CO<sub>2</sub>. Kobitone transducers have a relatively larger change in the transducer mechanics from atmosphere to CO<sub>2</sub> whereas PUI does not due to the geometry differences: Kobitone has a thinner vibrating diaphragm which is influenced more by the fluid density. Using the same voltage and gain setting, Kobitone was able to provide larger received signal in digital number. Some uncertainty persists regarding the TivaUT receive amplifier.

We have also proved that piezoelectric transducers are capable of making ultrasonic transmission in 6 mbar CO<sub>2</sub>, even though it has a much higher characteristic impedance than low pressure CO<sub>2</sub>. It was widely believed that due to impedance mismatching between piezoelectric transducers and Martian environment, it will be extremely difficult for acoustic transmission to be made. Our experiments have proved that impedance does not tell the whole story; transmission is possible for these transducers in low pressure CO<sub>2</sub>.

The most important acoustic loss is due to density change from air to 6 mbar of 6 mbar CO<sub>2</sub>, which results a loss of 44dB. In the small chamber we used for testing the transducers, the absorption effects are not a major effect; but this could become a major concern if a larger chamber or higher signal frequency is used.

## **7.2 Future Work**

There are a series of things that can be done in the future. First, current testing chamber built by Tufts University are only capable of testing the smaller transducers, whereas the CAP1 transducers cannot fit in the chamber. The current chamber is also limited in the maximum distance between the transmitter and the receiver. The optimal distance for such anemometers requires a distance of 1.8 m. Future testing will become easier once a bigger chamber can be used. A bigger volume allows a bigger distance between the transducers as well as smaller signal from reflection. A bigger volume also enables us to test more varieties of ultrasonic transducer. The bigger chamber should have an accurate indication of pressure by using a pressure gauge and it should also provide a temperature control which will provide a better simulation of the Martian atmosphere.

Aside from using a bigger chamber, we can also control the transducers using different or updated electronics. The TivaUT module enables us to measure the signal but other control devices (both commercialized and customized) might be able to provide us higher gain, which might be helpful for receiver amplification, which will be helpful to all transducers. At the same time, more ultrasonic transducers can be characterized for their ability to transmit and receive ultrasound in low-pressure system. For example, we can test smaller versions of CAP1 that are made by VN instruments. We can also use the ultrasonic transducers that has amplifier included in the package.

Furthermore, even though absorption coefficient on Mars was calculated mathematically, there was not much literature on the experimental data of absorption in 6 mbar CO<sub>2</sub>. Experiments



can be done to measure the effects of absorption in both air and 6 mbar CO<sub>2</sub> across frequencies at increments of distance.

A larger set of scanned LDV results with finer resolution can be done, which would also allow better modeling of the transducer transfer function, instead of relying on the simplification of a single effective area derived from a single LDV surface scan. A transfer function of both modes can be modeled for Kobitone transducer, which might give us a better alignment between the prediction and measurements.

Last but not least, the modeling of the acoustic system can also include FEA models for calculating the acoustic diffraction and reflection gains associated with the transducer housing.

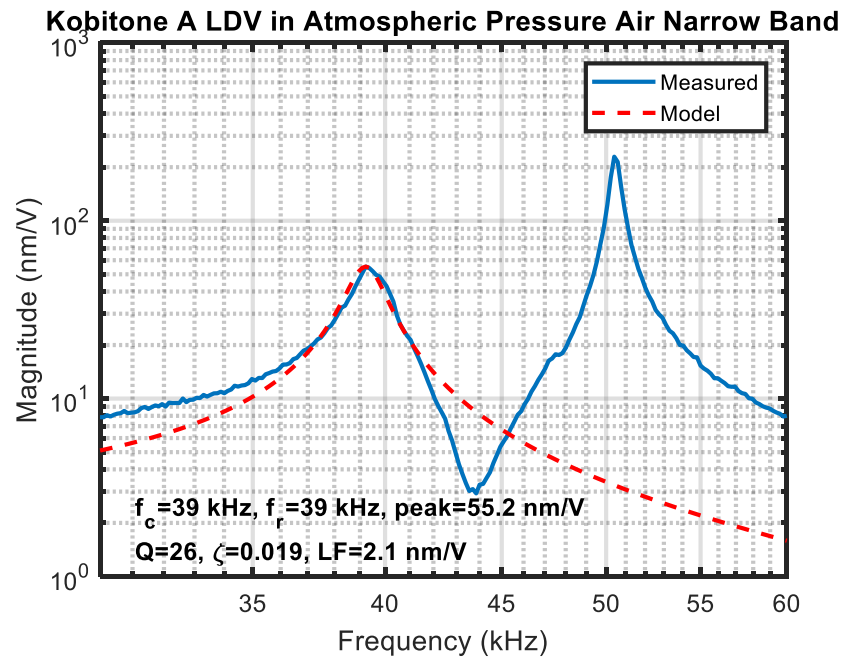
With all of the work mentioned above, more time domain measurements for the same sets of transducers can be done in the future to assess the accuracy and precision of our peak signal and time of flight prediction.



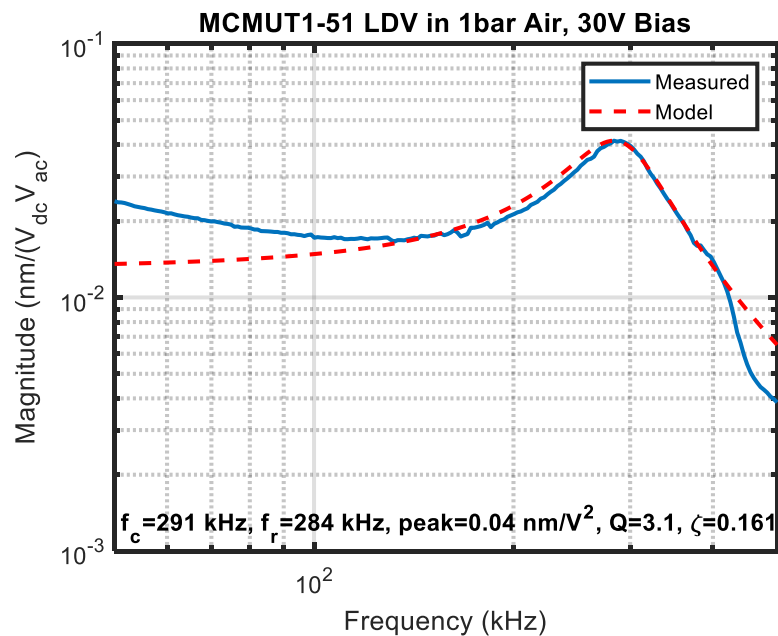
# Appendix A

## LDV scan and model plots

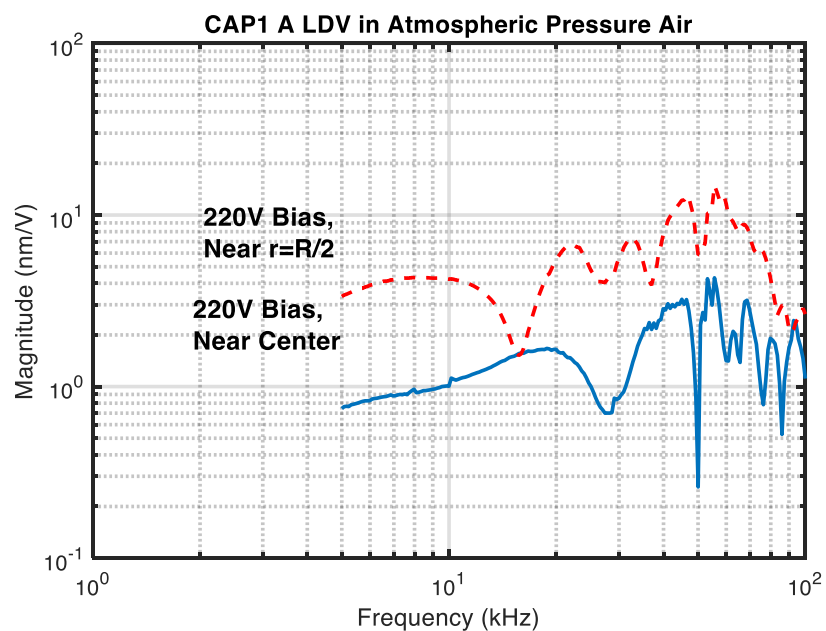
### A.1 LDV single point scan for Kobitone-A transducer



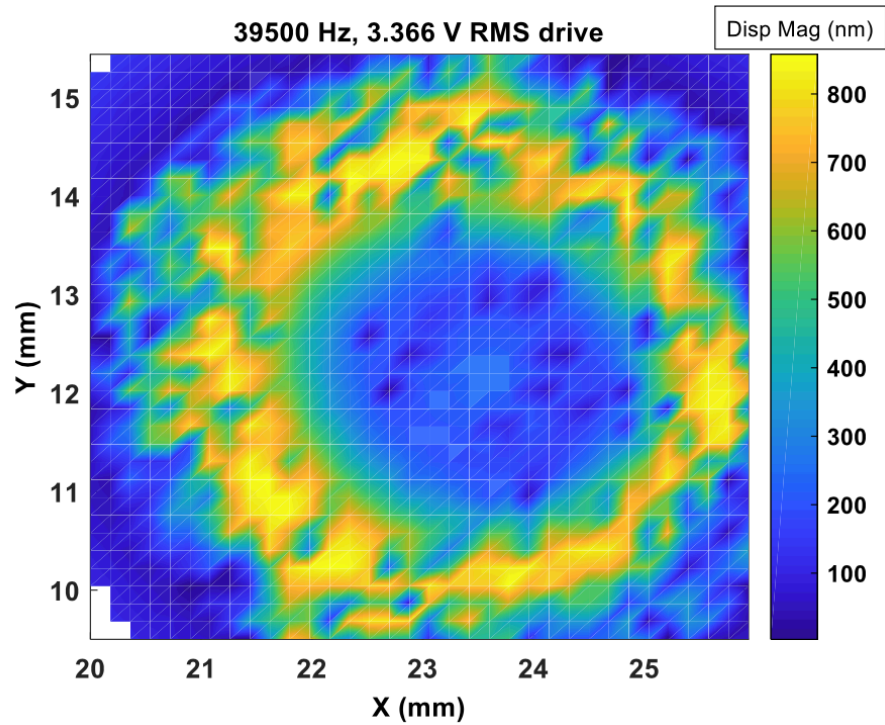
### A.2 LDV single point scan for cMUT1-51 transducer



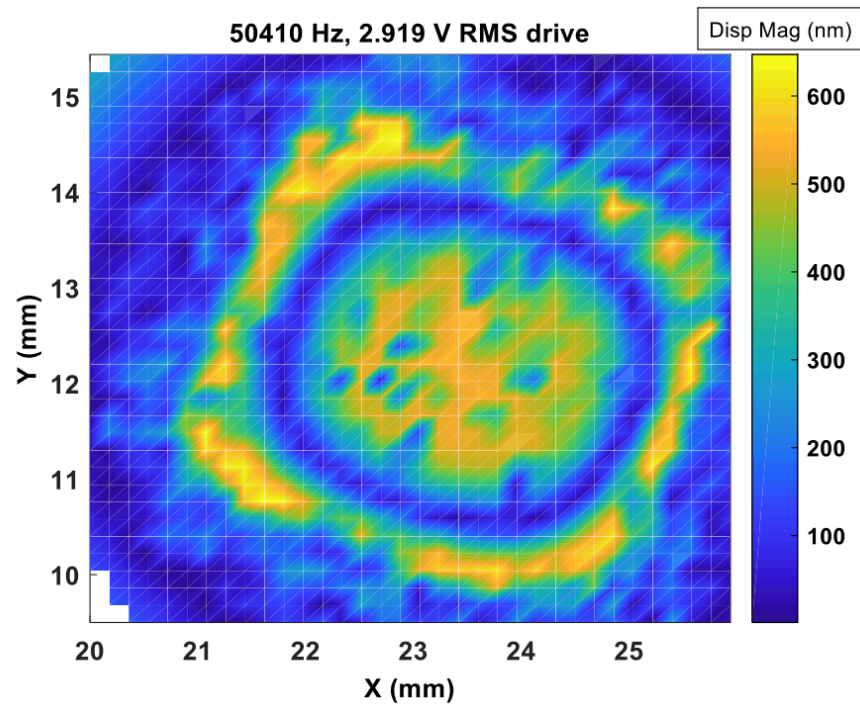
### A.3 LDV single point scan for CAP1 transducer



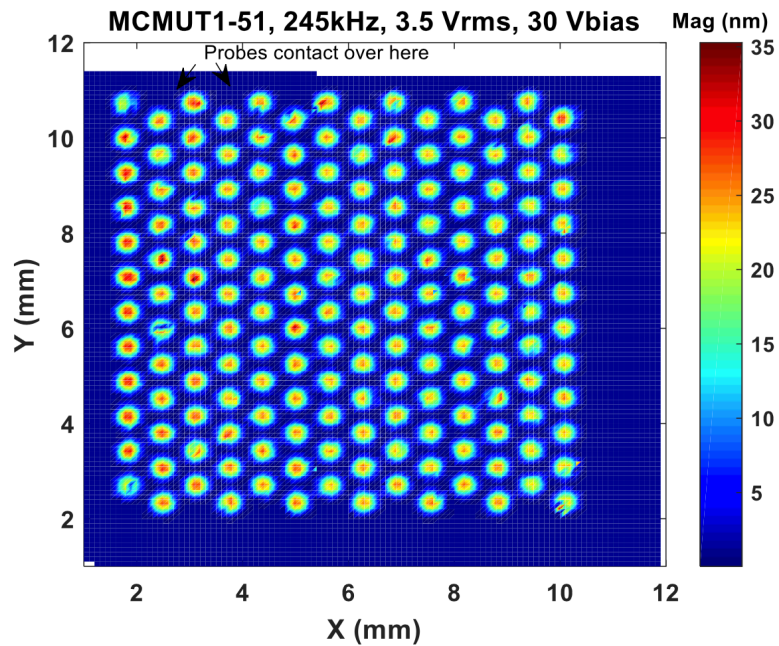
### A.4 LDV surface scan for Kobitone-A transducer at 39500 Hz



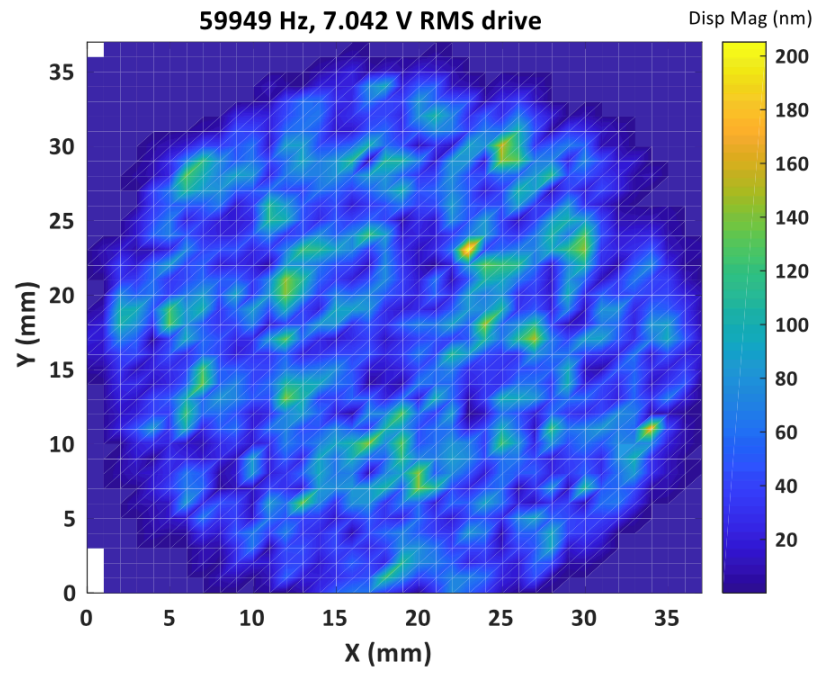
A.5 LDV surface scan for Kobitone-A transducer at 50410 Hz



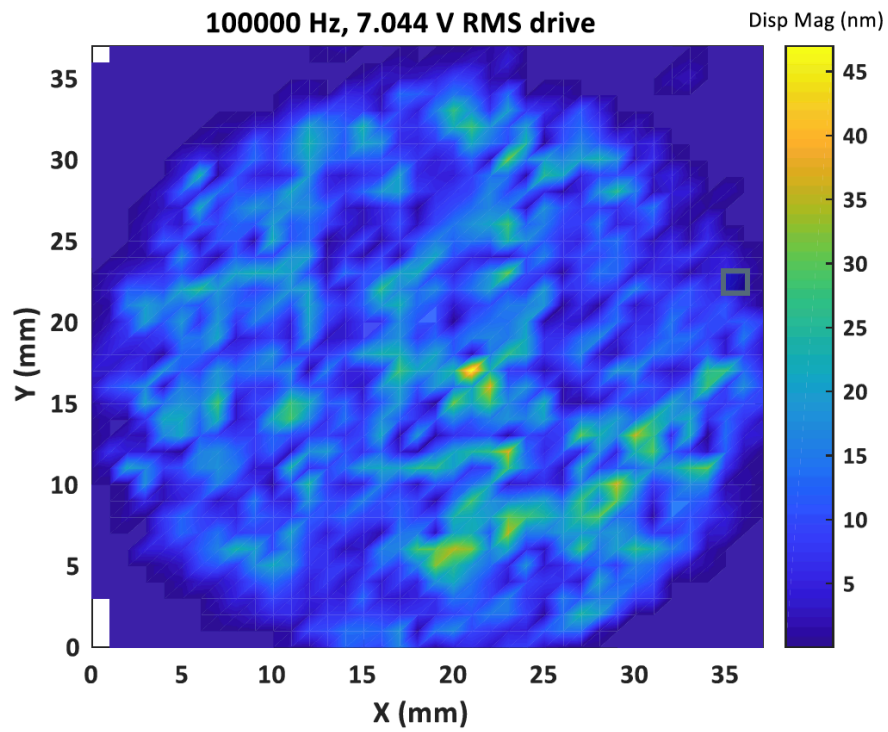
A.6 LDV surface scan for cMUT1-51 transducer



A.7 LDV surface scan for CAP1 transducer at 59949 Hz



A.8 LDV surface scan for CAP1 transducer at 100000 Hz

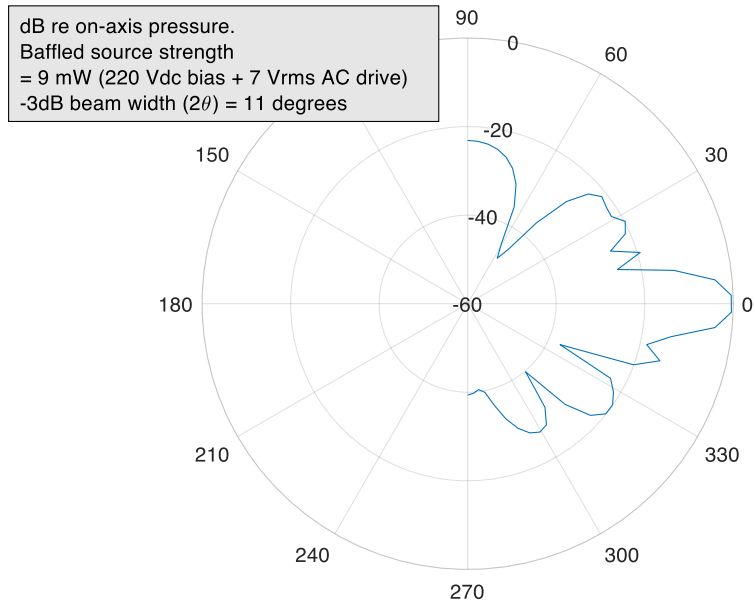


# Appendix B

## Beam Patten from LDV measurements

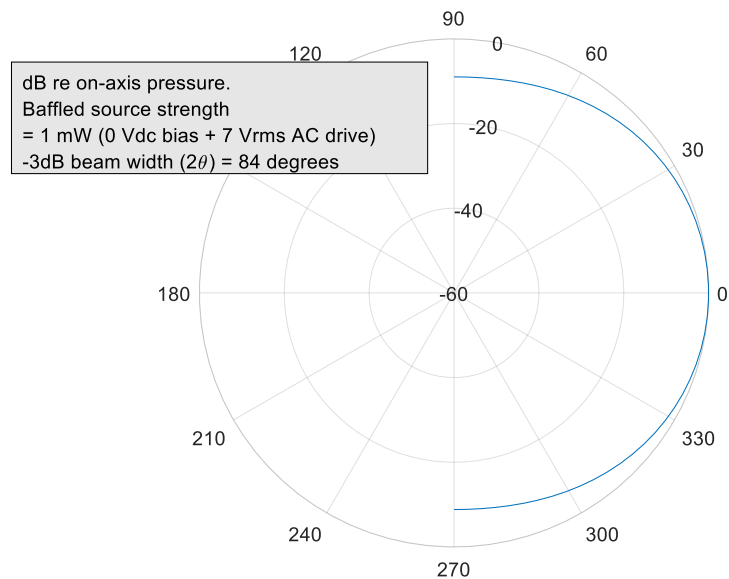
### B.1 Beam pattern for CAP1 transducer

**CAP1-A Farfield Beampattern from LDV at 60 kHz**

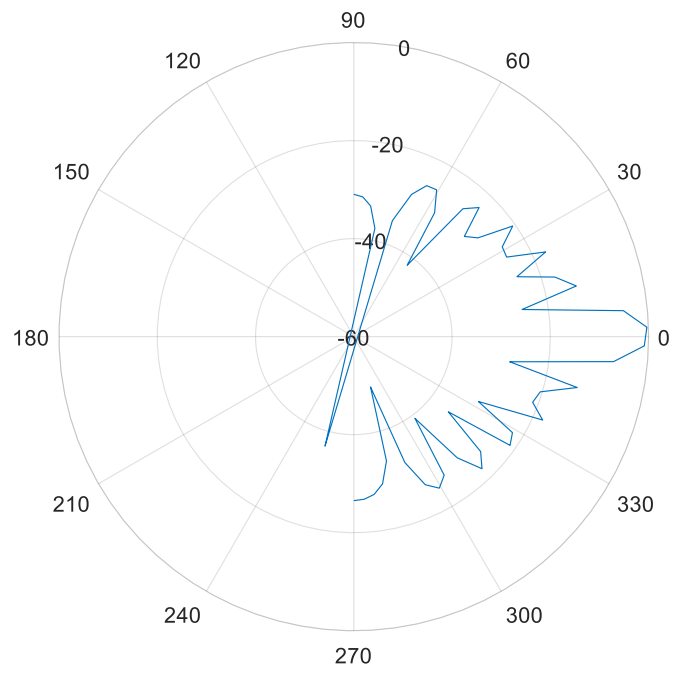


### B.2 Beam pattern for PUI transducer

**PUI Farfield Beampattern from LDV at 41 kHz**



### B.3 Beam pattern for cMUT1-51 transducer

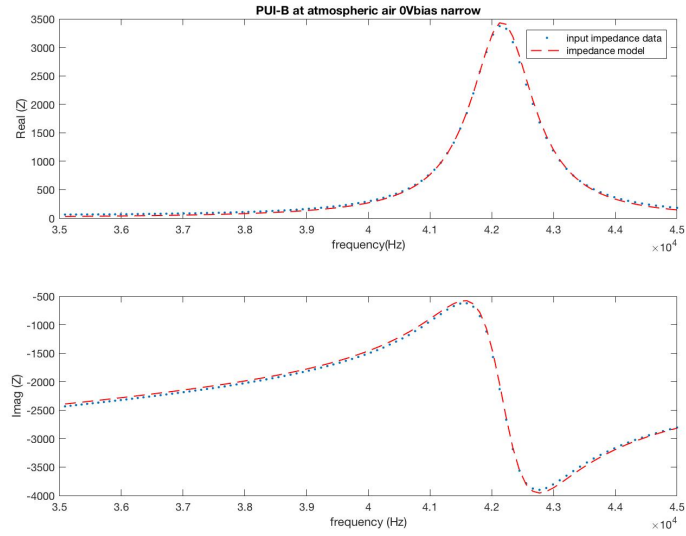




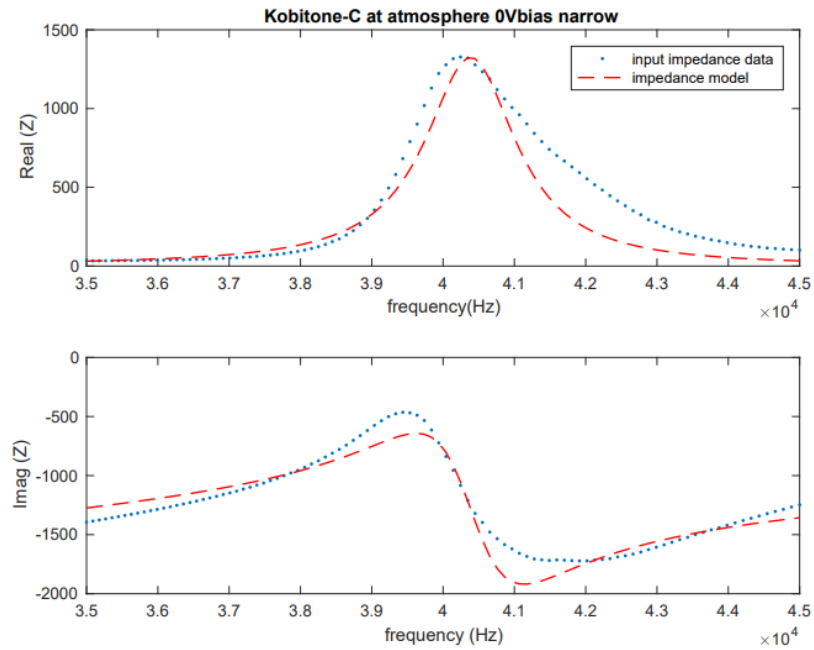
# Appendix C

## Input Impedance measurements and model

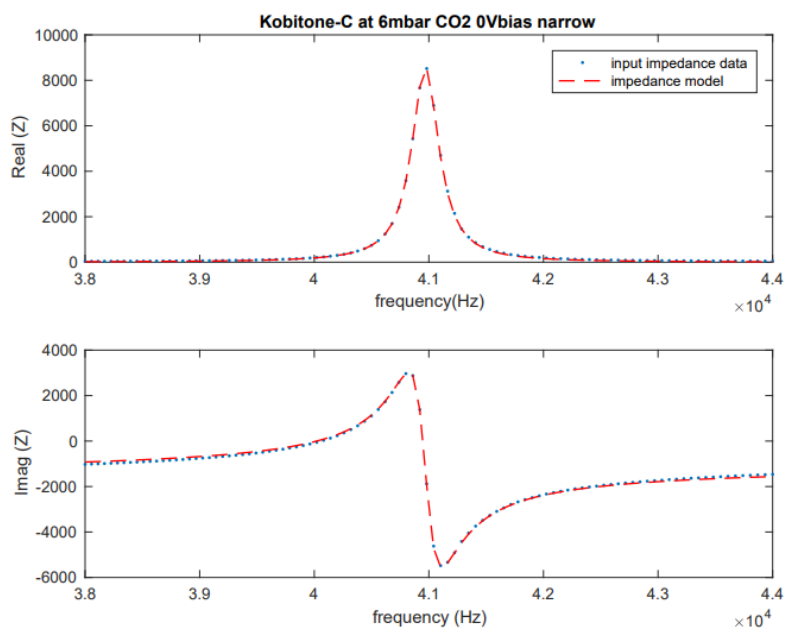
### C.1 Input impedance of PUI-B at atmosphere



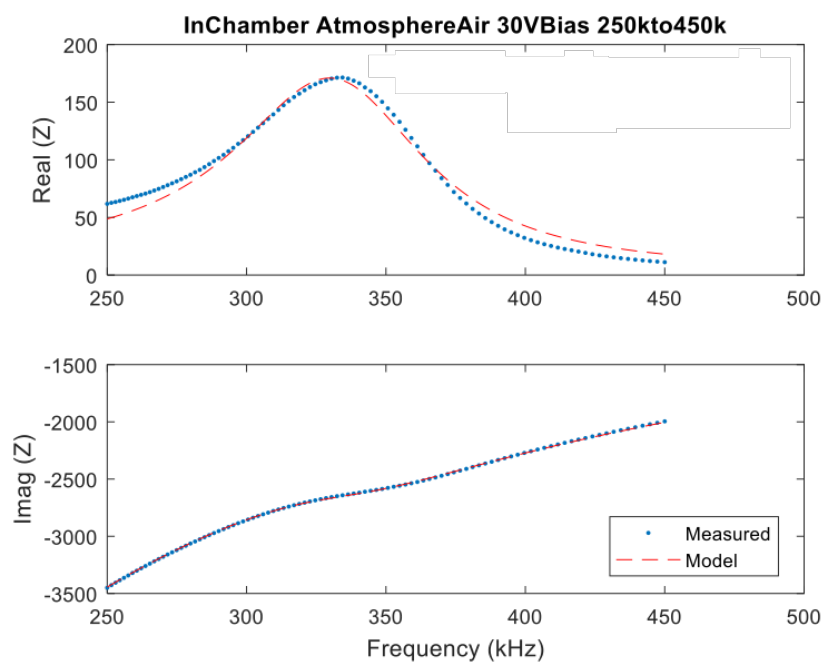
### C.2 Input impedance of Kobitone-C at atmosphere



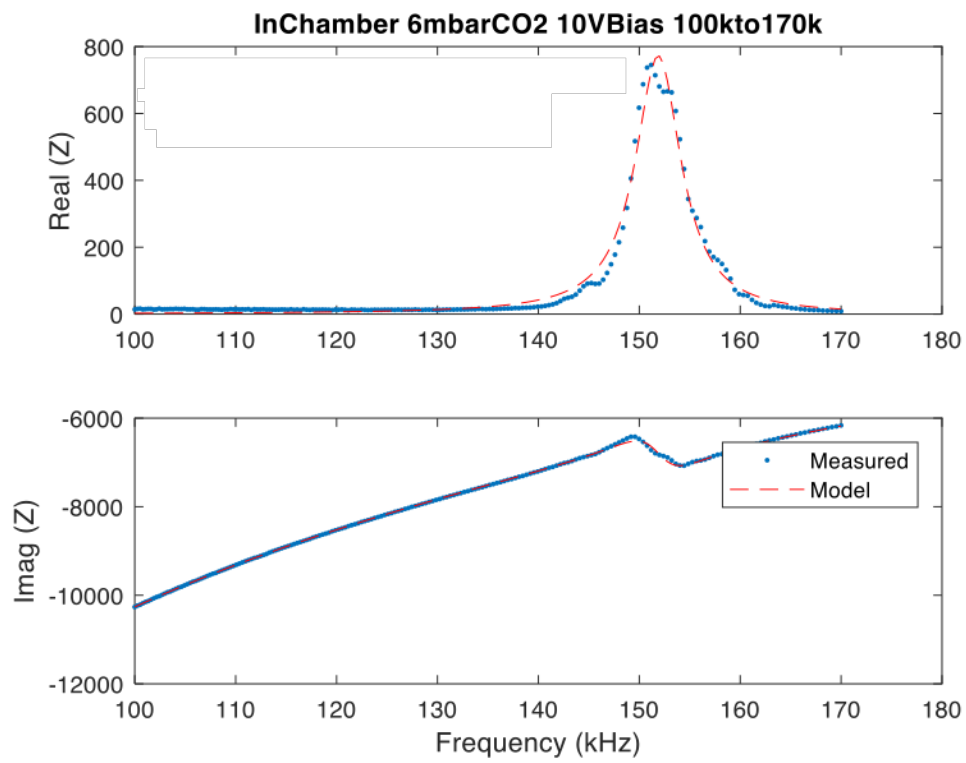
### C.3 Input impedance of Kobitone-C in 6mbar CO<sub>2</sub>



### C.4 Input impedance of cMUT1-51 at atmosphere



### C.5 Input impedance of cMUT1-40 in 6mbar CO<sub>2</sub>



# Appendix D

## MATLAB SCRIPT

### D.1 Plotting time of flight calculating time delay

```
%Put ADC1 ADC2 SigDataOut1 SigDataOut2 on a common time step
%t is the time used with SigDataOut1 and 2
%t1 is the time for ADC1
%t2 is the time for ADC2
%these are all in seconds

fname='*';
load([fname '.mat'])

dt=t(2)-t(1); %This should be the same for all 3 time vectors

use_which_run=3; %Which run do we want to use (If we did multiple)

%Assume Tconfig.StartOffsetT1=Tconfig.StartOffsetT2=0

SigOut1=[ones(1,floor(Tconfig.PreDelayT1/dt))*2^13 SigDataOut1];
SigOut1=[SigOut1 ones(1,length(ADC1)-length(SigOut1))*2^13];

SigOut2=[ones(1,floor(Tconfig.PreDelayT2/dt))*2^13 SigDataOut2];
SigOut2=[SigOut2 ones(1,length(ADC2)-length(SigOut2))*2^13];

%use time t1

%Make plot
figure
subplot(4,1,1)
plot(t1*1e3, (double(SigOut1)-2^13)/2^13)
set(gca, 'YLim', [-1.2 1.2])
ylabel('SigOut1')
subplot(4,1,2)
plot(t1*1e3, (ADC1(use_which_run,:)-2^11)/2^11)
set(gca, 'YLim', [-1.2 1.2])
hold on
%predicted time of flight for signals transmitted from CH1
tsup=2000e-6+(*./278.7);
plot(tsup*1e3*ones(size((ADC1(use_which_run,:)-2^11)/2^11)), ...
      (ADC1(use_which_run,:)-2^11)/2^11);
hold off
ylabel('ADC1')
subplot(4,1,3)
plot(t1*1e3, (double(SigOut2)-2^13)/2^13)
set(gca, 'YLim', [-1.2 1.2])
ylabel('SigOut2')
subplot(4,1,4)
plot(t1*1e3, (ADC2(use_which_run,:)-2^11)/2^11)
```

```

set(gca, 'YLim', [-1.2 1.2])
hold on
%predicted time of flight for signals transmitted from CH2
plot((tsup+3000e-6)*1e3*ones(size((ADC1(use_which_run,:)-2^11)/2^11)), ...
      (ADC1(use_which_run,:)-2^11)/2^11);
hold off
ylabel('ADC2')
xlabel('Time (msec)')

subplot(4,1,1)
title(fname, 'fontsize', 14)

```

## D.2 Cross correlation

```

[acor, lag] = xcorr(X, Y);
[~, I] = max(abs(acor));
lagDiff = lag(I);
timeDiff = lagDiff/Fs;
figure
plot(lag, acor)

```

## D.3 CPSD

```

% extract the scope data
V=dlmread('*.csv', ',', 2, 0);
t=transpose(V(:,1));
y=transpose(V(:,2));
tnew=t(t>=2000e-6 & t<=4000e-6)-2000e-6;
and 4000e-6 s
ynew=y(t>=2000e-6 & t<=4000e-6);
and 4000e-6 s
figure
plot(tnew, ynew);
xlabel('time (s)')
ylabel('Voltage (V)')
title('Voltage applied to transmitter')
N=length(tnew);
it is even
Fs=(N-1)/(max(tnew)-min(tnew));
oscilloscope
% configure the simulated data
T=2000e-6;
t=(0:(N-1))/Fs;
fc=520000;
BW=1000000;
k=BW/max(t);
f0=fc-BW/2;
Vout=sin(2*pi*(f0*t+(k/2)*t.^2));
x=0.5*(2^13)*Vout;
figure
% extracting data from scope data
% scope data time
% scope data voltage
% only takes in the t between 2000e-6
and 4000e-6 s
% only takes in the V between 2000e-6
and 4000e-6 s
% plot the scope data
% fcsame with number of terms, make sure
it is even
% this is the sampling rate of the
oscilloscope
% length of chirp
% center frequency (Hz)
% bandwidth (Hz)
% chirp rate (Hz/sec)
% start freq (Hz)
% linear chirp function
% 50% voltage sent

```

```

plot(tnew, x);
xlabel('time (s)')
ylabel('Digital Number')
title('Digital Number Sent')
% configure the window
width=2^8; % window size
overlap=width/2; % Window overlap (samples)
wn=ones(1,width); % uniform window
%CPSD calculation
m=1;
Pxx=[]; Pyy=[]; Pxy=[];
cnt=0; % number of averages
while (m<N-1-width)
    xn=x(m:m+width-1).*wn; % Just window the relevant part
    Xk=fft(xn);
    yn=ynew(m:m+width-1).*wn; % Just window the relevant part
    Yk=fft(yn);
    if cnt==0
        Pxx=2*Xk.*conj(Xk)/(Fs*width); % Compute the single sided auto-spectrum
        Pyy=2*Yk.*conj(Yk)/(Fs*width); % Compute the single sided auto-spectrum
        Pxy=2*Yk.*conj(Xk)/(Fs*width); % Compute the single sided cross-
spectrum
    else
        %Keep adding up the spectra:
        Pxx=Pxx+2*Xk.*conj(Xk)/(Fs*width); % Compute the single sided auto-spectrum
        Pyy=Pyy+2*Yk.*conj(Yk)/(Fs*width); % Compute the single sided auto-spectrum
        Pxy=Pxy+2*Yk.*conj(Xk)/(Fs*width); % Compute the single sided cross-
spectrum
    end
    m=m+(width-overlap);
    cnt=cnt+1; % number of averages
end
Pxx=Pxx/cnt; Pyy=Pyy/cnt; Pxy=Pxy/cnt;
F=0:Fs/width:Fs/2; % frequencies up to the Nyquist
frequency
% Phase and coherence:
Phase=atan2(imag(Pxy),real(Pxy)); % note, the atan2 function avoids the pi
ambiguity
Coh=Pxy.*conj(Pxy)./(Pxx.*Pyy);
figure
semilogx(F,Coh(1:length(F))) % plotting coherence
ylabel('Coherence')
xlabel('Frequency(Hz)')
title('Cross-Spectrum ')
H2=Pxy./Pxx; % calculating transfer function
S=20*log10(abs(H2(1:length(F))))); % express gain in dB
A=abs(H2(1:length(F))); % gain in ratio
figure
% subplot(2,1,1)
loglog(F(1:50),A(1:50))
xlabel('Frequency (Hz)')

```

```

ylabel('Gain (Vp/DNp)')
title('H1 20-1020 kHz')
% subplot(2,1,2)
figure
p=-unwrap(angle(H2(1:length(F))))*180/pi+360;
semilogx(F(1:50),p(1:50));
xlabel('Frequency (Hz)')
ylabel('Phase (deg)')
legend('From Cross Spectrum','System Bode Plot')

```

#### D.4 LDV modeling

```

S=load('*.csv');
title_text='*';
f=S(:,1);
dB=S(:,2);
deg=S(:,3);
RMS1=S(:,4);
RMS2=S(:,5);
SF=5e-3; %mm/s/V
Disp=10.^(dB/20)*SF.*RMS1*sqrt(2).*exp(1j*deg*pi/180)./(1j*f*2*pi);
Vac=RMS1*sqrt(2);

Mag=abs(Disp./Vac);

flimit_high=60e3; %Only search for peaks below this frequency (to avoid catching a
higher mode)
flimit_low=30e3; %Only search for peaks above this frequency (to avoid catching a
lower mode)

maxMag=max(Mag(f<flimit_high & f>flimit_low));
fr=f(Mag==maxMag);
flow=max(f(Mag<(maxMag/sqrt(2)) & f<fr));
fhigh=min(f(Mag<(maxMag/sqrt(2)) & f>fr));
Q=fr/(fhigh-flow);
zeta=1/(2*Q);
fc=fr/(1-zeta^2);

%Choose method of determining LF gain depending on narrow or wide band
%sweep:

%For narrow:
LF=maxMag/abs((fc^2)./(-fr.^2+2*zeta*1j*fc*fr+fc^2));

%For wide:
% LF=Mag(1);

% H=LF.*(fc^2)./(-f.^2+2*zeta*1j*fc*f+fc^2);
%For Kobitone
numerator=[126];
denominator=[1 2*2*pi*fc*zeta (2*pi*fc)^2];

```

```

H=tf(numerator,denominator);

figure
loglog(f/1000,Mag*1e9,'linewidth',2)
%axis([1e2 1e3 0.01 100])
grid
set(gca,'linewidth',2,'fontsize',12)
xlabel('Frequency (kHz)')
ylabel('Magnitude (nm/V)')
title(title_text)
xlims=get(gca,'xlim');
textlocx=((xlims(2)/xlims(1))^(1/20))*xlims(1);
ylims=get(gca,'ylim');
textlocy=((ylims(2)/ylims(1))^(1.2/10))*ylims(1);
% text(textlocx,textlocy,['f_c=' num2str(round(fc/100)/10) ' kHz, f_r='
num2str(round(fr/100)/10) ' kHz, peak=' num2str(round(maxMag*1e9*10)/10) '
nm/V'],'fontsize',12,'fontweight','bold');
textlocx=((xlims(2)/xlims(1))^(1/20))*xlims(1);
textlocy=((ylims(2)/ylims(1))^(0.5/10))*ylims(1);
% text(textlocx,textlocy,['Q=' num2str(round(Q*10)/10) ', \zeta='
num2str(round(zeta*1000)/1000) ', LF=' num2str(round(LF*10*1e9)/10) '
nm/V'],'fontsize',12,'fontweight','bold');
hold on
% loglog(f/1000,abs(H)*1e9,'r--','linewidth',2)
loglog(f/1000,(H)*1e9,'r--','linewidth',2)
saveas(gcf,[title_text '.fig'])
saveas(gcf,[title_text '.png'])

```

## D.5 Impedance modeling

```

V=dlmread('*.csv',' ',1,0); %extracting data from scope data
f=V(:,1);
Zreal=V(:,2);
Zimag=V(:,3);
Ztot=Zreal+i*Zimag;
figure(1)
subplot(2,1,1)
plot(f,Zreal,'.','LineWidth',2)
subplot(2,1,2)
plot(f,Zimag,'.','LineWidth',1)
figure(2)
plot(f,abs(Ztot))
fs=*; %resonance frequency from model
fp=*; %antiresonance frequency from model
ws=2*pi*fs;
wp=2*pi*fp;
Zws=*;
Zwp=*;
C0=sqrt((Zws^2*(wp^2-ws^2)+sqrt((2*wp^2*Zws*Zwp)^2+(Zws)^4*(wp^2-
ws^2)^2))/(2*(wp^2*Zwp*Zws)^2));
C1=C0*((wp/ws)^2-1);

```



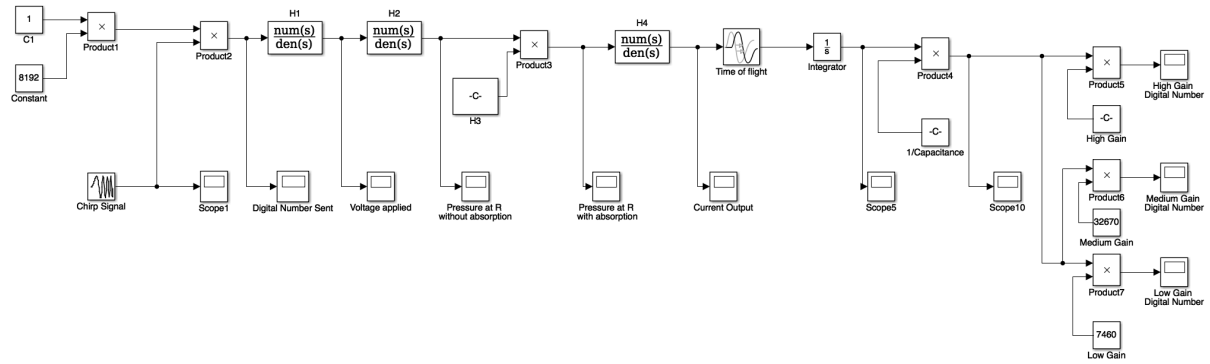
```

L1=1/(C1*ws^2);
R1=sqrt((Zws^2)/(1-(C0*ws*Zws)^2));
Z=(1./(w1*C0)).*(((ws^2-w1.^2+(j.*w1*R1/L1))./((-R1*w1/L1)+j.*(wp^2-w1.^2)));
figure(1)
subplot(2,1,1)
hold on
plot(f,real(Z),'r--','LineWidth',1)
title('PUI-B at atmospheric air 0Vbias narrow')
xlabel('frequency(Hz)')
ylabel('Real (Z)')
legend('input impedance data','impedance model')
hold off
subplot(2,1,2)
hold on
plot(f,imag(Z),'r--','LineWidth',1)
xlabel('frequency (Hz)')
ylabel('Imag (Z)')
% Calculate Q
flimit_high=60e3; %Only search for peaks below this frequency (to avoid catching a
higher mode)
flimit_low=30e3; %Only search for peaks above this frequency (to avoid catching a
lower mode)
A=real(Z);
maxMag=max(A(f<flimit_high & f>flimit_low));
fr=f(A==maxMag);
flow=max(f(A<(maxMag/sqrt(2)) & f<fr));
fhigh=min(f(A<(maxMag/sqrt(2)) & f>fr));
Q=fr/(fhigh-flow);
zeta=1/(2*Q);
fc=fr/(1-zeta^2);

```

# Appendix E

## Simulink Block Diagram



## Bibliography

1. McBean, G.A., *Instrument requirements for eddy correlation measurements*. Journal of Applied Meteorology, 1972. **11**(7): p. 1078-1084.
2. Banfield, D. and R. Dissly. *A Martian sonic anemometer*. in *Aerospace Conference, 2005 IEEE*. 2005. IEEE.
3. Gómez - Elvira, J., et al., *Curiosity's rover environmental monitoring station: Overview of the first 100 sols*. Journal of Geophysical Research: Planets, 2014. **119**(7): p. 1680-1688.
4. Carovac, A., F. Smajlovic, and D. Junuzovic, *Application of ultrasound in medicine*. Acta Informatica Medica, 2011. **19**(3): p. 168.
5. Quazi, A., *An overview on the time delay estimate in active and passive systems for target localization*. IEEE Transactions on Acoustics, Speech, and Signal Processing, 1981. **29**(3): p. 527-533.
6. *The ROV Little Hercules' scanning sonar imaged this 19th century wooden-hulled shipwreck in March 2012*. 2012; Available from: <http://oceanexplorer.noaa.gov/technology/tools/sonar/sonar.html>.
7. Kinsler, L.E., et al., *Fundamentals of acoustics*. Fundamentals of Acoustics, 4th Edition, by Lawrence E. Kinsler, Austin R. Frey, Alan B. Coppens, James V. Sanders, pp. 560. ISBN 0-471-84789-5. Wiley-VCH, December 1999., 1999: p. 560.
8. Williams, J.P., *Acoustic environment of the Martian surface*. Journal of Geophysical Research: Planets, 2001. **106**(E3): p. 5033-5041.
9. Pollet, B., *Power ultrasound in electrochemistry: from versatile laboratory tool to engineering solution*. 2012: John Wiley & Sons.
10. Brown, L.F., *Electromechanical modeling, performance testing, and design of piezoelectric polymer film ultrasound transducers*. 1988.
11. Akasheh, F., et al., *Development of piezoelectric micromachined ultrasonic transducers*. Sensors and Actuators A: Physical, 2004. **111**(2-3): p. 275-287.
12. Ladabaum, I., et al., *Surface micromachined capacitive ultrasonic transducers*. IEEE transactions on ultrasonics, ferroelectrics, and frequency control, 1998. **45**(3): p. 678-690.
13. Jin, X., I. Ladabaum, and B.T. Khuri-Yakub, *The microfabrication of capacitive ultrasonic transducers*. Journal of Microelectromechanical Systems, 1998. **7**(3): p. 295-302.
14. Shin, M., et al., *Micromachined ultrasonic Doppler velocity sensor using nickel on glass transducers*. Sensors and Actuators A: Physical, 2014. **208**: p. 37-49.
15. Shin, M., et al., *Acoustic Doppler velocity measurement system using capacitive micromachined ultrasound transducer array technology*. The Journal of the Acoustical Society of America, 2013. **134**(2): p. 1011-1020.
16. Škvor, Z., *On the acoustical resistance due to viscous losses in the air gap of electrostatic transducers*. Acta acustica united with acustica, 1967. **19**(5): p. 295-299.
17. Corrsin, S., *Extended Applications of the Hot - Wire Anemometer*. Review of Scientific Instruments, 1947. **18**(7): p. 469-471.
18. Sheppard, P., *An improved design of cup anemometer*. Journal of Scientific Instruments, 1940. **17**(9): p. 218.

19. Andrews, G., D. Bradley, and G. Hundy, *Hot wire anemometer calibration for measurements of small gas velocities*. International Journal of Heat and Mass Transfer, 1972. **15**(10): p. 1765-1786.
20. Johnson, D.A., *Laser Doppler anemometry*. 1988.
21. Ahmed, N., et al., *Miniature laser anemometer for 3D measurements*. Measurement Science and Technology, 1990. **1**(3): p. 272.
22. Burns, S., et al., *Using sonic anemometer temperature to measure sensible heat flux in strong winds*. Atmospheric Measurement Techniques, 2012. **5**(9): p. 2095-2111.
23. McKay, C.P. and M.M. Marinova, *The physics, biology, and environmental ethics of making Mars habitable*. Astrobiology, 2001. **1**(1): p. 89-109.
24. Mahaffy, P.R., et al., *Abundance and isotopic composition of gases in the Martian atmosphere from the Curiosity rover*. Science, 2013. **341**(6143): p. 263-266.
25. Sheehan, W., *The planet Mars: A history of observation & discovery*. 1996: University of Arizona Press.
26. Balme, M. and R. Greeley, *Dust devils on Earth and Mars*. Reviews of Geophysics, 2006. **44**(3).
27. *Mars' Whirling Dust Devil*. 2012; Available from: [https://www.nasa.gov/mission\\_pages/MRO/multimedia/pia15545.html](https://www.nasa.gov/mission_pages/MRO/multimedia/pia15545.html).
28. Soffen, G.A., *Mars and the remarkable Viking results*. Journal of Spacecraft and Rockets, 1978. **15**(4): p. 193-200.
29. *Viking Lander Model*. 2007; Available from: <https://www.jpl.nasa.gov/spaceimages/details.php?id=PIA09703>.
30. Hess, S., et al., *Meteorological results from the surface of Mars: Viking 1 and 2*. Journal of Geophysical Research, 1977. **82**(28): p. 4559-4574.
31. Chamberlain, T., et al., *Atmospheric measurements on mars: The viking meteorology experiment*. Bulletin of the American Meteorological Society, 1976. **57**(9): p. 1094-1104.
32. Schofield, J., et al., *The Mars Pathfinder atmospheric structure investigation/meteorology (ASI/MET) experiment*. Science, 1997. **278**(5344): p. 1752-1758.
33. Sullivan, R., et al., *Results of the Imager for Mars Pathfinder windsock experiment*. Journal of Geophysical Research: Planets, 2000. **105**(E10): p. 24547-24562.
34. Seiff, A., et al., *The atmosphere structure and meteorology instrument on the Mars Pathfinder lander*. Journal of Geophysical Research: Planets, 1997. **102**(E2): p. 4045-4056.
35. Gunnlaugsson, H.P., et al., *Telltale wind indicator for the Mars Phoenix lander*. Journal of Geophysical Research: Planets, 2008. **113**(E3).
36. Petrosyan, A., et al., *The Martian atmospheric boundary layer*. Reviews of Geophysics, 2011. **49**(3).
37. Van Boxel, J., G. Sterk, and S. Arens, *Sonic anemometers in aeolian sediment transport research*. Geomorphology, 2004. **59**(1-4): p. 131-147.
38. Dominguez, M., et al., *A hot film anemometer for the Martian atmosphere*. Planetary and Space Science, 2008. **56**(8): p. 1169-1179.
39. Walker, I.J., *Physical and logistical considerations of using ultrasonic anemometers in aeolian sediment transport research*. Geomorphology, 2005. **68**(1-2): p. 57-76.

40. Castellini, P., M. Martarelli, and E. Tomasini, *Laser Doppler Vibrometry: Development of advanced solutions answering to technology's needs*. Mechanical Systems and Signal Processing, 2006. **20**(6): p. 1265-1285.
41. Wong, G.S., *Speed of sound in standard air*. The Journal of the Acoustical Society of America, 1986. **79**(5): p. 1359-1366.
42. Cramer, O., *The variation of the specific heat ratio and the speed of sound in air with temperature, pressure, humidity, and CO2 concentration*. The Journal of the Acoustical Society of America, 1993. **93**(5): p. 2510-2516.
43. Lenoir, B., D. Banfield, and D.A. Caughey, *Accommodation study for an anemometer on a Martian lander*. Journal of Atmospheric and Oceanic Technology, 2011. **28**(2): p. 210-218.
44. Harris, F.J., *On the use of windows for harmonic analysis with the discrete Fourier transform*. Proceedings of the IEEE, 1978. **66**(1): p. 51-83.
45. Fabijanski, P. and R. Lagoda, *Modeling and Identification of Parameters the Piezoelectric Transducers in Ultrasonic Systems*, in *Advances in Ceramics-Electric and Magnetic Ceramics, Bioceramics, Ceramics and Environment*. 2011, InTech.
46. Touloukian, Y.S., S. Saxena, and P. Hestermans, *Viscosity*. Vol. 11. 1975: IFI/Plenum.